

# Studies and Applications of Hyperpolarized $^{129}\text{Xe}$

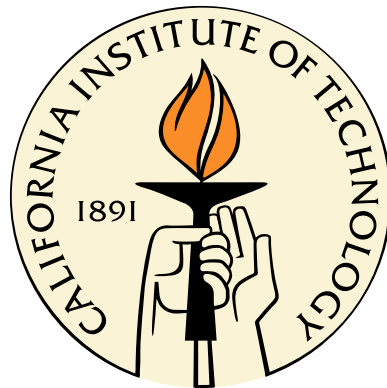
Thesis by

Wenjin Shao

In Partial Fulfillment of the Requirements

for the Degree of

Doctor of Philosophy



California Institution of Technology

Pasadena, California

2004

(Defended May 17th, 2004)



To my wife, Fuping, for her longtime support.

# Acknowledgements

My deepest thanks to my advisor, Dr. Emlyn W. Hughes, for his guidance in my research work; to Guodong Wang, Tina Pavlin, Peter Mastromarino, G. Mark Jones, and Steffen Jensen, the current and previous students in my group, and to Scott C. Greig, Steve M. Conolly, and Blaine A. Chronik, my collaborators in Stanford University, for their valuable help and discussions; to Georgia Frueh, our wonderful group secretary for everything; to Raymond Fuzesy and Faye Witharm, for helping with the lab work and sharing their knowledge and experience; and to the entire Caltech society, for the wonderful experience I had here during the past five years. I'd also like to thank Henry D. Thoreau and Omar Khayyám, for the delight I derived from their works *Walden* and *Rubáiyát*.

# Abstract

In this thesis, research work concerning studies and applications of hyperpolarized  $^{129}\text{Xe}$  is presented. The research includes two projects. The first project is the measurement and interpretation of the spin-exchange rates between  $^{129}\text{Xe}$  and three alkali metals Rb, Cs, and K, for the cell density range of 0.2-0.7 amagats, with the alkali number densities directly measured by the Faraday rotation method. The determination of the constants governing the spin-exchange process provides a better understanding of the spin-exchange optical pumping method that is used to polarize  $^{129}\text{Xe}$ , and it helps the optimization of mass production of hyperpolarized  $^{129}\text{Xe}$ . The second project of the research work involves the construction of a low readout field imaging system, which is capable of producing magnetic resonance images using both water and hyperpolarized  $^{129}\text{Xe}$  as imaging agents, under a low readout magnetic field, and is the first of its kind at room temperature.

# Contents

<b>Acknowledgements</b>	<b>iv</b>
<b>Abstract</b>	<b>v</b>
<b>1 Introduction</b>	<b>1</b>
<b>2 Theory</b>	<b>5</b>
2.1 Spin-Exchange Optical Pumping . . . . .	5
2.1.1 Optical Pumping . . . . .	6
2.1.2 Spin-Exchange . . . . .	9
2.2 The Spin-Exchange Rate . . . . .	15
2.3 Nuclear Magnetic Resonance (NMR) and Magnetic Resonance Imaging (MRI) . . . . .	20
2.3.1 NMR Principles . . . . .	20
2.3.2 Basics of MRI . . . . .	27
<b>3 Experiments I: Measurements of Spin-Exchange Rate Constants</b>	<b>32</b>
3.1 Experimental Setup . . . . .	33
3.2 Measurements of Spin-Exchange Rates between $^{129}\text{Xe}$ and Alkalis . .	39
3.3 Direct Measurements of the Alkali Number Density Using the Faraday Rotation Method . . . . .	48
3.4 Determination of the Spin-Exchange Rate Constants . . . . .	58
<b>4 Experiments II: Imaging Study</b>	<b>63</b>
4.1 Sample Cell Construction . . . . .	64

4.2	$^{129}\text{Xe}$ Polarimetry . . . . .	72
4.3	The Imaging System . . . . .	81
4.3.1	The Stanford PMRI System for Water Imaging . . . . .	81
4.3.2	Experimental Design for Performing Hyperpolarized $^{129}\text{Xe}$ MRI in the PMRI System . . . . .	85
4.4	Imaging Results . . . . .	89
<b>5</b>	<b>Future Outlook</b>	<b>94</b>
	<b>Bibliography</b>	<b>96</b>

# Chapter 1

## Introduction

The practice of polarizing noble gases started with  $^3\text{He}$  [1, 2], and its usages were first found in the field of nuclear physics. With two paired protons and an unpaired neutron in its nucleus, polarized  $^3\text{He}$  provides a stable source of polarized neutrons, and has been widely applied in nuclear physics studies [3, 4, 5]. When properly polarized,  $^3\text{He}$  also has applications in various fields including medical magnetic resonance imaging (MRI) [6]. During the attempts to achieve high polarization of  $^3\text{He}$  at high densities, the technique of spin-exchange optical pumping (SEOP) [2, 7, 8] has been developed. SEOP utilizes the spin of alkali metal valence electrons to transfer angular momentum from laser light to the nuclei of  $^3\text{He}$ , and routinely achieves  $^3\text{He}$  polarizations of  $\gtrsim 50\%$  [3, 9].

When the SEOP technique was brought to maturity for  $^3\text{He}$ , it was soon afterwards applied to polarize other noble gases [10, 11]. Of them,  $^{129}\text{Xe}$  was used for numerous applications including medical diagnosis [12, 13], surface studies [14, 15], and searches for permanent electric dipole moments [16].  $^{129}\text{Xe}$  has certain merits as an agent for MRI, compared to  $^3\text{He}$ :  $^{129}\text{Xe}$  can be polarized very fast ( $\sim 1$  minute vs.  $\gtrsim 10$  hours for  $^3\text{He}$ ),  $^{129}\text{Xe}$  is relatively cheap ( $\sim 10$  dollars per liter vs.  $\sim 100$  dollars per liter for  $^3\text{He}$ ), its larger chemical shift results in a higher sensitivity to its environment, and  $^{129}\text{Xe}$  is soluble in blood, while  $^3\text{He}$  is not. The polarization of  $^{129}\text{Xe}$  that can be routinely achieved is 10%-20% [16, 17, 18]. While this number is about  $10^5$  times larger than its thermal polarization at room temperature at a magnetic field of 1 Tesla, it is still smaller than the achievable polarization for  $^3\text{He}$  by a factor of  $\sim 3$ . This low

polarization greatly limits the applications of polarized  $^{129}\text{Xe}$ . Therefore, studies to improve the  $^{129}\text{Xe}$  polarization are still an important endeavour. My research is focused on the study of the SEOP process for  $^{129}\text{Xe}$ . The ultimate goal is to try to improve the  $^{129}\text{Xe}$  polarization. The application to MRI is the most important motivation.

During a typical SEOP process to polarize  $^{129}\text{Xe}$ ,  $^{129}\text{Xe}$  is mixed with the vapor of some alkali metal in a transparent cell. Currently, Rb is most frequently used for polarizing  $^{129}\text{Xe}$ , while K and Cs are possible alternatives. Circularly polarized laser light shines on the cell and polarizes the spin of the alkali metal's valence electron. The polarized electrons subsequently interact with the nuclear spin of  $^{129}\text{Xe}$ , and transfer angular momentum to  $^{129}\text{Xe}$ . The spin-exchange between alkalis and  $^{129}\text{Xe}$  can occur in two ways: either exchange during binary collisions of the two species of particles, or exchange by forming alkali- $^{129}\text{Xe}$  van der Waals molecules (vdW molecules) [8, 19]. Of them, the latter case requires the presence of third-body particles. In Ch. 2 we will make detailed discussions about the theoretical background pertaining to the SEOP process.

To improve the polarization of  $^{129}\text{Xe}$  achieved by the SEOP method, it is naturally useful to learn more about both of the two mechanisms contributing to the spin-exchange rate between the alkali metals K, Rb, and Cs and  $^{129}\text{Xe}$ . This knowledge gives us information on how varying a couple of parameters, including the alkali metal species, the number densities of the gases in the cell, and the cell temperature, optimizes the polarization. In a 1985 paper by Zeng *et al.*, the group measured and studied the spin-exchange rate constants between K, Rb, and Cs and  $^{129}\text{Xe}$  at low cell densities, and in  $\text{N}_2$ -dominating environments [11]. Current efforts in the production of hyperpolarized  $^{129}\text{Xe}$ , however, use higher cell densities ( $\sim 1$  amagat <sup>1</sup>) and Xe-dominated environments. Accurate measurements of the spin-exchange rate constants for the different conditions are, therefore, important. The relevant constants for  $^{129}\text{Xe}$ -Rb spin-exchange have more recently been measured by Cates *et al.* at  $\sim 1$  amagat densities [20], but tests for K and Cs under similar conditions have not

---

<sup>1</sup>One amagat =  $2.69 \times 10^{25} \text{m}^{-3}$ , which is the number density of a gas at 1 atm pressure and  $0^\circ\text{C}$ .

	K	Rb	Cs
$\ll 1$ atm, N <sub>2</sub> dominating	[11]	[11]	[11]
$\sim 1$ atm, Xe dominating	√	√, [20]	√

Table 1.1: Summary of published spin-exchange rate constants measurements and those presented in this thesis for various combinations of alkali-<sup>129</sup>Xe pairs and general experimental conditions. The published measurements are marked by reference numbers, and our new measurements are marked by “√.”

been done. In Ch. 3, results will be presented of measurements of the spin-exchange rates between K, Rb and Cs and <sup>129</sup>Xe, for cell densities in the range of 0.2 to 0.7 amagats. Explanations and analyses of the measured data, and determination of the rate constants, will also be included in Ch. 3.

For clarity, Table 1.1 lists the combinations of alkali-<sup>129</sup>Xe pairs and experimental conditions. The combinations in which spin-exchange rate constants have been measured in existing literature, and those in which the constants will be presented in this thesis, are marked in Table 1.1.

One more issue that arose in recent years is the applicability of the empirical saturated vapor density formulae for the alkali metals. In the experiments by both Zeng *et al.* [11] and Cates *et al.* [20], these formulae were applied to calculate the alkali number densities in the cell from the measured cell temperatures. However, in several recent papers [21, 22], it has been reported that the values from the empirical formulae can vastly differ from the directly measured alkali densities. Some researchers (e.g., [21]) also reported cell-to-cell differences in the relation between temperature and alkali density. In our experiments, we studied the alkali densities in independent cells using Faraday rotation method [23], and found that the measured values are indeed different with values from the formulae, with the difference up to a factor of 3 in the K case. However, we didn’t observe the cell-to-cell difference. We modified the existing formulae by adding scaling factors to fit our experimental results. Since our results of the spin-exchange rate constants were derived using our own empirical formulae, they are free from the possible errors related with using formulae in the literature.

A second study presented in this thesis pertains to the application of  $^{129}\text{Xe}$  polarized by SEOP (“hyperpolarized”  $^{129}\text{Xe}$ , to be distinguished with  $^{129}\text{Xe}$  with thermal polarizations) in magnetic resonance imaging (MRI). Compared with the thermal polarizations of imaging agents exploited in conventional MRI [24], the polarizations of hyperpolarized  $^{129}\text{Xe}$  are usually larger by a factor of about  $10^5$ . Moreover, unlike the thermal polarization, which is proportional to the strength of the holding magnetic field, the polarization achieved by SEOP does not vary with the magnetic field. Therefore, with hyperpolarized  $^{129}\text{Xe}$ , it wouldn’t be necessary to go to high magnetic fields using expensive magnets in order to obtain good signal-to-noise ratios (SNR’s), and the cost of an imaging system can be substantially reduced.

There is another MRI technique, which works with room temperature thermal polarizations, but can also use a low magnetic field to collect signals, and reduce the system cost. It is called prepolarized MRI (PMRI) [25, 26], and was carefully explored by the Macovski group at Stanford University. In this technique, a strong ( $\sim 1$  T) but not very uniform ( $\sim 20\%$ ) magnetic field is first turned on for a short time ( $\sim 40$  ms) to induce a relatively high thermal magnetization, and subsequently a weak ( $\sim 30$  mT) but uniform ( $\sim 10$  ppm) field is used to collect signals. During a collaboration between our group (Hughes group at Caltech) and Macovski group at Stanford, the hyperpolarized  $^{129}\text{Xe}$  MRI and PMRI techniques were successfully demonstrated on a single imaging system [17]. This the first successful attempt to perform both hyperpolarized  $^{129}\text{Xe}$  MRI and water MRI at low magnetic field strength and room temperature. Our part (the Caltech part) in the collaboration included trying techniques to optimize the  $^{129}\text{Xe}$  polarization, construction of a vacuum system to produce cells for polarizing  $^{129}\text{Xe}$ , testing the cells, setting up a laser and magnet system to polarize  $^{129}\text{Xe}$  cells by the SEOP method, and polarizing the cells for performing MRI. More details about this project will be discussed in Ch. 4, and the MR images of tested cells will be shown.

Conclusion and future prospects are presented in Ch. 5.

# Chapter 2

## Theory

In this chapter, we will lay out the theoretical foundations for the research to be presented in this thesis. Sec. 2.1 discusses the theory of spin-exchange optical pumping (SEOP), which includes two processes, optical pumping and spin-exchange. The section will specifically focus on the SEOP for  $^{129}\text{Xe}$ . Sec. 2.2 includes further detailed discussions about the spin-exchange rate, namely how the rate depends on various factors. Finally, Sec. 2.3 will be a brief introduction to the theories of nuclear magnetic resonance and magnetic resonance imaging.

### 2.1 Spin-Exchange Optical Pumping

Spin-exchange optical pumping (SEOP) [2, 7, 8] is the technique commonly applied for producing polarized noble gases at high densities. SEOP involves two processes, firstly, the optical pumping of the spin of the alkali metal atom's valence electrons, in which angular momentum is transferred from photons in a circularly polarized laser beam to the alkali metal electrons, and secondly, the spin-exchange between the alkali metal atoms and the noble gas nuclei, in which the angular momentum is subsequently transferred to the nuclear spin of the noble gas. We'll discuss in this section the theories of these two processes. While the SEOP theory applies to polarizing  $^3\text{He}$  and  $^{129}\text{Xe}$  with only minor differences between the two, this thesis is primarily about the  $^{129}\text{Xe}$  case, and we will hereafter refer to our subject as "SEOP of  $^{129}\text{Xe}$ ."

In the following two subsections we will study the processes of optical pumping and spin-exchange respectively.

### 2.1.1 Optical Pumping

Generally speaking, optical pumping is defined as manipulating the internal degrees of freedom of a sample of atoms using light [27]. It is an efficient means to transfer angular momentum from photons to the atoms. Before beginning to discuss the optical pumping for our case, we need to define a few variables: let  $\vec{I}$  be the alkali nuclear spin,  $\vec{S}$  be the alkali electron spin,  $\vec{F} \equiv \vec{I} + \vec{S}$  be the total angular momentum, and  $z$ -direction be the direction of the holding external magnetic field  $B_0 \hat{z}$ . For most SEOP experimental conditions, the holding field is weak enough to ensure that  $F^2$  and  $F_z$  are good quantum numbers. We will assume a weak holding field in all following discussions, and use  $f$  to denote the total angular momentum quantum number, where the possible values of  $f$  are  $f = I \pm \frac{1}{2}$  for our case.

In a typical optical pumping process for our purpose, circularly polarized laser light along the  $z$ -direction, tuned to the  $D1$  line is used to interact with the alkali atoms.  $D1$  is the transition line between electron levels  $nS_{1/2}$  and  $nP_{1/2}$ , where  $n$ , the principle quantum number, has different values for different alkali metals. While either of the circular polarizations of the laser would work for the optical pumping, we assume the laser photons to be with  $\sigma^+$  helicity for simplicity. In the holding field, both the ground state  $S_{1/2}$  and excited state  $P_{1/2}$  split into two sublevels,  $S_z = 1/2$  and  $S_z = -1/2$  (Zeeman splitting). Due to the conservation of angular momentum, only the transition between  $S_z = -1/2$  sublevel of the ground state and the  $S_z = 1/2$  sublevel of the excited state is possible, given that the photons have  $\sigma^+$  helicity.

Once excited, the electrons decay back to  $S_{1/2}$ , either by spontaneous emission or by quenching collisions. The photons generated by the spontaneous emission are unpolarized, and would depolarize other alkali atoms. So, it's a widespread practice to add molecular gases (often  $N_2$ ) to “quench” the excited alkali atoms [8]—to collide with these atoms and absorb the extra energy into the rotational and vibrational

degrees of freedom of the quenching gas molecules. When the quenching decay is the dominant decay mechanism, the depolarizing effect of the spontaneous emission can be neglected, and the overall rate for the electron to decay from the excited state is typically on the order of  $10^9 \text{ sec}^{-1}$  ( $\text{ns}^{-1}$ ).

The quenching decay of excited electrons populates the two sublevels of the ground state with the same rate. So, the overall effect of an excitation-decay cycle would be pumping half of the  $S_z = -1/2$  electrons to the  $S_z = 1/2$  state. By putting the electrons through the cycle many times, most of the electrons are pumped to the  $S_z = 1/2$  state.

When the gas number density in the sample cell is high ( $\gtrsim 0.1$  amagat), the hyperfine structures of the alkali  $D1$  lines are unresolved due to collisional broadening of the lines. Therefore, the interaction between an alkali atom and a photon can only flip the electron spin, while the nuclear spin remains unchanged. As we'll see in the next subsection, the durations of the spin-exchange processes are not much longer than the hyperfine interaction timescale, and therefore do not significantly change the alkali nuclear polarization either. Under these conditions, it is a valid approximation to assume that the density matrix of the alkali atoms obeys the spin temperature distribution [29], that is, the distribution is determined by a single parameter  $\beta$ :

$$\rho = Z^{-1} \exp(\beta F_z) = Z^{-1} \exp(\beta I_z) \exp(\beta S_z), \quad (2.1)$$

where  $Z$  is the partition function. The electron polarization is defined as

$$P = 2\langle S_z \rangle = \frac{N_{|\text{spin-up}} - N_{|\text{spin-down}}}{N_{|\text{spin-up}} + N_{|\text{spin-down}}} = \frac{\exp(\beta/2) - \exp(-\beta/2)}{\exp(\beta/2) + \exp(-\beta/2)} = \tanh(\beta/2). \quad (2.2)$$

If we completely ignore the presence of the alkali nuclear spin, the evolution of the electron spin due to optical pumping would be

$$\frac{d}{dt}\langle S_z \rangle = R \left( \frac{1}{2} - \langle S_z \rangle \right), \quad (2.3)$$

where  $R$  is the mean photon absorption rate for unpolarized alkali atoms, and we have assumed the incident light has 100% circular polarization with helicity  $\sigma^+$ . The

above equation is straightforward, since an atom with electron spin down ( $\langle S_z \rangle = -1/2$ ) receives one unit of angular momentum from the photon, while a spin-up atom ( $\langle S_z \rangle = 1/2$ ) receives nothing.

However, the nuclear spin does interact with the electron spin, through the hyperfine interaction  $A\vec{I}\cdot\vec{S}$ , which roughly corresponds to a  $10^9 \sim 10^{10} \text{ sec}^{-1}$  evolution rate. So, between two consecutive sudden interactions (optical pumping or spin-exchange), the electron spin slowly transfers to the nuclear spin of alkali atoms. This process slows the build-up rate of the electron polarization by a factor  $1 + \bar{\epsilon}(P)$  which is defined as

$$1 + \bar{\epsilon}(P) = \sum_{\text{isotopes}} \frac{\langle F_z \rangle}{\langle S_z \rangle} = \sum_{\text{isotopes}} (1 + 2\langle \vec{I}\cdot\vec{I} - I_z^2 \rangle). \quad (2.4)$$

This slowdown factor is polarization-dependent, and is usually on the order of 1 to 10. So the actual electron spin evolution due to optical pumping is

$$\frac{d}{dt}\langle S_z \rangle = \frac{R}{1 + \bar{\epsilon}(P)}\left(\frac{1}{2} - \langle S_z \rangle\right). \quad (2.5)$$

Now the mean photon absorption rate for unpolarized atoms  $R$  is given by

$$R = \int_0^\infty \Phi(\nu)\sigma_{opt}(\nu)d\nu, \quad (2.6)$$

where  $\Phi(\nu)$  is the spectral distribution of the photon flux, and  $\sigma_{opt}(\nu)$  is the spectral distribution of the absorption cross section of the alkali atom.  $\Phi(\nu)$  usually takes a Gaussian form, with typical full width at half maximum (FWHM) ranging from  $10^{10}$  to  $10^{12}$  Hz. The term  $\sigma_{opt}(\nu)$  is commonly Lorentzian, for most cases its FWHM is dominated by the collisional broadening effect, and is proportional to the environmental gas density, with 1 amagat density corresponding to roughly  $2 \times 10^{10}$  Hz FWHM. The term  $\sigma_{opt}$  satisfies the relation

$$\int_{-\infty}^{\infty} \sigma_{opt}d\nu = \pi r_e c f, \quad (2.7)$$

where  $r_e = 2.82 \times 10^{-15}$  m is the classical radius of electron,  $c$  is the light speed, and  $f$  is the oscillator strength [28]. For  $D1$  lines,  $f \approx \frac{1}{3}$ .

Assume a typical SEOP scenario: using a diode laser beam with intensity of 3 Watts/cm<sup>2</sup>, and bandwidth of 600 GHz bandwidth, to pump unpolarized Rb atoms, and Xe and N<sub>2</sub> gases in the cell have an overall density of 1 amagat. If the laser frequency has been exactly tuned to the Rb *D1* line,  $R \approx 3 \times 10^6 \text{ sec}^{-1}$ . So, considering the slow-down factor  $1 + \bar{\epsilon}(P)$ , the spin build-up rate of alkali electron is usually on the order of  $10^5 \sim 10^6 \text{ sec}^{-1}$ . Because the photon flux  $\Phi$  decreases as the laser beam penetrates into the cell, the value of  $R$  will be smaller toward the back end of the cell.

As we will see in the next subsection, for our experimental conditions, the relaxation rate of  $S_z$  resulting from depolarizing mechanisms of alkali electron spin (collisions with other alkali atoms, interactions with noble gas and other gas molecules) is usually  $\lesssim 10^5 \text{ sec}^{-1}$ . So for our SEOP experiments, we can assume that the equilibrium value of the alkali electron polarization is close to 100%, throughout most of the cell volume. Close to the cell wall, the wall relaxation reduces the polarization to zero, but from the discussion in [7, 8], the thickness of this unpolarized layer is on the order of  $\sqrt{D/R} \lesssim 10^{-4}\text{m}$ , where  $D$  is the diffusion constant. Toward the back end of the cell, the alkali electron polarization might also be much smaller than 100% due to the reduced photon flux.

To avoid confusion with the noble gas nuclear polarization, we shall from now on denote the alkali electron polarization as  $P_{\text{alkali}}$ .

### 2.1.2 Spin-Exchange

Spin-exchange is the process of spin transferring between interacting particles. Here, the process that we're interested in, is specifically the spin-exchange between the spin of alkali metal valence electrons and <sup>129</sup>Xe nuclei. The new notations to be defined for this part are  $\vec{K}$ , the <sup>129</sup>Xe nuclear spin and  $\vec{N}$ , the orbital angular momentum of the system of two interacting particles (could be alkali-Xe system or alkali-buffer gas system). For clarity, the angular momenta discussed in this and the previous subsection have been plotted in Fig. 2.1.

For <sup>129</sup>Xe, there are two different mechanisms that can induce transfer of angular

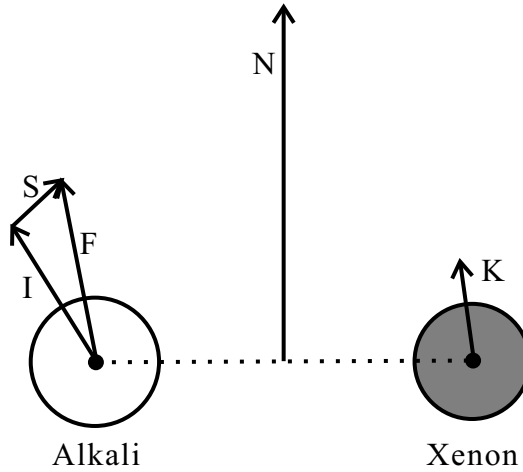


Figure 2.1: An illustration of the angular momenta discussed in the text:  $\vec{I}$ ,  $\vec{S}$ ,  $\vec{F}$ ,  $\vec{K}$ , and  $\vec{N}$ .

momentum between the alkali metal atom and the  $^{129}\text{Xe}$  atom, namely transfer during binary collisions and transfer by forming van der Waals molecules. The average duration of the binary collisions between the particles is on the order of  $10^{-12}$  sec. Regarding the vdW molecules, their average lifetime is inversely proportional to the number density of gases in the cell. For number densities  $\gtrsim 0.2$  amagat, this average lifetime is on the order of  $10^{-11}$  sec. As we have seen in subsection 2.1.1, the characteristic timescale for the alkali nuclear spin to precess is about  $10^{-9} \sim 10^{-10}$  sec, so most spin-exchanging processes do not change the nuclear spin of alkali metals. The assumptions leading to the spin-temperature representation in the last subsection are, therefore, justified.

The term in the Hamiltonian of the system that is related to the spin-exchange is the same for both mechanisms, and it has the form of  $\alpha \vec{K} \cdot \vec{S}$ , namely the interaction of two magnetic moments. During the interaction, the two angular momenta are coupled together, and due to the conservation of angular momentum, the only consequence of this term would be transfer of angular momentum between  $\vec{K}$  and  $\vec{S}$ . We should keep in mind that the spin-exchange term has different values for different isotopes of Xe. The only other natural isotope of Xe with non-zero nuclear spin is  $^{131}\text{Xe}$ , its nuclear spin is  $3/2$ . For our studies, the polarization of  $^{131}\text{Xe}$  is not interesting. We

will not discuss much about the spin-exchange between the alkali electron and  $^{131}\text{Xe}$ , except when referring to the depolarization of alkali electron spin.

There is another term  $\gamma\vec{N} \cdot \vec{S}$  in the Hamiltonian that transfers the alkali electron spin  $\vec{S}$  to the orbital angular momentum  $\vec{N}$ . This term does not contribute to the nuclear polarization of  $^{129}\text{Xe}$ , but does destroy the alkali electron polarization, so we will also discuss this mechanism. This spin-rotation interaction does not depend on the nuclear spin of Xe, i.e., it has the same value for all Xe isotopes. Because of the existence of this spin-rotation interaction, only a fraction of the angular momentum lost in  $\vec{S}$  goes to  $\vec{K}$ . The ratio of angular momentum that goes from  $\vec{S}$  to  $\vec{N}$  to that which goes to  $\vec{K}$  can be estimated as  $\frac{\gamma N}{\alpha}$ . This quantity has been measured by Zeng *et al.* to be approximately 3 for  $^{129}\text{Xe}$  with K, Rb, and Cs [11]. The measurements are for nitrogen dominated environments, but we can use them to estimate that for each unit of angular momentum lost in  $\vec{S}$  during an alkali- $^{129}\text{Xe}$  interaction, about 0.1  $\sim$  0.5 units go to  $\vec{K}$ . Considering other Xe isotopes, if we assume that the spin-exchange term for  $^{131}\text{Xe}$  is the same order of magnitude as for  $^{129}\text{Xe}$ , it can be estimated that for each unit of angular momentum lost from  $\vec{S}$  during interactions with Xe atoms, about 0.02  $\sim$  0.3 units go to the  $^{129}\text{Xe}$  nuclear spin. In the above estimate, we have assumed that we are using Xe with natural isotopic abundance, namely 26.4% of Xe atoms are  $^{129}\text{Xe}$  and 21.2% are  $^{131}\text{Xe}$ .

Since the binary collisions have very short durations, they can be considered as instantaneous, and can be described by the collisional cross sections:  $\langle v\sigma_{KS} \rangle$ , corresponding to the angular momentum that goes to  $\vec{K}$ , and  $\langle v\sigma_{NS} \rangle$ , corresponding to the angular momentum that is transferred to  $\vec{N}$ . The term  $\langle v\sigma_{NS} \rangle$  has different values for different particles that interact with alkali atoms, and will be specified by  $\langle v\sigma_{NS} \rangle_{\text{Xe}}$ ,  $\langle v\sigma_{NS} \rangle_{\text{N}_2}$ , etc. The relaxation rate of  $\vec{S}$  caused by these collisional mechanisms are, therefore,

$$\Gamma_{SD, \text{collisional}} = [\text{Xe}] \langle v\sigma_{NS} \rangle_{\text{Xe}} + [^{129}\text{Xe}] \langle v\sigma_{KS} \rangle_{^{129}\text{Xe}} + [^{131}\text{Xe}] \langle v\sigma_{KS} \rangle_{^{131}\text{Xe}} + [\text{N}_2] \langle v\sigma_{NS} \rangle_{\text{N}_2}, \quad (2.8)$$

where we have assumed that  $\text{N}_2$  is the only buffer gas in the sample cell. We have

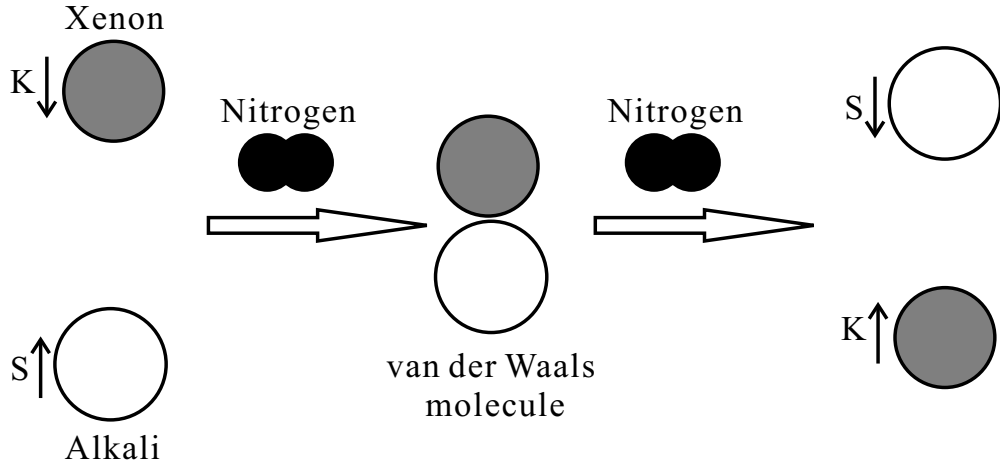


Figure 2.2: Formation and break-up of a van der Waals molecule. A nitrogen molecule acts as the third-party particle for both the formation and break-up processes.  $\vec{S}$  and  $\vec{K}$  are “exchanged” during the lifetime of the vdW molecule.

also introduced the use of pairs of brackets, “[ ],” to denote the number density of a certain particle. For Xe with natural isotopic abundance used in our experiments,  $[^{129}\text{Xe}] = 0.264[\text{Xe}]$ ,  $[^{131}\text{Xe}] = 0.212[\text{Xe}]$ .

To form or break a van der Waals molecule, a third-party particle has to be present to satisfy the conservation of energy and momentum in the system. The formation and break-up of a typical vdW molecule have been sketched in Fig. 2.2, where a nitrogen molecule acted as the third-party particle. In Fig. 2.2, the alkali electron spin and the  $^{129}\text{Xe}$  nuclear spin are “exchanged” during the lifetime of the molecule, but it should be noted that, due to the spin-rotation interaction, in many vdW molecules the loss in  $\vec{S}$  would go to  $\vec{N}$  instead of  $\vec{K}$ .

Since the frequency of the break-up of van der Waals molecules depends on the overall density of the gases that can act as the third-party particle, the mean lifetime of the vdW molecules depends on the density in the sample cell. For our experiments, where the overall density lies in the range of 0.2-0.7 amagat, the mean lifetime satisfies the conditions of being “short but not *very* short” as defined in [7].

The “short but not *very* short” lifetime is defined as a lifetime  $\tau$  that satisfies

$$\gamma N \tau / h \ll 1 \text{ and } \alpha \tau / h \ll 1, \quad (2.9)$$

but does not satisfy

$$\omega_{hf}\tau \ll 1, \quad (2.10)$$

where  $\gamma$  and  $\alpha$  are the coupling coefficients for spin-rotation and spin-exchange interactions, respectively, and  $\omega_{hf} \equiv [I]A/(2\hbar)$  is the hyperfine frequency. The relations (2.9) show that the average rotation angles of  $\vec{S}$  and  $\vec{K}$  during a lifetime of the vdW molecule are small. The relation (2.10) means that the lifetime is not negligibly short compared to the timescale for the evolution of the alkali nuclear spin  $\vec{I}$ , and thus the total angular momentum quantum number  $f$  is not changed during the vdW lifetime.

The rigorous derivation of the contribution of van der Waals molecules in the spin-exchange process and in the transfer of angular momentum between  $\vec{S}$  and  $\vec{N}$  is complicated. We will discuss more about this topic in the next section. Detailed discussions can also be found in the literature [7, 8, 20]. Naturally the spin-exchange rate resulting from vdW molecules depends on the cell density.

Hereafter, we shall use “Xe” in subscripts to stand for “ $^{129}\text{Xe}$ ” unless otherwise specified. So the polarization of the  $^{129}\text{Xe}$  nuclear spin  $\vec{K}$  is denoted by  $P_{\text{Xe}}$ . To characterize the time evolution of  $P_{\text{Xe}}$ , we define the spin-exchange rate  $\gamma_{SE}$  as the relaxation rate of  $\vec{K}$  resulting from the interaction with alkali atoms. The relaxation rate includes contributions both from binary collisions and from vdW molecules. We further define  $\Gamma_{\text{Xe}}$  as the relaxation rate of  $\vec{K}$  from other sources, mainly due to the interaction with the cell walls. As we will see in the next section,  $\gamma_{SE}$  depends on various quantities, but it is a constant for a cell with certain amounts of gases and at a certain temperature. The time evolution of  $P_{\text{Xe}}$  is, therefore,

$$\frac{d}{dt}P_{\text{Xe}} = (P_{\text{alkali}} - P_{\text{Xe}})\gamma_{SE} - P_{\text{Xe}}\Gamma_{\text{Xe}}. \quad (2.11)$$

To verify our assumption that for our experimental conditions, the polarization of  $\vec{S}$  is close to 100%, we can roughly estimate the relaxation rate of  $\vec{S}$  resulting from both spin-exchange interactions and spin-rotation interactions for typical situations. The relaxation rate of  $\vec{S}$  due to spin-exchange is related to the relaxation rate of  $\vec{K}$

due to the same mechanism by

$$\gamma_{\vec{S},spin-exchange} = \frac{[^{129}\text{Xe}]}{[\text{alkali}]} \gamma_{\vec{K},spin-exchange}, \quad (2.12)$$

where the subscripts  $\vec{S}$  and  $\vec{K}$  specify the quantities of the relaxation (We use the notation  $\gamma_{SE}$  without a subscript to stand for  $\gamma_{\vec{K},spin-exchange}$ ). For our typical situation,  $[\text{Xe}] = 0.35$  amagat. For our Xe with natural isotopic abundance, this corresponds to  $[^{129}\text{Xe}] \approx 0.1$  amagat  $\approx 2.5 \times 10^{24} \text{ m}^{-3}$ . Let  $[\text{N}_2] = 0.15$  amagat and  $[\text{alkali}] = 2.5 \times 10^{19} \text{ m}^{-3}$ . From our measurements to be shown in later chapters, the relaxation rates of  $\vec{K}$  in the presence of any of the three alkali metals K, Rb, or Cs is on the order of  $10^{-2} \text{ sec}^{-1}$ . From these numbers, we can estimate that  $\gamma_{\vec{S},spin-exchange}$  is on the order of  $10^3 \text{ sec}^{-1}$ .

As we have previously estimated, due to the presence of the spin-rotation interaction, the angular momentum lost in  $\vec{S}$  due to interaction with Xe atoms is about 3-50 times the gain in  $\vec{K}$  of  $^{129}\text{Xe}$ . So, the overall relaxation rate of  $\vec{S}$  resulting from interactions with noble gas atoms is one or two order of magnitude larger than  $\gamma_{\vec{S},spin-exchange}$ , or on the order of  $10^4 \sim 10^5 \text{ sec}^{-1}$ . Contributions from other relaxation mechanisms of  $\vec{S}$  are negligible. So the optical pumping rate of  $\vec{S}$ , which is  $10^5 \sim 10^6 \text{ sec}^{-1}$ , dominates over the other relaxation rates, and our assumption is justified.

$\Gamma_{\text{Xe}}$ , the rate of  $\vec{K}$ 's relaxation through mechanisms other than interactions with alkali atoms, is dominated by the wall relaxation for our case. From our measurements, this overall relaxation time is on the order of  $0.01 \text{ sec}^{-1}$ . Other major relaxation mechanisms include Xe-Xe interactions and inhomogeneities in magnetic field. According to the measurements by Chann *et al.* [32], the Xe-Xe interactions induce a relaxation rate in  $\vec{K}$  is given by

$$\Gamma_{\text{Xe-Xe}} = 6.7 \times 10^{-5} \text{ sec}^{-1} + 5.0 \times 10^{-6} [\text{Xe}] \text{ sec}^{-1}, \quad (2.13)$$

where  $[\text{Xe}]$  is measured in amagats.

The relaxation rate resulting from field inhomogeneities can be estimated as [30,

31]

$$\Gamma_{\Delta B} = D \frac{|\nabla B_{\perp}|^2}{B_0^2}, \quad (2.14)$$

where  $D$  is the diffusion constant,  $B_0$  is the holding field, and  $\nabla B_{\perp}$  is the field inhomogeneity in the plane perpendicular to the direction of  $\vec{B}_0$ . For our experimental condition,  $|\nabla B_{\perp}| \sim 0.01$  Gauss/cm when  $B_0 \sim 20$  Gauss, and  $D \sim 0.1$  cm<sup>2</sup>/sec. Therefore  $\Gamma_{\Delta B}$  is on the order of  $10^{-8}$  sec<sup>-1</sup>. Clearly, both  $\Gamma_{\text{Xe-Xe}}$  and  $\Gamma_{\Delta B}$  are negligible compared to the overall relaxation rate.

## 2.2 The Spin-Exchange Rate

As defined in the last section, the spin-exchange rate  $\gamma_{SE}$  is the relaxation rate of  $\vec{K}$  resulting from interactions with alkali atoms. Naturally,  $\gamma_{SE}$  is proportional to the number density of the alkali atoms. As we have discussed in the last subsection,  $\gamma_{SE}$  can be divided into two parts, corresponding to the two spin-exchange mechanisms. The van der Waals molecules part is dependent on the number density of gases (primarily Xe and N<sub>2</sub> in our case), while the binary collision part is density independent.

For a detailed derivation of the exact form of  $\gamma_{SE}$ , we will begin with the simple case when Xe is the only gas in the cell (the number density of alkali vapor is usually lower by at least 4 orders of magnitude, and can almost always be neglected compared to other gases), and the alkali metal is monoisotopic (having only one isotope). The binary collision part, as we stated in Sec. 2.1, can be characterized by a single parameter  $\langle v\sigma_{KS, \text{Xe-alkali}} \rangle$ , which is the velocity-averaged spin-exchange cross section. Since there will not be much discussion concerning  $\sigma_{NS}$  in the following parts, the simplified notation  $\sigma_{\text{Xe-alkali}}$  will be used for spin-exchange cross section. The binary collision part of  $\gamma_{SE}$  is therefore  $[\text{alkali}] \langle v\sigma_{\text{Xe-alkali}} \rangle$ . The term  $\sigma_{\text{Xe-alkali}}$  has slight temperature dependences.

The van der Waals contribution to  $\gamma_{SE}$  is proportional to  $1/T_{vdW, \text{Xe}}$ , the formation rate of vdW molecules per <sup>129</sup>Xe atom. According to [8], for the short molecular

lifetime limit, as defined by conditions (2.9) and (2.10), the spin-exchange interaction during vdW molecule interactions induces change in  $K_z$  with the form of

$$\frac{d}{dt}\langle K_z \rangle = \frac{1}{T_{vdW, Xe}} \left( \frac{\alpha\tau}{(2I+1)\hbar} \right)^2 [\langle \hat{K}^2 - K_z^2 \rangle \langle F_z \rangle - \langle \hat{F}^2 - F_z^2 \rangle \langle K_z \rangle], \quad (2.15)$$

where  $\alpha$  is the coefficient in the spin-exchange interaction,  $\tau$  is the mean lifetime of vdW molecules, and  $I$  is the alkali nuclear spin.

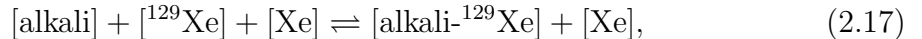
Semiclassically, we can view  $\frac{\alpha\tau}{(2I+1)\hbar}$  as the ‘‘mean rotation angle’’ of  $\vec{K}$  during the lifetime of a vdW molecule. Because this mean angle is small following Eq. (2.9), the ‘‘relative change’’ in  $K_z$  is roughly  $1 - \cos \frac{\alpha\tau}{(2I+1)\hbar} \approx \frac{1}{2} \left( \frac{\alpha\tau}{(2I+1)\hbar} \right)^2$ . Under the spin-temperature limit, the polarization of  $\vec{K}$  can be defined as  $P_{Xe} = \frac{K_z}{\langle \hat{K}^2 - K_z^2 \rangle}$ . (For a spin-1/2 system,  $\langle \hat{K}^2 - K_z^2 \rangle \equiv \frac{1}{2}$ .) Similarly, for the alkali atoms,  $P_{\text{alkali}} = \frac{F_z}{\langle \hat{F}^2 - F_z^2 \rangle} = \frac{S_z}{\langle \hat{S}^2 - S_z^2 \rangle} = 2\langle S_z \rangle$ .

Now we can simplify Eq. (2.15) to

$$\frac{dP_{Xe}}{dt} = \frac{1}{T_{vdW, Xe}} \left( \frac{\alpha\tau}{(2I+1)\hbar} \right)^2 \langle \hat{F}^2 - F_z^2 \rangle (P_{\text{alkali}} - P_{Xe}), \quad (2.16)$$

namely, the van der Waals part of  $\gamma_{SE}$  is  $\frac{1}{T_{vdW, Xe}} \left( \frac{\alpha\tau}{(2I+1)\hbar} \right)^2 \langle \hat{F}^2 - F_z^2 \rangle$ .

To further simplify the expression, we study the formation of van der Waals molecules



where  $[\text{alkali-}^{129}\text{Xe}]$  is the number density of the vdW molecules, and we have used the assumption that Xe is the only gas in the cell. When the reaction (2.17) reaches equilibrium, the molecule formation rate per  $^{129}\text{Xe}$  atom,  $1/T_{vdW, Xe}$ , and the break-up rate of vdW molecules,  $1/\tau$ , are related by

$$\frac{[^{129}\text{Xe}]}{T_{vdW, Xe}} = \frac{[\text{alkali-}^{129}\text{Xe}]}{\tau} = Z[\text{alkali}][^{129}\text{Xe}][\text{Xe}], \quad (2.18)$$

where  $Z$  is the rate constant for the reaction (2.17), and is independent of the number densities. The chemical equilibrium constant  $\kappa$  is also independent of the number densities, and is defined as

$$\kappa = \frac{[\text{alkali-}^{129}\text{Xe}]}{[\text{alkali}][^{129}\text{Xe}]} = \frac{[\text{alkali-Xe}]}{[\text{alkali}][\text{Xe}]}. \quad (2.19)$$

The second equality in (2.19) comes from the fact that the van der Waals interaction is the same for different Xe isotopes.

With the above relations, we find

$$\frac{\tau^2}{T_{vdW,Xe}} = \frac{[\text{alkali-}^{129}\text{Xe}]^2}{Z[\text{alkali}][^{129}\text{Xe}]^2[\text{Xe}]} = \frac{[\text{alkali}]}{Z[\text{Xe}]} \left( \frac{[\text{alkali-}^{129}\text{Xe}]}{[\text{alkali}][^{129}\text{Xe}]} \right)^2 = \frac{[\text{alkali}]}{[\text{Xe}]} \frac{\kappa^2}{Z}. \quad (2.20)$$

Now we can express the vdW part of  $\gamma_{SE}$  using only number densities, and density-independent quantities. We can also include all quantities that depend on the alkali nuclear spin in one single quantity by defining

$$\zeta \equiv \frac{\langle \hat{F}^2 - F_z^2 \rangle}{(2I + 1)^2}. \quad (2.21)$$

Using our assumption that  $P_{\text{alkali}}$  is close to 100% for our experimental conditions,  $\zeta$  can be simplified to

$$\zeta \rightarrow \frac{1}{4I + 2}. \quad (2.22)$$

Note that for our case,  $\zeta$  has different values with the cases when  $P_{\text{alkali}} \rightarrow 0$ , for example [20].

Now we can rewrite Eq. (2.16) as

$$\frac{dP_{Xe}}{dt} = \frac{[\text{alkali}]}{[\text{Xe}]} \frac{\kappa^2}{Z} \frac{\alpha^2}{\hbar^2} \zeta (P_{\text{alkali}} - P_{Xe}). \quad (2.23)$$

The vdW contribution to  $\gamma_{SE}$  is proportional to the alkali number density as expected, and is inversely proportional to the Xe number density. The latter relationship is because, when the Xe density increases, while the vdW molecule generation rate increases correspondingly, the lifetime of vdW molecules decreases. Since the vdW contribution to  $\gamma_{SE}$  is proportional to the generation rate of vdW molecules, and to the square of molecule lifetime, the probability of spin-exchange through vdW molecules is inversely proportional to the Xe density. The term  $\alpha$  characterizes the interactions between the alkali valence electron and the noble gas nucleus, it is independent of the isotopic species of the alkali, and is also independent of the number densities of the particles. The term  $Z$  is also a constant for any particular alkali. The quantity  $\frac{\kappa^2}{Z}$  is a constant for each alkali-Xe pair as well. So, the term  $\frac{\kappa^2 \alpha^2}{Z \hbar^2}$  in the relaxation rate is

a constant for each alkali-Xe pair. In discussions later in this section, we will see that this term needs to be slightly modified for the case when  $N_2$  is present in the sample cell. We follow the notation in [20] and define this term as  $\gamma_M \equiv \frac{\kappa^2 \alpha^2}{Z \hbar^2}$ .

From the above discussions, for the simplified situation where Xe is the only gas in the cell, and the alkali is monoisotopic,  $\gamma_{SE}$  has the form of

$$\gamma_{SE} = [\text{alkali}] \left( \langle v \sigma_{\text{Xe-alkali}} \rangle + \frac{\gamma_M \zeta}{[\text{Xe}]} \right). \quad (2.24)$$

The quantity  $\gamma_{SE}$ , together with  $\Gamma_{\text{Xe}}$ , the relaxation rate induced by mechanisms other than interactions with alkali atoms, governs the time evolution of  $P_{\text{Xe}}$  according to Eq. (2.11).

We can now generate our result for multi-isotopic alkalis. This is important because, among K, Rb, and Cs, three frequently used alkali for SEOP of  $^{129}\text{Xe}$ , only Cs is monoisotopic. Let different isotopes of the alkali be denoted by the subscript “ $i$ ,” and their relative abundances by  $f_i$ . The velocity-averaged spin-exchange cross section characterizing spin-exchange through binary collisions can be generalized to a weighted average over all isotopes,

$$\langle v \sigma_{\text{Xe-alkali}} \rangle = \sum_i f_i \langle v \sigma_{\text{Xe-alkali},i} \rangle. \quad (2.25)$$

For the spin-exchange rate coming from van der Waals molecules, the only quantity depending on the isotopic species is  $\zeta$ . So, for the multi-isotopic alkali cases, we do not have to change the entire Eq. (2.24) and only need to modify slightly the definition of  $\zeta$  from Eq. (2.21) to

$$\zeta \equiv \sum_i \frac{\langle \hat{F}_i^2 - F_{i,z}^2 \rangle}{(2I_i + 1)^2}. \quad (2.26)$$

For the limit when  $P_{\text{alkali}} \rightarrow 100\%$ , the approximate value of  $\zeta$  becomes

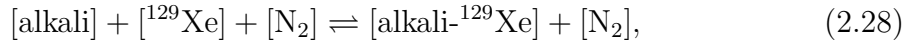
$$\zeta \approx \sum_i \frac{f_i}{4I_i + 2}. \quad (2.27)$$

For alkalis K, Rb, and Cs with natural isotopic abundances, we can numerically calculate the values of  $\zeta$  according to Eq. (2.27), with the results shown in Table 2.1. Note that these are different from the  $\zeta$  values in [20] where  $P_{\text{alkali}} \rightarrow 0$ .

alkali	K		Rb		Cs
isotope	<sup>39</sup> K	<sup>41</sup> K	<sup>85</sup> Rb	<sup>87</sup> Rb	<sup>133</sup> Cs
$I$	$\frac{3}{2}$	$\frac{3}{2}$	$\frac{5}{2}$	$\frac{3}{2}$	$\frac{7}{2}$
$f$	0.9326	0.0673	0.7215	0.2785	1
$\zeta$	0.125		0.0949		0.0625

Table 2.1: The nuclear spin  $I$  and relative abundance  $f$  of all major isotopes of the three alkalis K, Rb, and Cs. Values of  $\zeta$  are calculated from these quantities. Alkali electron polarizations of nearly 100% have been assumed.

To generalize the results to the experimental condition where  $N_2$  is also present in the cell as a buffer gas, we need to consider the formation of van der Waals molecules with  $N_2$  molecules acting as the third party particle,



in addition to reaction (2.17). For reaction (2.28), we have a different rate constant  $Z$ , so we can denote the  $Z$  for reaction (2.17) as  $Z_{\text{Xe}}$ , and the  $Z$  for reaction (2.28) as  $Z_{N_2}$ .

Eqs. (2.18) and (2.20) should now be respectively generalized to

$$\frac{[^{129}\text{Xe}]}{T_{vdW,\text{Xe}}} = \frac{[\text{alkali-}^{129}\text{Xe}]}{\tau} = Z_{\text{Xe}}[\text{alkali}][^{129}\text{Xe}]([Xe] + \frac{Z_{N_2}}{Z_{\text{Xe}}}[N_2]), \quad (2.29)$$

and

$$\frac{\tau^2}{T_{vdW,\text{Xe}}} = \left( \frac{[\text{alkali-}^{129}\text{Xe}]}{[\text{alkali}][^{129}\text{Xe}]} \right)^2 [\text{alkali}] / (Z_{\text{Xe}}([Xe] + \frac{Z_{N_2}}{Z_{\text{Xe}}}[N_2])) = \frac{\kappa^2}{Z_{\text{Xe}}} [\text{alkali}] / ([Xe] + \frac{Z_{N_2}}{Z_{\text{Xe}}}[N_2]). \quad (2.30)$$

Our generalization would not change the value of  $\kappa$ , since the third party particle appears on both side of reactions (2.17) or (2.28). So, if we stick to the definition of  $\gamma_M$  as  $\gamma_M \equiv \kappa^2 \alpha^2 / (Z_{\text{Xe}} \hbar^2)$ , and for convenience make the definition  $b \equiv Z_{N_2} / Z_{\text{Xe}}$ , Eq. (2.24) now becomes

$$\gamma_{SE} = [\text{alkali}] \left( \langle v \sigma_{\text{Xe-alkali}} \rangle + \frac{\gamma_M \zeta}{[Xe] + b[N_2]} \right), \quad (2.31)$$

where  $\langle v\sigma_{\text{Xe-alkali}} \rangle$  and  $\zeta$  have been generalized according to the above discussions.

Eq. (2.31) is the final form of the  $\gamma_{SE}$  for our experimental conditions, and will be used to analyze data from our measurements.

## 2.3 Nuclear Magnetic Resonance (NMR) and Magnetic Resonance Imaging (MRI)

Nuclear Magnetic Resonance (NMR) is defined as the selective absorption of radio frequency (RF) radiation by an atomic nucleus in an external magnetic field. It is a very useful way for studying various properties of nuclei with non-zero spin. Throughout our projects, we used NMR techniques to measure the nuclear polarization of our laser-polarized  $^{129}\text{Xe}$  sample. We will discuss the fundamental NMR principles in subsection 2.3.1.

Magnetic Resonance Imaging (MRI), an application of NMR, has by now become one of the routine medical diagnostic methods. Compared to other approaches, it has the advantages of being non-invasive, ultra fast ( $<1$  sec), having high resolution (on the scale of millimeters), providing images in multiple dimensions with a single scan, and can be done *in vivo*. MRI is particularly useful for the diagnosis of many brain diseases, as well as arthritis, and a number of other diseases afflicting tissues and muscles. Other than applications in medical diagnosis, MRI can also be used in various material studies (e.g., study of the permeability in porous media [33]). In Ch. 4 we will present a project using laser-polarized  $^{129}\text{Xe}$  to perform MRI. Some basic MRI techniques will be briefly introduced in subsection 2.3.2 for preparation.

### 2.3.1 NMR Principles

Nuclear Magnetic Resonance (NMR) [24, 34] was first discovered in 1946 by F. Bloch and E. Purcell, who later received the Nobel prize for the discovery. As is well-known by now, in an external field (“holding field”)  $B_0\hat{z}$ , the nuclear magneton has the energy of  $E = -\mu \cdot \vec{B}_0$ . The gyromagnetic ratio  $\gamma$  of this specific nucleus is defined as the

nuclear magneton  $\mu$  divided by the nuclear spin angular momentum  $I\hbar$ . Considering the quantization of  $I_z$ , the possible values of  $E$  become

$$E = \gamma m \hbar B_0, \quad (m = -I, -I + 1, \dots, I), \quad (2.32)$$

where  $m \equiv I_z$  is the magnetic quantum number in the direction of the external field. The energy difference between two adjacent levels becomes  $\Delta E = \gamma \hbar B_0$ . Therefore, for a photon to excite transitions between two adjacent levels, its minimum energy is  $E_\gamma = \hbar\omega = \gamma \hbar B_0$ , and the lowest RF frequency that can induce nuclear magnetic resonance is

$$\omega_0 = \gamma B_0. \quad (2.33)$$

This is the Larmor equation for NMR, and the frequency  $\omega_0$  is the Larmor frequency, which is also the precession frequency of the nucleus about  $\vec{B}_0$ .

In an external magnetic field, quantum states with different  $m$  values correspond to different energies. According to the Boltzmann distribution, the populations of different  $m$ -states would be different, and the nuclear spin would be polarized. For a typical spin-1/2 system, at temperature  $T$ , the thermal polarization becomes

$$P = 2\langle m \rangle = \frac{N|_{\text{spin-up}} - N|_{\text{spin-down}}}{N|_{\text{spin-up}} + N|_{\text{spin-down}}} = \frac{\exp(\frac{\mu B}{kT}) - \exp(-\frac{\mu B}{kT})}{\exp(\frac{\mu B}{kT}) + \exp(-\frac{\mu B}{kT})} = \tanh(\frac{\mu B}{kT}) \approx \frac{\mu B}{kT}, \quad (2.34)$$

where the last approximation comes from the fact that under all practical circumstances, the quantity  $\frac{\mu B}{kT}$  is far smaller than unity. This thermal polarization is usually exploited in conventional NMR. We can see that to achieve a high polarization, it is desirable to have a high magnetic field and/or a low temperature. For NMR using laser-polarized  $^{129}\text{Xe}$ , however, the polarization of the nuclear spin is independent of the magnetic field or the temperature. We will see that the size of the NMR signal is proportional to  $P$ . So, laser-polarized  $^{129}\text{Xe}$  NMR has the advantage over conventional MRI in that it doesn't require high fields or low temperatures, and can thus greatly reduce the cost.

In equilibrium, a thermally polarized sample of nuclei has the magnetization of

$$\vec{M}_0 = PN\mu\hat{z}, \quad (2.35)$$

where  $P$  is the nuclear polarization given by Eq. (2.34),  $N$  is the total number of nuclei in the sample, and  $\mu$  is the magneton of a single nucleus. The magnetization of laser-induced polarization for  $^{129}\text{Xe}$  has the same form, as long as the magnetization is aligned with  $\vec{B}_0$ , even though the polarization  $P$  is no longer the thermal polarization. The above magnetizations are in  $z$ -direction, and do not precess. To generate detectable signals, it is necessary to “tip” the magnetization  $\vec{M}$  away from the  $z$ -direction, so that it precesses around  $z$ -direction, and induce signals in pickup coils. For this purpose, a rotating magnetic field is usually applied.

In the context of NMR, it is often convenient to introduce a rotating frame of reference, which shares the  $z$ -axis with the laboratory frame, but have  $x$  and  $y$  axes rotating about  $z$  axis at a certain angular frequency  $\omega$ . To distinguish from the laboratory frame axes, we use  $x'$  and  $y'$  to denote the axes in the rotating frame.

If, in addition to the holding field  $\vec{B}_0$ , there exists another magnetic field  $\vec{B}_1$  perpendicular to  $\vec{B}_0$ , and  $\vec{B}_1$  rotates about the  $z$ -axis at the Larmor frequency of the holding field  $\omega_0 = \gamma B_0$ , we can study the effects of  $\vec{B}_1$  on the nuclear magnetons in the rotating frame. Let the frame rotate at the same frequency as  $\vec{B}_1$ . Then, without considering  $\vec{B}_1$ , the magnetization  $\vec{M}$  would be at rest with respect to the rotating frame. Now  $\vec{B}_1$  is also static in the rotating frame, so  $\vec{M}$  would precess about the direction of  $\vec{B}_1$ , at the frequency  $\omega_1 = \gamma B_1$ . By applying the rotating field  $\vec{B}_1$  for a short duration  $\Delta t_1$ , the direction of the magnetons precesses by  $\alpha = \gamma B_1 \Delta t_1$  away from the  $z$ -direction. Shown in Fig. 2.3 is a magnetization “tipped away” from the  $z$ -axis.

When  $\vec{M}$  is tipped away from  $z$ -direction, it precesses about the  $z$  axis at the Larmor frequency  $\gamma B_0$ . If pickup coils are placed near the sample of nuclei, the precessing magnetization causes variations in the magnetic flux through the coils, and induces a signal  $s(t)$  in the coils

$$s(t) = C\omega_0 M \sin \alpha \exp(-i\omega_0 t), \quad (2.36)$$

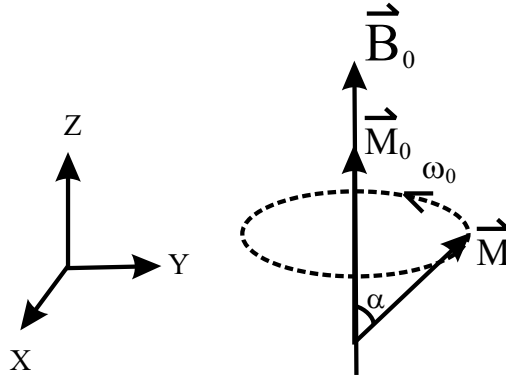


Figure 2.3: A magnetization  $\vec{M}$  is tipped away from its initial direction by angle  $\alpha$ , it subsequently precesses about the holding magnetic field  $B_0\hat{z}$  at the Larmor frequency. The rotating field  $B_1$  used to tip the magnetization is not explicitly shown.

where  $C$  is a constant determined by the coils' geometrical properties. The signal  $s(t)$  is an AC signal at the Larmor frequency, and its amplitude is proportional to the magnetization, the frequency, and  $\sin \alpha$ , where  $\alpha$  is the tip angle. We can see that  $s$  is proportional to the nuclear polarization  $P$ , since  $M$  is given by Eq. (2.35).

When  $\vec{M}$  is tipped away from its equilibrium value, it tends to relax back. The time evolution of  $\vec{M}$  is described by the Bloch equation [35],

$$\frac{d}{dt}\vec{M} = \vec{M} \times \gamma\vec{B}_0 - \frac{M_x\hat{x} + M_y\hat{y}}{T_2} - \frac{(M_z - M_0)\hat{z}}{T_1}, \quad (2.37)$$

where the first term on the right-hand side is the precession about  $\vec{B}_0$ , and the last two terms govern the relaxation of  $\vec{M}$ .  $T_1$  is the “longitudinal” relaxation time, and  $T_2$  is the “transverse” relaxation time. For most situations  $T_2 \leq T_1$ .  $M_0\hat{z}$  is the equilibrium value of  $\vec{M}$ , given by Eq. (2.35).

The longitudinal relaxation (sometimes called the “ $T_1$  process”) results from magnetic fields experienced by the nuclei that vary at the Larmor frequency  $\omega_0$ . Most time-varying magnetic fields have components at the Larmor frequency, so practically all time-varying fields contribute to the relaxation. In gaseous or liquid samples, the nuclei perform a random-walk in the field, so spatial field gradients are viewed by the nuclei as time-varying fields, and induces longitudinal relaxation of the magnetization as well. For the transverse relaxation (“ $T_2$  process”), the relaxation mechanisms for

longitudinal relaxation are still present, and there is also an additional mechanism, the decoherence of the magnetization. The sample magnetization consists of many nuclear magnetons. Each magneton experiences a slightly different holding field  $B_0$ , so each has a slightly different precession frequency. With time, the directions of the transverse components of these magnetons disperse on the  $x$ - $y$  plane, and their vector sum, the overall magnetization, decays due to the dispersion.

For the NMR of protons in water, which is the most frequently exploited NMR for imaging,  $T_1$  is typically on the order of  $0.1 \sim 1$  sec, and  $T_2$  is on the order of  $0.01 \sim 0.1$  sec. Both relaxation times vary with the environment of the sample. For pure water,  $T_1$  can be up to 2 sec [36]. Therefore, the signal-acquisition time should be generally within several  $T_2$  times, to obtain a good signal-to-noise ratio (SNR). And the duration of the rotating field  $\vec{B}_1$  field applied to tip the magnetization should be much smaller than  $T_2$ .

There is a difference between NMR using laser-polarized  $^{129}\text{Xe}$  and conventional NMR exploiting thermal polarizations of nuclei. The magnetization of laser-polarized  $^{129}\text{Xe}$  is much larger than the equilibrium value of magnetization resulting from the Boltzmann distribution given in Eq. (2.34). For instance, at room temperature (300 K), with a holding field  $B_0 = 1$  Tesla, the thermal polarization of  $^{129}\text{Xe}$  is  $P \approx \mu B / (kT) \approx 1.5 \times 10^{-7}$ , whereas the laser-induced polarization is usually on the order of 0.01 or even 0.1. So, for laser-polarized NMR, the equilibrium magnetization is about  $10^5$  times smaller than the initial magnetization, and is effectively zero. Also, the longitudinal relaxation time  $T_1$  for laser-polarized gaseous  $^{129}\text{Xe}$  is on the order of seconds to tens of seconds [37], much longer than the proton relaxation times.

In many NMR and MRI applications, the sample's magnetization is tipped away from the  $z$ -direction multiple times, producing one signal each time, and between two consecutive signal acquisitions, the magnetization is allowed a time on the order of  $T_1$  to restore its equilibrium value. For thermal magnetizations, the tip angle  $\alpha$  is often chosen to be  $\pi/2$  since the signal is proportional to  $\sin \alpha$  (Eq. (2.36)). However, when laser-induced magnetizations are used, choosing  $\alpha = \pi/2$  would completely destroy the longitudinal polarization, and make subsequent signal acquisitions impossible.

Therefore, small  $\alpha$  values are usually used for laser-polarized noble gases.

We now briefly discuss two common NMR techniques that have been applied in the projects to be presented in this thesis: free induction decay (FID) and adiabatic fast passage (AFP).

Free induction decay (FID) refers to the signal acquisition practice of tipping the magnetization from the  $z$ -direction by an angle  $\alpha$ , then allowing the transverse magnetization to decay at the rate of  $1/T_2$ , and finally recording the signals induced in pickup coils. The signals have the form

$$s(t) = C\omega_0 M_0 e^{-t/T_2} \sin \alpha \exp(-i\omega_0 t), \quad (2.38)$$

where  $C$  is the pickup coil constant as in Eq. (2.36), and  $M_0$  is the magnetization before being tipped, given by Eq. (2.35). The FID signals can be used to get information on  $T_2$  and  $M_0$ . The latter, in turn, can be used to calculate the nuclear polarization  $P$ .

Adiabatic fast passage (AFP) is another technique often used to measure the nuclear polarization  $P$ . To induce an AFP signal, the rotating field  $B_1$  is kept on, but its rotating frequency is deliberately set to be off resonance with the holding field (i.e.,  $\omega_{B_1} \neq \omega_0 \equiv \gamma B_0$ ). During the data acquisition, either  $B_0$  or  $\omega_{B_1}$  is swept past the resonance point. For our tests,  $\omega_{B_1}$  remains constant, and  $B_0$  is swept at a constant rate.

In the reference frame rotating at the frequency  $\omega_{B_1}$ , the Bloch equation (2.37) becomes

$$\left(\frac{d}{dt}\right)' \vec{M} = \vec{M} \times \gamma \vec{B} - \vec{M} \times \omega_{B_1} \hat{z} - \frac{M_x \hat{x} + M_y \hat{y}}{T_2} - \frac{(M_z - M_0) \hat{z}}{T_1}, \quad (2.39)$$

where the prime denotes the time-derivative in the rotating frame, and  $\vec{B}$  is the superposition of  $\vec{B}_0$  and  $\vec{B}_1$ . We can arbitrarily define the  $x'$ -direction of the rotation frame to be aligned with  $\vec{B}_1$ , so  $\vec{B}_1 = B_1 \hat{x}'$ . The above equation can be written as

$$\left(\frac{d}{dt}\right)' \vec{M} = \vec{M} \times \gamma \vec{B}_{eff} + \text{relaxation terms}, \quad (2.40)$$

where the effective field

$$\vec{B}_{eff} \equiv (B_0 - \omega_{B_1}/\gamma) \hat{z} - B_1 \hat{x}'. \quad (2.41)$$

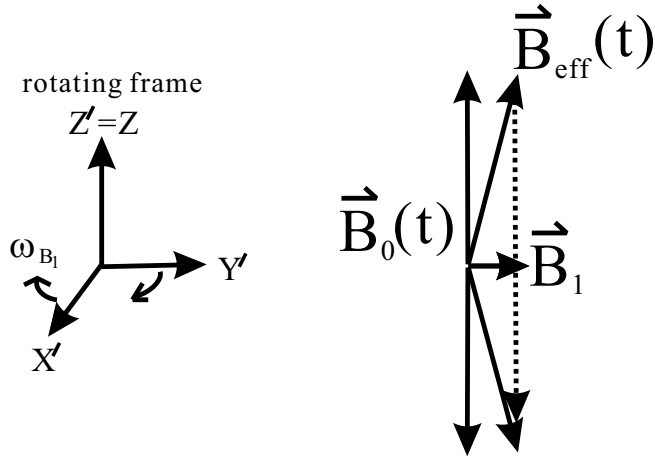


Figure 2.4: The time evolution of  $\vec{B}_{eff}$  in the rotating frame. When  $B_0$  is swept across the resonance point  $B_0 = \omega_{B_1}/\gamma$ ,  $\vec{B}_{eff}$  traverses the  $x$ - $y$  plane.

The magnitude of  $B_1$  is normally much smaller than  $B_0$ , so when  $B_0$  is swept across the value  $\omega_{B_1}/\gamma$ ,  $\vec{B}_{eff}$  is rotated from near the  $+z$ -direction to near the  $-z$ -direction. Fig. 2.4 shows the time evolution of  $\vec{B}_{eff}$  near the resonance point.

For the process to become an “adiabatic fast passage,” both the “adiabatic condition” and the “fast condition” must be satisfied. The adiabatic condition ensures that the rotation of  $\vec{B}_{eff}$  is much slower than the precession rate of the magnetization  $\vec{M}$ , so that  $\vec{M}$  follows the direction of  $\vec{B}_{eff}$ . The fast condition requires the rotation of  $\vec{B}_{eff}$  to be much faster than the relaxation rates, so that the relaxational loss of  $|M|$  during the passage is negligible. These conditions are, respectively,

$$\left(\frac{dB_0}{dt} / B_1\right) \ll \omega_0 \equiv \gamma B_0, \quad (2.42)$$

and

$$\left(\frac{dB_0}{dt} / B_1\right) \gg 1/T_1. \quad (2.43)$$

Note that although the transverse relaxation rate  $1/T_2$  is the greater of the two relaxation rates, as long as the passage is adiabatic, the magnetization would follow the direction of the effective field, and would not have a significant component on the transverse direction with respect to the effective field.

When these conditions are satisfied,  $\vec{M}$  follows  $\vec{B}_{eff}$  exactly with minimal loss. The signal induced in the pickup coils becomes

$$s(t) = C \exp(-i\omega_0 t) \omega_0 M_0 \left( \frac{\vec{B}_{eff}}{B_{eff}} \cdot \hat{x}' \right), \quad (2.44)$$

where  $M_0$  is the magnetization before adiabatic fast passage, and  $M_0 \left( \frac{\vec{B}_{eff}}{B_{eff}} \cdot \hat{x}' \right)$  is its projection onto the  $x$ - $y$  plane. If  $\vec{B}_0$  is swept at a constant rate, and the time of the resonance is defined as  $t = 0$ , we have  $\vec{B}_{eff}(t) = bt\hat{z} + B_1\hat{x}'$  where  $b$  is the constant sweeping rate of  $\vec{B}_0$ . The magnitude of  $s(t)$  can now be written as

$$|s(t)| = C\omega_0 M_0 \frac{B_1}{\sqrt{B_1^2 + (bt)^2}}. \quad (2.45)$$

This is similar to a Lorentzian signal, with the peak value  $C\omega_0 M_0$  proportional to the nuclear polarization  $P$ .

Presented above is only a small fraction of the theory of NMR. Much more on this topic can be found in A. Abragam's *The Principles of Nuclear Magnetism* [34].

### 2.3.2 Basics of MRI

To use NMR signals to create images, it is necessary to encode information about spatial positions into the resonance signals. The common approach to achieve this information encoding is to introduce gradients in the holding field  $\vec{B}_0$ . We define  $\vec{B}_{000} = B_{000}\hat{z}$  as the magnetic field at the origin point of the laboratory frame ( $x = y = z = 0$ ), and denote the field gradient by  $\vec{G} = (G_x, G_y, G_z)$ . So now

$$\vec{B}_0 = (B_{000} + \vec{G} \cdot (x, y, z))\hat{z}. \quad (2.46)$$

The field gradient is usually small, i.e.,  $\vec{G} \cdot (x, y, z) \ll B_{000}$  throughout the sample.

Various techniques have been developed for different imaging modalities. The field gradients in three directions could be carefully programmed into certain pulse sequences, to be on and off at different stages, with different durations. A large number of MRI techniques fall in the category of Fourier transform imaging, which

uses Fourier transformations to “decode” the NMR signals into images. The two-dimensional Fourier transform imaging (2DFT imaging) is simple, yet very helpful in understanding the principles of MRI.

In a 2DFT imaging process, the first step is to select a thin “slice” in the three-dimensional body to be imaged, and create the two-dimensional image for the slice. The other slices are imaged subsequently, so that the 3D image of the full body can be reconstructed. To select the slice, we can choose to tip the magnetization on the slice by a certain angle, while leaving the magnetization on other slices unaffected. As a result, the signal to be observed afterwards becomes the free induction decay of the magnetization in the selected slice. For this purpose, a field gradient in the  $z$ -direction is applied while the rotating field  $\vec{B}_1$  is used to tip the magnetization. Only the slice with  $B_0 \sim \omega_{B_1}/\gamma$  is significantly tipped. This step is called “slice selection” or “selective excitation.”

To make sure that the selected slice can be clearly distinguished from the neighbouring slices, it is a common practice to choose the magnitude of  $\vec{B}_1$  to have a sinc profile  $\frac{\sin(kt)}{kt}$ . The Fourier transformation of a sinc function is a square waveform ( $F(\omega) = \text{const}$ ,  $|\omega - \omega_{B_1}| \leq k$ ;  $F(\omega) = 0$ , otherwise). So the slice with  $B_0$  within  $\omega_{B_1}/\gamma \pm k/\gamma$  is selected, the slice thickness is  $2k/(\gamma G_z)$ .

As  $B_1 \ll B_0$ , the effective magnetic field in the rotating frame ( $\vec{B}_{eff}$ , as defined in Eq. (2.41)) by which the magnetization precesses is close to  $\vec{B}_1$  only when  $B_0$  is very near the resonance point  $\omega_{B_1}/\gamma$ . So it is safe to neglect the contribution from magnetizations outside of the selected slice.

After the slice selection is done, both the rotating field  $\vec{B}_1$  and the gradient in the  $z$ -direction,  $G_z$ , are turned off. The remaining work is to create a two-dimensional image for the slice. There are two ways to encode spatial information in the FID signals of the slice: frequency encoding and phase encoding.

If a field gradient exists in the  $x$ -direction when the resonance signals (FID signals with the form of Eq. (2.38)) are recorded, different  $x$ -positions correspond to different frequency components. This is the principle of frequency encoding. If  $\vec{B}_0 = (B_{000} +$

$G_x x) \hat{z}$ , the overall signal has the form of

$$\begin{aligned} s(t) &= \int_{x,y} dx dy C(\omega_0 + \gamma G_x x) M_0(x, y) e^{-t/T_2} \sin \alpha \exp(-i(\omega_0 + \gamma G_x x)t) \\ &\approx C\omega_0 e^{-t/T_2} \sin \alpha \int_{x,y} dx dy M_0(x, y) \exp(-i(\omega_0 + \gamma G_x x)t) \end{aligned} \quad (2.47)$$

where  $M_0(x, y)$  is the spatial distribution of the nuclear magnetization in the slice before the tipping process. The approximation above comes from the fact that the field gradient is small. A simple Fourier analysis can separate the components with different frequencies. The magnitude of the component with  $\omega = \omega_0 + \delta\omega$  is proportional to  $\int_y dy M_0(x = \delta\omega/(\gamma G_x), y)$ .

To further separate the magnetizations with same  $x$ -coordinate but different  $y$ 's, the phase encoding is applied. The phase encoding actually occurs before the frequency encoding, between the tipping process and the recording of resonance signals. If the field gradient in the  $y$ -direction has been applied for a fixed duration  $\Delta t$  by the time of signal acquisitions, a relative phase difference is introduced in the precession of the magnetization at different  $y$  positions

$$\Delta\phi(y) = \phi(y) - \phi(0) = \gamma G_y y \Delta t, \quad (2.48)$$

where we have assumed the gradient  $G_y$  is a constant for simplicity. In reality, the gradients can be programmed to vary with time.

Combining the frequency encoding and phase encoding techniques above, we find the final size of the signal to be

$$C\omega_0 e^{-t/T_2} \sin \alpha \int_{x,y} dx dy M_0(x, y) \exp(-i[(\omega_0 + \gamma G_x x)t + \gamma \Delta t G_y y]). \quad (2.49)$$

A certain frequency component with  $\omega = \omega_0 + \delta\omega$  now has a magnitude proportional to

$$\int_y dy M_0(x = \delta\omega/(\gamma G_x), y) \exp(-i(\gamma \Delta t G_y)y), \quad (2.50)$$

so  $M_0(x, y)$  can be calculated from another Fourier transformation. The above choice of encoding  $x$  information in the frequency and  $y$  information in the phase is, of

course, arbitrary. In addition to the above basic 2DFT approach, there are other more complicated 2DFT techniques, e.g., spin echo 2DFT [38].

To better illustrate the imaging process, the different pulses (rotating field, gradients in three directions, etc.) are often plotted versus time in graphs called “timing diagrams.” For example, the above 2DFT process corresponds to the timing diagram shown in Fig. 2.5.

By varying the pulse sequence, other imaging techniques could be designed, but these are not so relevant with the research results that are to be presented here.

Since the signals used for MRI are FID signals, the signal-to-noise ratio for MRI is also directly proportional to the spin polarization of the nuclei used for imaging. In conventional MRI using thermal polarizations, much of the hardware cost goes to the high-field magnets. If laser-polarized  $^{129}\text{Xe}$  is used as the imaging agent, the requirement on the magnetic field can be lowered by orders of magnitude, and the MRI cost would be greatly reduced.

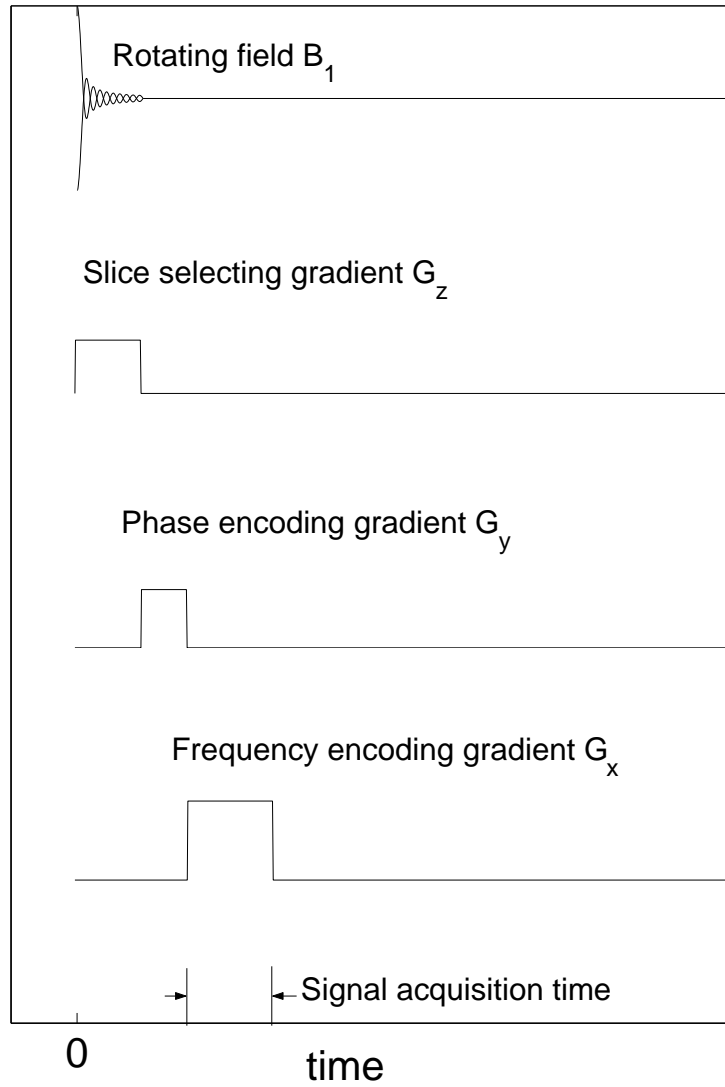


Figure 2.5: The timing diagram of the 2DFT process introduced in the text. The relative time durations and relative gradient magnitudes are not drawn to scale. The resonance signals are recorded during the “signal acquisition time” marked in the diagram.

## Chapter 3

# Experiments I: Measurements of Spin-Exchange Rate Constants

As we have discussed, measurements of the spin-exchange rate constants  $\langle v\sigma_{\text{Xe-alkali}} \rangle$ ,  $\gamma_M$ , and  $b$  are important for optimizing the production of laser-polarized  $^{129}\text{Xe}$ . We have measured these constants between  $^{129}\text{Xe}$  and three alkali metals K, Rb, and Cs, for cell densities in the range of 0.2-0.7 amagats. This project will be presented, in detail, in this chapter. Sec. 3.1 introduces the experimental setup for the measurements, including the optical, electronic, and heating system. Sec. 3.2 discusses how adiabatic fast passage (AFP) signals from the polarized sample are used to derive the values of  $\gamma_{SE}/[\text{alkali}]$ , the spin-exchange relaxation rate of  $^{129}\text{Xe}$  polarization per alkali atom. To get more accurate results, we have applied the Faraday rotation method to measure directly the densities of the alkali metals, these supporting measurements will be presented in Sec. 3.3. The  $\gamma_{SE}/[\text{alkali}]$  data are analyzed in Sec. 3.4 in order to determine the constants  $\langle v\sigma_{\text{Xe-alkali}} \rangle$ ,  $\gamma_M$ , and  $b$ . The error analysis and some discussions of the project will also be presented in Sec. 3.4.

The measurements of the spin-exchange rate constants in this chapter do not involve the absolute determination of the nuclear polarization of the  $^{129}\text{Xe}$  samples, so we will not discuss the methods to measure nuclear polarization (“polarimetry” methods) in this chapter, and will postpone the discussion to Ch. 4. Also, since the measurements in this project do not require optimized  $^{129}\text{Xe}$  polarizations, the discussions regarding the vacuum system for producing polarized  $^{129}\text{Xe}$  glass sample

cells, and the cell preparations for optimizing the maximum achievable polarization, will also be left until Ch. 4.

### 3.1 Experimental Setup

The central experimental setup of our measurements included an optical setup and an electronics setup. The optical setup mainly consisted of lasers, polarizing optics, and mirrors and lenses for manipulating the laser beam so that it covered the sample cell evenly. The electronics setup included the NMR coils that provided the holding field and the rotating field, the coils that received the NMR signals, electronic devices supplying the power for the coils, a pre-amplifier, a lock-in amplifier for separating the frequency component that we wanted from the raw signals, and a PC to control the signal acquisition and to record the data. The cell-building will be discussed in Ch. 4, here we will simply state that the alkali metals we used were produced by Alfa Aesar, they had chemical purities of 99.95%, 99.75%, and 99.98% for K, Rb, and Cs respectively. For the gases  $N_2$  and Xe, we used research grade gases produced by Spectra Gases, with natural isotopic abundances (99.6%  $^{14}N$  for  $N_2$ , 26.4%  $^{129}Xe$  for Xe). The cells we used for this project were cylindrical ones, different with the spherical cells used in Ch. 4. The cylindrical cells had diameters of 2.5 cm, and lengths 7.5 cm (1 inch by 3 inch).

For the measurements of the Rb- $^{129}Xe$  pair, a diode laser (FAP-system<sup>TM</sup>) manufactured by Coherent was used. The diode laser had a fixed 795 nm wavelength, 30 Watt output and 550 GHz linewidth. The diode laser was easy to use and maintenance-free, but its wavelength could not be adjusted over a wide range. For the measurements concerning K- $^{129}Xe$  and Cs- $^{129}Xe$  pairs, which required laser wavelengths of 770 nm and 894 nm, respectively, a Spectra Physics Ti:Sapphire laser was used. The Ti:Sapphire laser was pumped by an Ar ion laser (Ar<sup>+</sup> laser), its output wavelength could be tuned over the range of 700~1000 nm. The maximum output power of the Ti:Sapphire laser was about 5 Watt at 770 nm, or 3 Watt at 894 nm, and its linewidth was about 40 GHz. Since a high nuclear polarization of  $^{129}Xe$  was

not our primary concern, we did not use multiple lasers to pump our cells. The output beams of the lasers had linear polarizations. To obtain circular polarized beams needed for spin-exchange optical pumping of  $^{129}\text{Xe}$ , an accessorial circular polarizer was used for the diode laser output, and a quarter ( $\lambda/4$ ) waveplate was inserted in the path of the Ti:Sapphire laser beam. The diode laser system did not require a water cooling system, and could be easily moved. The fiber output of the diode laser was placed about 1 m from the sample cell. The Ti:Sapphire laser and  $\text{Ar}^+$  laser were fixed on an optical table about 5 m away from the cell, and a mirror was used to guide the beam to the cell. The diode laser beam had a circular cross section, with a diameter of about 3 cm, so it could evenly cover the cell with a 2.5 cm diameter. But the Ti:Sapphire laser beam had a smaller size, its diameter was  $\lesssim 1$  cm even with its divergence during propagation to the cell. Therefore, a concave lens was applied to the Ti:Sapphire laser beam to expand it to about 3 cm by the time it reached the cell. The optical setup for the Ti:Sapphire laser is shown in Fig. 3.1. The setup for the diode laser is simple and is not sketched.

To perform AFP [34] tests for the sample cell, three pairs of coils in orthogonal directions were used. A pair of Helmholtz coils with a diameter of 1.4 m were used to generate the holding magnetic field ( $B_0\hat{z}$ ). A second pair of coils, in a direction perpendicular to the holding coils, provided field  $\vec{B}_1$  that rotated at radio frequency (27.6 kHz for our tests). These two coils are called “radio frequency (RF) drive coils.” A third pair of coils called “pickup coils,” in the third orthogonal direction, picked up the induced resonance signals. The coil system was essentially same with what had been used in the neutron spin structure function measurements at the Stanford Linear Accelerator Center (SLAC) [3, 39, 40, 41]. Fig. 3.2 shows a schematic of the coil system together with a sample cell.

The holding coils were powered by a Kepco power supply, which varied the field strength according to waveforms provided by a HP 3325B function generator. The function generator accepted from the PC the waveforms, as well as commands to start and stop feeding the waveform into the power supply. For our AFP tests, we used a triangle waveform, so that the holding field was swept at a constant rate, from a static

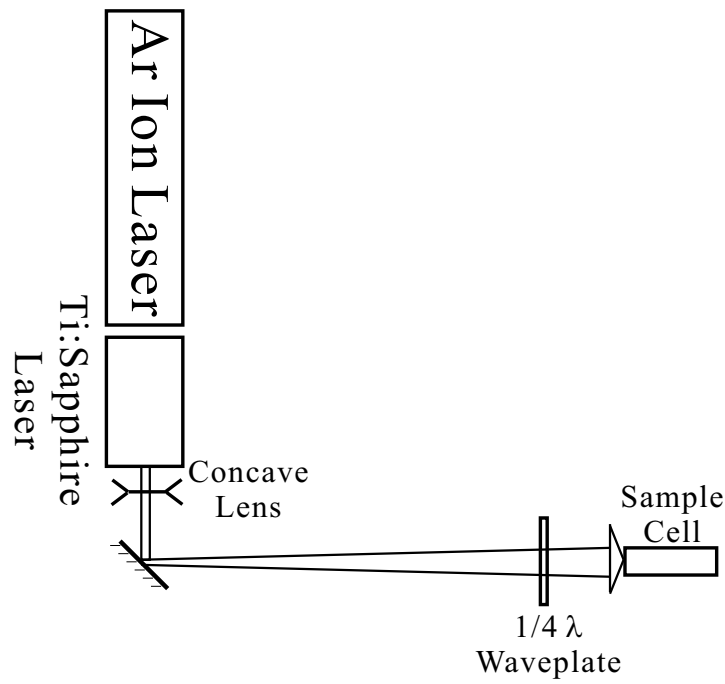


Figure 3.1: Schematic showing the optical setup for measurements concerning K and Cs, using the Ti:Sapphire laser. Optical elements are not drawn to scale.

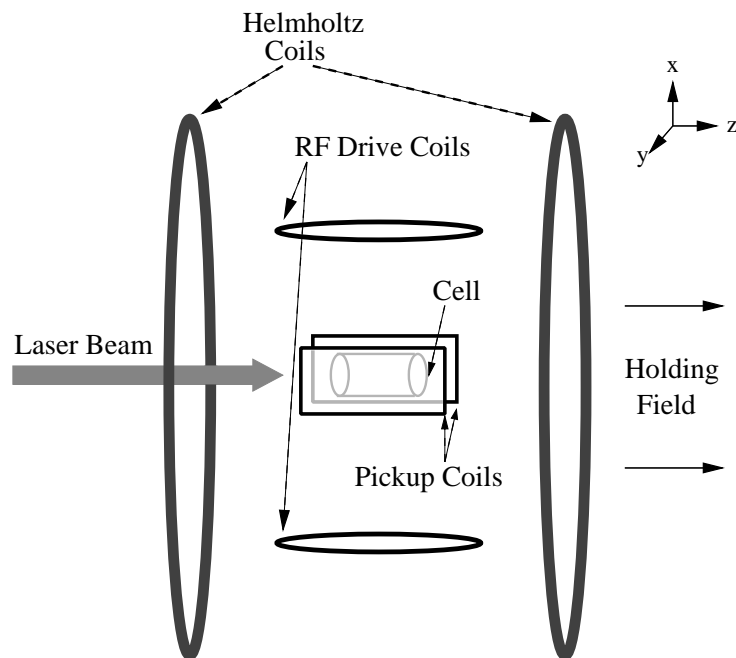


Figure 3.2: The coil system for performing AFP measurements. The components are not drawn to scale.

value up to a maximum value, and then back down, at the same rate, to the initial value. The entire sweeping cycle took 9 seconds, and the range of the sweeping was about 10 Volts in the output of the Kepco power supply, corresponding to a 11 Gauss range for the strength of  $B_0$ . The initial field strength can be adjusted between 10 Gauss and 25 Gauss, to change the time interval between the two AFP resonances in the signal. The purpose for changing the time interval will become evident in Sec. 3.2. The inhomogeneities in the holding field contribute to the relaxation rate of the nuclear polarization of  $^{129}\text{Xe}$ , therefore they were minimized. We have measured the inherent field inhomogeneities for the holding coils in a volume of about  $10 \times 10 \times 10 \text{ cm}^3$  at the center of the coils, where cells are tested. At a static field strength of 20 Gauss, the inhomogeneities are around 10 mG/cm.

The frequency of the rotating field was set at 27.6 kHz by a HP function generator. The output of the function generator was amplified by a RF amplifier manufactured by Electronic Navigation Industries (ENI, model number 21002), and the amplified signal powered the RF drive coils. The magnitude of  $\vec{B}_1$  was difficult to measure directly, since  $\vec{B}_1$  was rotating at radio frequency. But following the discussions in Sec. 3.2, we calculated  $|\vec{B}_1| \sim 80 \text{ mG}$ .

The outputs from the two pickup coils were added and amplified by going through a pre-amplifier. The pickup coils were in a perpendicular direction with respect to the RF drive coils, so theoretically the RF field should not induce voltages in the pickup coils. But, in reality, perfect perpendicular alignment is not possible, and there will always be some “leakage” signals induced by the RF field. The signal from the pickup coils were actually the sum of a sine wave with constant magnitude (the “leakage signal”) and the resonance signal. To isolate the resonance signal, the output of the pre-amplifier was fed into a Stanford Research System (SRS) lock-in amplifier, which compared the experimental signal to a reference sine signal (generated by a HP function generator) at the AFP resonance frequency, and output their difference. To make sure that the reference signal exactly cancelled the leakage signal in the pickup coils, an oscilloscope was used to monitor the signals from the pre-amplifier and from the function generator. The two signals were displayed on the same screen.

The magnitude and phase of the reference signal were then adjusted so that the two waveforms coincided. The peak-peak voltages ( $V_{pp}$ ) of the extracted signal were viewed as a vector with respect to the reference signal (synchronization signals from a HP function generator were used), and projected onto the  $x$  and  $y$  axes in a vector space. The outputs of the lock-in amplifier were digitized signals of these projections, the two output channels corresponding to the  $x$  and  $y$  projections. By adjusting the projection phase of the lock-in amplifier, we were able to change the distributions of the signal and the noise between the two channels. We maximized the signal-to-noise ratio of one of the two channels of the amplifier, and used that channel for our measurements. A PC with Labview software was used to record the outputs of the lock-in amplifier as text files, as well as to control the overall process of data acquisition.

The schematic of the electronics setup of the experiment is shown in Fig. 3.3. The two channels of the output of the lock-in amplifier are marked as “X” and “Y.”

In addition to the optical and electronic systems needed for the spin-exchange optical pumping and the AFP measurements, we also used a heating system to maintain the cell temperature, so that sufficient vapor densities of the tested alkali metal were present in the cell for the SEOP process. Any inhomogeneities in the magnetic field would cause increased relaxation rate of the  $^{129}\text{Xe}$  nuclear spin, so electronic currents and ferromagnetic objects needed to be kept away from the center of the holding coils, where the cells were tested. We used hot air flow to heat the cell, and constructed a Teflon oven for the purpose, approximately 20 cm by 10 cm by 10 cm. The oven has two optical windows on the two far ends to allow the laser beam through, an air inlet, and a small hole on the bottom plate. The purpose of the small hole was to allow a wire attached to the resistance temperature detector (RTD) to conduct the temperature signals to outside the cell. The air inlet was connected by a brass connector to brass tubings carrying hot air. The air flow was heated by an electric heater placed about 1.5 m away from the cell. A variable AC transformer (Variac) controlled the temperature of the heater, and ultimately the cell temperature. The RTD was non-magnetic, manufactured by Omega Engineering (Model F3105). The

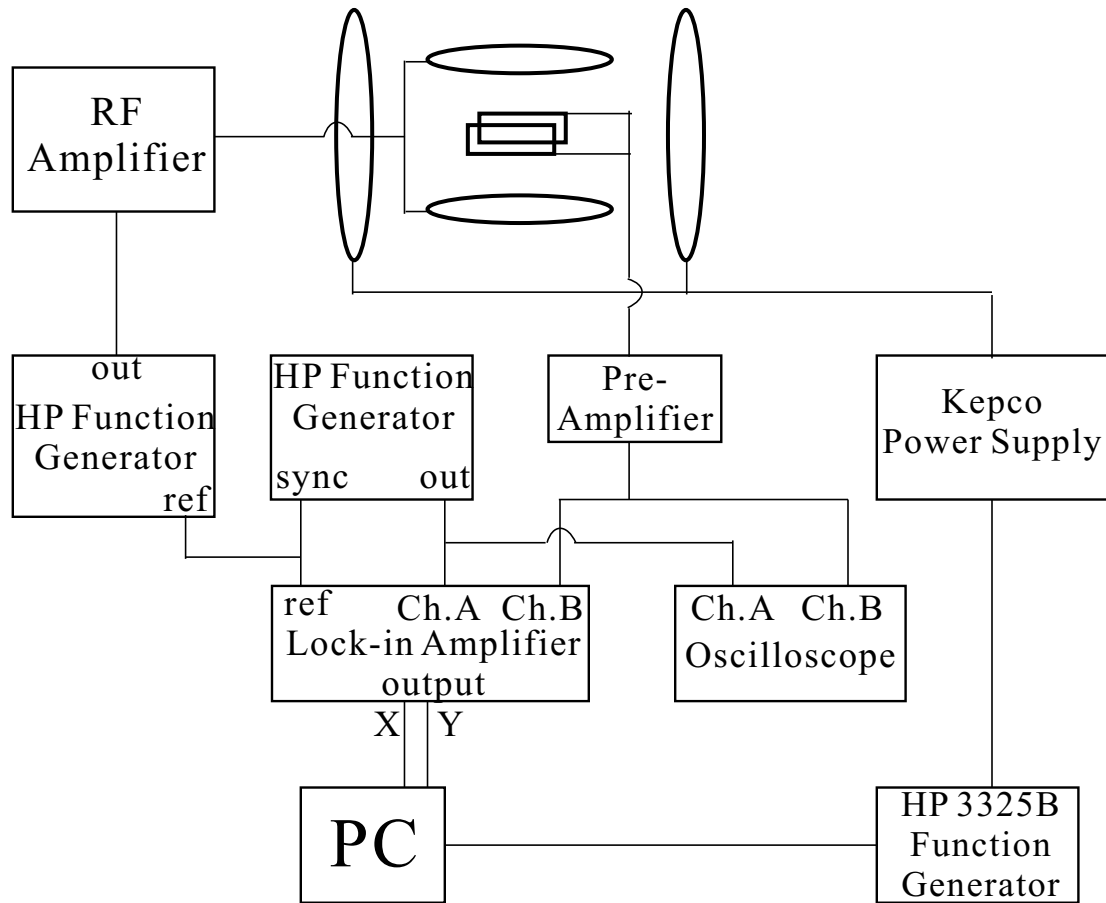


Figure 3.3: A schematic of the electronics setup for the measurements. The coils are the same with those in Fig. 3.2, and are not labeled in this figure.

RTD was attached to the tested cell, but out of the way of the laser beam during the measurements. The cell temperature was in the range of 90°C to 170°C. For K, Rb, and Cs, the individual temperature ranges were 130-170°C, 110-150°C, and 90-130°C, respectively. For each temperature point, the cell temperature was stabilized to be within  $\pm 0.4^\circ\text{C}$ . The temperature variations along the outer wall of the cell were measured to be smaller than  $\pm 1.0^\circ\text{C}$  during the cell tests.

## 3.2 Measurements of Spin-Exchange Rates between $^{129}\text{Xe}$ and Alkalis

With the setup introduced in Sec. 3.1, AFP tests were performed for polarized  $^{129}\text{Xe}$  nuclei. The AFP conditions Eqs. (2.42) and (2.43) require  $1/T_1 \ll (\frac{dB_0}{dt}/B_1) \ll \gamma B_0$ . For our case,  $B_1 \approx 80$  mG,  $\frac{d}{dt}B_0 \approx 2.4$  Gauss/sec, and  $\omega_0 = 27.6$  kHz. From our measurements,  $T_1 \gtrsim 20$  seconds. However, there is a complication with the value of the  $T_1$  during the AFP. Because, the  $T_1 \gtrsim 20$  sec results were the rate of relaxation between two AFP processes (see the later discussions in this section), whereas *during* the AFP, the relaxation mechanism related with the inhomogeneities in the magnetic field can be greatly increased. The denominator in Eq. (2.14),  $B_0^2$ , becomes  $B_{eff}^2$  during the AFP, and when  $B_{eff}$  is perpendicular with  $B_0$ , the quantity  $B_{eff}^2$  takes its minimum value  $B_1^2$ . Therefore, the maximum value of the relaxation rate of the nuclear polarization during the AFP was

$$(1/T_1)|_{AFP} = (1/T_1)|_{\overline{AFP}} + D \frac{|\nabla B|^2}{B_1^2}, \quad (3.1)$$

where  $(1/T_1)|_{\overline{AFP}}$  denotes the relaxation rate when the magnetization is not experiencing an AFP. Taking  $D \sim 0.1$  cm<sup>2</sup>/sec, the term  $D \frac{|\nabla B|^2}{B_1^2}$  was calculated to be about  $0.0015$  sec<sup>-1</sup>, still much smaller than  $(1/T_1)|_{\overline{AFP}} \approx 0.05$  sec<sup>-1</sup>.

Following the above discussions, the AFP conditions became  $0.05$  sec<sup>-1</sup>  $\ll$   $30$  sec<sup>-1</sup>  $\ll$   $2.76 \times 10^4$  sec<sup>-1</sup>, and were strictly satisfied.

After the temperature was stabilized, approximately 10 minutes of optical pumping was performed for the  $^{129}\text{Xe}$  nuclear polarization to build up and stabilize, before

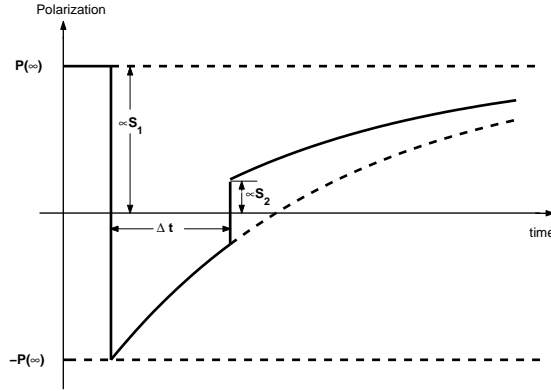


Figure 3.4: Time evolution of the  $^{129}\text{Xe}$  nuclear polarization during the AFP process. AFP signals  $S_1$  and  $S_2$  were produced at the points where the polarization was reversed, with the signal sizes proportional to the polarizations at the resonance times. Except for the resonance points,  $P_{\text{Xe}}$  underwent relaxation toward the equilibrium value  $P(\infty)$  with the rate  $\gamma_{SE} + \Gamma_{\text{Xe}}$ . The ratio  $S_2/S_1$  was determined by  $\Delta t$ , the interval between two resonances, and by  $\gamma_{SE} + \Gamma_{\text{Xe}}$ . A small loss of polarization induced by AFP is not explicitly shown in the picture. The laser was on continuously with  $\sigma^+$  helicity throughout the process.

AFP signals were taken. Two consecutive AFP signals were separated by an interval of at least 4 minutes, which was 3-10 times the relaxation time of the  $^{129}\text{Xe}$  polarization. So all the AFP signals were taken when the  $^{129}\text{Xe}$  polarization reached equilibrium between the spin-exchange optical pumping process and the relaxation mechanisms.

During the acquisition of each AFP signal, the holding magnetic field  $B_0\hat{z}$  was swept up past the resonance point  $B_0 = \omega_{B_1}/\gamma$ , and then back to the initial strength, passing the resonance point again. Two resonance signals were generated and recorded during each AFP process. Before the first resonance, the  $^{129}\text{Xe}$  nuclear polarization  $P_{\text{Xe}}$  was at its equilibrium value, denoted by  $P_{\text{Xe}}(\infty)$ . After the first resonance, the direction of the  $P_{\text{Xe}}$  was reversed,  $P_{\text{Xe}} = -P_{\text{Xe}}(\infty)$ , while the polarization of the alkali metal, and thus the equilibrium value of  $P_{\text{Xe}}$ , remained unchanged. Being away from its equilibrium value, the  $^{129}\text{Xe}$  polarization  $P_{\text{Xe}}$  underwent a longitudinal relaxation between the two resonances. The time-evolution of  $P_{\text{Xe}}$  during our AFP process is shown schematically in Fig. 3.4.

As we have discussed in Sec. 2.3, the AFP signals had shapes similar to Lorentzian in the form of Eq. (2.45), and the heights of the peaks were proportional to the  $^{129}\text{Xe}$  nuclear polarization. Therefore, the relative ratio of the height of the second signal peak to that of the first peak revealed the relaxation that the nuclear polarization underwent during the interval between the two resonances. If the time at the first resonance point is denoted by  $t = 0$ , then the time evolution of the  $^{129}\text{Xe}$  nuclear polarization  $P_{\text{Xe}}$  induced by the relaxation is

$$\begin{aligned} P_{\text{Xe}}(t) &= -P_{\text{Xe}}(\infty) + [P_{\text{Xe}}(\infty) - (-P_{\text{Xe}}(\infty))](1 - \exp[-(\gamma_{SE} + \Gamma_{\text{Xe}})t]) \\ &= P_{\text{Xe}}(\infty) \times (1 - 2 \exp[-(\gamma_{SE} + \Gamma_{\text{Xe}})t]) \end{aligned} \quad (3.2)$$

If we denote the time interval between the two resonances by  $\Delta t$ , the ratio of the values of  $P_{\text{Xe}}$  at the two resonance points becomes

$$P_{\text{Xe},2\text{nd resonance}}/P_{\text{Xe},1\text{st resonance}} = 1 - 2 \exp[-(\gamma_{SE} + \Gamma_{\text{Xe}})\Delta t]. \quad (3.3)$$

The sign of the AFP signal is determined by the direction of  $^{129}\text{Xe}$  nuclear polarization  $P_{\text{Xe}}$  with respect to direction of the effective magnetic field  $B_{eff}$  (defined by Eq. (2.41)) immediately before the resonance point. If  $P_{\text{Xe}}$  is in the same direction as  $B_{eff}$ , the AFP signal becomes positive, and the signal peak is ‘‘upward.’’ If  $P_{\text{Xe}}$  is on the opposite direction with  $B_{eff}$ , the AFP signal is negative, with a downward peak.  $B_{eff}$  was on the  $-z$  direction before the first resonance, and on the  $+z$  direction before the second one, so the AFP signal peak sizes  $S_1$  and  $S_2$  (as defined in Fig. 3.4) had the ratio of

$$S_2/S_1 = -P_{\text{Xe},2\text{nd resonance}}/P_{\text{Xe},1\text{st resonance}} = -1 + 2 \exp[-(\gamma_{SE} + \Gamma_{\text{Xe}})\Delta t]. \quad (3.4)$$

The interval  $\Delta t$  can be varied by changing the initial strength of the holding field, while keeping the sweeping range and sweeping rate of the field unchanged. By recording the ratios of the peaks as a function of  $\Delta t$ , we can readily calculate  $\gamma_{SE} + \Gamma_{\text{Xe}}$ , the relaxation rate of the  $^{129}\text{Xe}$  nuclear polarization. Fig. 3.5 shows a typical AFP signal with two peaks of different heights resulting from the relaxation.

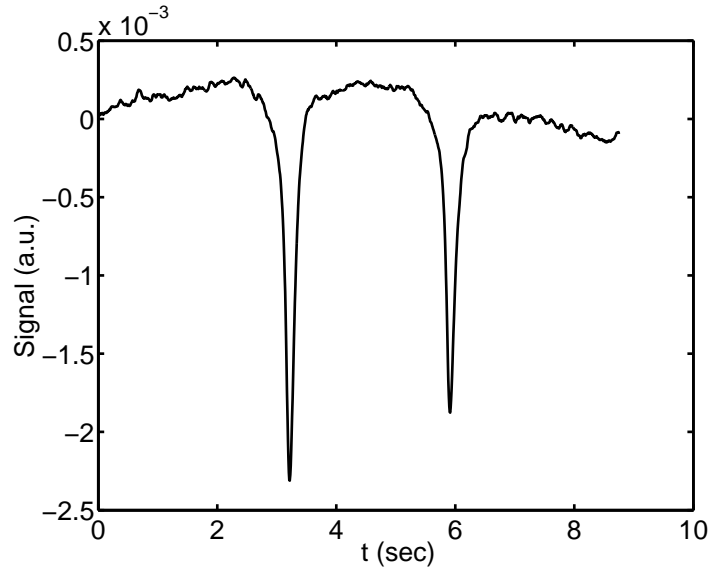


Figure 3.5: A typical  $^{129}\text{Xe}$  AFP signal in our tests. The second signal peak had a smaller size than the first one due to the relaxation of  $P_{\text{Xe}}$  between the two resonances. The signal size is in arbitrary units, and roughly corresponds to a 1%  $^{129}\text{Xe}$  polarization at equilibrium.

The above approach of measuring  $\gamma_{SE} + \Gamma_{\text{Xe}}$  involves only the relative ratio of the two signal sizes, so any drift of the laser power over timescales larger than  $\sim 10$  seconds cancels out. An accurate calibration of the absolute polarization value was also unnecessary. The flips of nuclear polarization at the resonance points, however, did introduce a small loss of  $P_{\text{Xe}}$ . This loss, denoted by  $\delta$ , was typically  $< 5\%$  of the original value. Considering this loss, Eq. (3.4) should now be modified to

$$\begin{aligned} S_2/S_1 &= - \left( - (1 - \delta) + [1 + (1 - \delta)](1 - \exp[-(\gamma_{SE} + \Gamma_{\text{Xe}})\Delta t]) \right) \\ &= -1 + (2 - \delta) \exp[-(\gamma_{SE} + \Gamma_{\text{Xe}})\Delta t]. \end{aligned} \quad (3.5)$$

The AFP signal data were recorded, and for each data, the vicinities of each of the two peaks were extracted and fitted using Matlab. The regions used for the fits centered on the peaks, and usually contained 200-300 discrete points. The data sampling frequency of the lock-in amplifier was chosen to be 128 Hz, so each point in the recorded text file corresponded to 1/128 second, and the fitted regions corresponded to time periods of about 1.5-2.5 sec. The fitting model has the form of the

Lorentzian-like shape as in Eq. (2.45):

$$S(t) = C + k \cdot t + \frac{Hw}{\sqrt{(t - t_0)^2 + w^2}}, \quad (3.6)$$

where  $t_0$  is the center of the peak, i.e., the resonance time,  $H$  is the peak height of the signal at the resonance, and  $w$  is the width of the peak. From Eq. (2.45) we know that  $w = B_1/(dB_0/dt)$ . Combining the fit values of  $w$ , and the known quantity  $dB_0/dt$ , we calculated  $B_1 \approx 80$  mG. The terms  $C$  and  $k \cdot t$  represent a constant baseline and a linear drifting. They were added in the fitting model to account for backgrounds under the signal. The time interval  $\Delta t$  between two resonances was the spacing between the centers of the two peaks. The value of  $\Delta t$  ranged from 1 to 9 seconds for our tests.

For each sample cell and each temperature point, we fixed the cell temperature monitored by the RTD to be within  $\pm 0.4^\circ\text{C}$ , and recorded AFP signals with different  $\Delta t$  values to form a data set. Theoretically, the value of  $P_{\text{Xe}}$  should be the same ( $P_{\text{Xe}} = P_{\text{Xe}}(\infty)$ ) before every AFP process, and the size of the first resonance peak  $S_1$  should remain a constant throughout any data set. However, due to slow and small shifts in the laser power and the cell temperature,  $S_1$  did exhibit some fluctuations among the AFP signals in each set. For a typical data set, the  $S_1$  fluctuations were within  $\sim \pm 7\%$ . Most of the uncertainties resulting from the fluctuations had been cancelled out in the ratio  $S_2/S_1$ , and will not be transferred to the results for  $\gamma_{SE} + \Gamma_{\text{Xe}}$ .

For each data set, a linear fit of  $\ln \frac{1+S_2/S_1}{2}$  with respect to  $\Delta t$  was performed. Following Eq. (3.5), the fitted slope gave  $\gamma_{SE} + \Gamma_{\text{Xe}}$ , and the intercept gave  $\ln(1 - \frac{\delta}{2})$ . The fit for a particular set of data is plotted in Fig. 3.6, where the fit value of  $\gamma_{SE} + \Gamma_{\text{Xe}}$  was  $0.0413 \text{ sec}^{-1}$ , and the fitted intercept of  $-0.012$  corresponded to the AFP loss of  $\sim 2.5\%$ . The inset shows a histogram of the relative deviations from the linear fit of the 44 AFP data points for that data set. The deviations corresponded to a  $\sim 3\%$  relative spread.

The above procedure describes the measurement of the  $^{129}\text{Xe}$  nuclear polarization relaxation rate  $\gamma_{SE} + \Gamma_{\text{Xe}}$  for a cell at a particular temperature. For each cell,  $\gamma_{SE} + \Gamma_{\text{Xe}}$  was measured at several different temperatures. There was always enough alkali

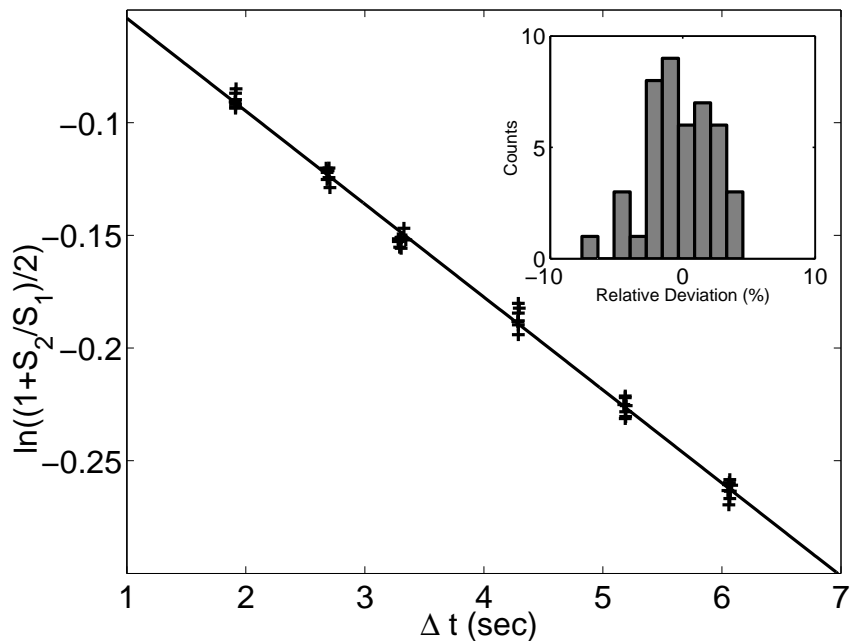


Figure 3.6: A linear fit of  $\ln \frac{1+S_2/S_1}{2}$  with respect to  $\Delta t$  for a particular data set. A Rb- $^{129}\text{Xe}$  cell was used as the sample cell, containing 0.124 amagat  $\text{N}_2$  and 0.248 amagat Xe (natural abundance). The quantity  $\gamma_{SE} + \Gamma_{\text{Xe}}$  was found to be  $0.0413 \text{ sec}^{-1}$ , while the fitting intercept  $-0.012$  corresponded to the AFP loss of  $\sim 2.5\%$ . A histogram showing the relative deviations of the data points with respect to the fitted line, is plotted as an inset.

metal in our sample cells, so that the alkali vapor was saturated. Therefore, different temperatures corresponded to different values of the alkali number density for the saturated vapor. These number densities were calculated from the temperatures measured by the RTD, using empirical vapor pressure formulae for the three alkalis.

In the past, many researchers had used the empirical formulae in the literature, such as the Killian formulae [42], Smithells formulae [43], formulae from *Handbook of Chemistry and Physics* [44], and formulae from *Vapor Pressure of the Elements* [45], to calculate alkali densities from measured cell temperatures. Unfortunately the published values do not agree well, and have differences up to factor of three for some cases. As an example, for the K vapor density, the *Handbook of Chemistry and Physics* value and the Smithells value roughly agree, but the Killian value differs with

them by a factor of 3. For the Rb density, the *Handbook of Chemistry and Physics* value agrees with the Killian value, yet the Smithells value differs by a factor of 1.5~2. Worse still, as we have mentioned in Ch. 1, some groups have recently reported that they have observed, in direct measurements, some cell-to-cell differences in the alkali vapor densities at identical temperatures [21, 22]. This could rule out any possibility of determining the alkali densities by only measuring the cell temperature. These research groups have therefore switched to direct measurements of the alkali densities, using the Faraday rotation method and the absorption spectroscopy method.

For our research, we used the Faraday rotation method [23] to study the alkali densities in our cells. From these measurements, the alkali density values were, indeed, different from values calculated using the formulae in the literature (specifically, we compared with the Killian formulae for Rb and K [42], and the formula from *Vapor Pressure of the Elements* for Cs [45]). The discrepancy between our measured values and the formulae was largest for the case of K, where the difference was a factor of three. However, we didn't observe the cell-to-cell difference. We concluded that since the vapor pressure of alkali metals could be vastly changed by the contaminants in the metals, their actual values might be quite different from the empirical values in the literature. But, since all our cells were made in a similar manner (details about cell preparation will be discussed in Sec. 4.1), using alkali metals with same specifications from the Alfa Aesar company, cell-to-cell variations in the vapor density-temperature relations were not significant among our cells. So, it is still possible for us to fit empirical vapor density formulae from measurements, and use these formulae to calculate the alkali density in our cells. Using the Faraday rotation measurements, we modified the existing formulae by adding scaling factors to fit our experimental results. Since our results were derived using our own empirical formulae, they were free from the possible errors related to using the various formulae in the literature.

More discussions about the measurements of the alkali vapor densities using the Faraday rotation method, and the complete results can be found in Sec. 3.3. For now, we will simply present the final forms of the fitted empirical formulae

$$[\text{K}] = 10^{10.34-4964/T} / kT, \quad (3.7)$$

$$[\text{Rb}] = 10^{9.25-4132/T} / kT, \quad (3.8)$$

$$[\text{Cs}] = 10^{12.89-4041/T} / T^{1.35} / kT, \quad (3.9)$$

where the unit of all number densities is  $\text{m}^{-3}$ , and the unit for temperature  $T$  is Kelvin. We estimate a relative error of 10% for all the formulae above, which comes primarily from the fits.

For each cell, using the alkali densities [alkali] calculated from our empirical formulae, we plotted the relaxation rates versus [alkali], and performed a linear fit to separate the slope  $\gamma_{SE}/[\text{alkali}]$  and the intercept  $\Gamma_{\text{Xe}}$ . The quantity  $\gamma_{SE}/[\text{alkali}]$  has a slight dependence on the temperature, since the collision term  $\langle v\sigma \rangle$  is proportional to  $\sqrt{T}$ . However, the experimental temperature spanned a range of less than  $40^\circ\text{C}$ , which corresponds to changes  $\lesssim 5\%$  in  $\langle v\sigma \rangle$ , whereas the alkali density changed drastically with temperature (usually a factor of 5-10), so the temperature dependence of  $\langle v\sigma \rangle$  was neglected during the fitting. For the final results of  $\langle v\sigma \rangle$  for all the three alkali metals, the average temperature for the measurements will be indicated for each alkali.

The possible temperature dependence of  $\Gamma_{\text{Xe}}$  appeared to be small, since no notable deviation was observed in the linear fits of  $\gamma_{SE} + \Gamma_{\text{Xe}}$  with respect to the alkali density. The curing process during the building of the cells (described in Sec. 4.1) ensured that the  $\Gamma_{\text{Xe}}$  values were stabilized and did not drift with time. Some representative data for a particular cell (Cs-Xe in this case) and the corresponding fit are shown in Table 3.1 and Fig. 3.7, respectively. From the fits, we found that the wall relaxation rate  $\Gamma_{\text{Xe}}$  for the cell is  $(0.0208 \pm 0.0020) \text{ sec}^{-1}$ , and the spin-exchange rate per Cs atom is  $\gamma_{SE}/[\text{Cs}] = (3.23 \pm 0.19) \times 10^{-21} \text{ sec}^{-1} \text{ m}^3$ . For this cell, the temperature range corresponded to a Cs density range of  $5 \times 10^{18} - 3 \times 10^{19} \text{ m}^{-3}$ .

Temperature ( $^{\circ}\text{C}$ )	[Cs] ( $10^{19}\text{m}^{-3}$ )	$\gamma_{SE} + \Gamma_{Xe}$ ( $\text{sec}^{-1}$ )
$123.7 \pm 0.4$	$2.92 \pm 0.29$	$0.1158 \pm 0.0049$
$110.7 \pm 0.4$	$1.42 \pm 0.14$	$0.0664 \pm 0.0037$
$101.9 \pm 0.4$	$0.853 \pm 0.085$	$0.0479 \pm 0.0022$
$89.9 \pm 0.4$	$0.405 \pm 0.040$	$0.0342 \pm 0.0017$

Table 3.1: Measured relaxation rates tabulated with respect to the cell temperature and calculated Cs number density, for a Cs-Xe cell with 0.093 amagat of  $\text{N}_2$  and 0.310 amagat of Xe. The uncertainties for  $\gamma_{SE} + \Gamma_{Xe}$  come from the fits. The 10% relative uncertainty associated with the number densities of Cs is mostly due to the uncertainties in our empirical density formula.

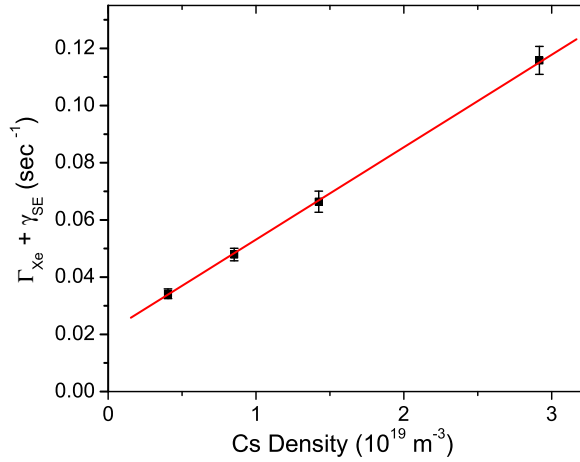


Figure 3.7: A linear fit of the measured relaxation rates versus Cs number density for a Cs-Xe cell with 0.093 amagat  $\text{N}_2$  and 0.310 amagat Xe. The fit gives  $\gamma_{SE}/[\text{Cs}] = (3.23 \pm 0.19) \times 10^{-21} \text{sec}^{-1}\text{m}^3$  and  $\Gamma_{Xe} = (0.0208 \pm 0.0020) \text{sec}^{-1}$  for the cell.

The analysis of the  $\gamma_{SE}/[\text{alkali}]$  data obtained using this method will be presented in Sec. 3.4, together with the final results for the spin-exchange rate constants  $\langle v\sigma_{\text{Xe-alkali}} \rangle$ ,  $\gamma_M$ , and  $b$ .

### 3.3 Direct Measurements of the Alkali Number Density Using the Faraday Rotation Method

In this section we will discuss a direct measurement of the alkali vapor densities using the Faraday rotation method. In the presence of an external magnetic field, an alkali metal vapor becomes a circularly birefringent medium. In other words, the vapor has different refractive indices for light with the circular polarization in the same direction as the magnetic field, and for light with the circular polarization in the opposite direction. Any linear polarization of the light can be decomposed into a superposition of the two circular polarizations with a fixed phase difference. So, when linearly polarized light passes through the alkali vapor, its two circular polarized components will gain an extra phase difference during the passage, and as a result, the linear polarization plane will be rotated. This rotation of the polarization plane is called “Faraday rotation.” We will see that for alkali vapors, Faraday rotation is relatively easy to detect when the vapor is optically thick, when the magnetic field is strong, and when the incident light has a wavelength near an absorption resonance of the alkali vapor.

The general form of the Faraday rotation angle is

$$\Delta\theta = \pi \frac{(n_- - n_+)l}{\lambda}, \quad (3.10)$$

where  $n_-$  and  $n_+$  are the refractive indices for the two circular polarizations of the incident light,  $l$  is the length of the circularly birefringent medium through which the light passes, and  $\lambda$  is the wavelength of the light. From the discussions in Wu *et al.* [23], in optically thick alkali vapor, for light with wavelength in the vicinities of the  $D1$  or  $D2$  resonances of the alkali, the Faraday rotation angle approximately takes

the form of

$$\Delta\theta \approx 2 \frac{\pi l}{\lambda_0} [\text{alkali}] r_e \lambda_0^5 f \frac{1}{4\pi c} \frac{K \mu_B B / h}{(\Delta\lambda)^2}, \quad (3.11)$$

where  $\lambda_0$  is the resonance wavelength,  $\Delta\lambda = \lambda - \lambda_0$  is the detuning between the wavelength of the incident light and the resonance wavelength,  $r_e$  is the classical electron radius,  $f$  is the oscillator strength of the resonance ( $f \approx \frac{1}{3}$  for  $D1$  lines,  $f \approx \frac{2}{3}$  for  $D2$  lines),  $c$  is the speed of light,  $\mu_B$  is the Bohr magneton, and  $h$  is Planck's constant. The quantity  $K$  is a constant related to the resonance transition, defined as

$$K = g_g \frac{2 + J_g(J_g + 1) - J_e(J_e + 1)}{4} + g_e \frac{2 + J_e(J_e + 1) - J_g(J_g + 1)}{4}, \quad (3.12)$$

where the subscript  $g$  stands for the ground state of the transition, and  $e$  stands for the excited state. The constants  $J$  refer to the total angular momenta,  $g$ 's are the Lande  $g$  factors, where

$$g = 1 + \frac{J(J + 1) + S(S + 1) - L(L + 1)}{2J(J + 1)}. \quad (3.13)$$

In our measurements, the incident light had wavelengths near the  $D1$  lines of the alkalis. The  $D1$  lines represent the resonance transitions between  $S_{1/2}$  and  $P_{1/2}$  states. Therefore,  $g_g = 2$ ,  $g_e = \frac{2}{3}$ ,  $J_g = J_e = \frac{1}{2}$ , and  $K$  is calculated to be  $\frac{4}{3}$ . We can plug these values into Eq. (3.11) to obtain the Faraday rotation angle,

$$\Delta\theta \approx l [\text{alkali}] r_e \lambda_0^4 \frac{2}{9c} \frac{\mu_B B}{h} \frac{1}{(\Delta\lambda)^2}. \quad (3.14)$$

There is a similar term in the rotation angle resulting from the  $D2$  resonance, but since  $\Delta\theta$  is inversely proportional to the square of the detuning  $\Delta\lambda$ , and all the wavelengths were within  $\pm 0.3$  nm of the  $D1$  lines, the  $D2$  term in the rotation angle tended to be much smaller than the  $D1$  term. Of the alkali metals that we measured, K has the smallest wavelength difference between  $D1$  and  $D2$  lines, which is 2.3 nm. The maximum relative correction pertaining to the  $D2$  term is less than 2.3% for K. The wavelength differences between the two resonance lines for Rb and Cs are much larger (14.7 nm and 42.2 nm, respectively), and the  $D2$  corrections are negligible for these two alkalis.

Compared with the absorption spectroscopy method, which is another approach often used to measure alkali vapor densities, the Faraday rotation method has the advantage of not requiring measurements at wavelengths very close to the resonance lines. Therefore, the Faraday rotation method is particularly convenient for high alkali densities. For example, Vliegen *et al.* have reported measurements of K density up to  $10^{22} \text{ m}^{-3}$  [46]. This method had been applied by many groups for measurements of alkali number densities [21, 23, 46].

Since the Faraday rotation measurements required varying the wavelength of the incident laser light, we used our Ar<sup>+</sup> pumped Ti:Sapphire laser for the measurements for all three alkalis. The laser power was attenuated to  $\sim 300$  mW. The beam is initially linearly polarized, and, therefore, no further manipulation of its polarization was necessary. The Faraday rotation measurements did not require the laser beam to cover the cell, so no lens was applied in the light path. The laser beam had a natural size of about  $3 \sim 5$  mm in diameter.

In addition to the laser, our optical setup for the Faraday rotation measurements included a photoelastic modulator (PEM) manufactured by Hinds Instruments, two polarizing cube beamsplitters (BS), a pinhole, and a photodiode (PD).

The optic setup is sketched in Fig. 3.8. In the sketch, as well as in the following discussions, we define the direction along the holding magnetic field and the propagation of the laser beam to be the  $z$ -direction. This is consistent with our previous definition. We define the other horizontal direction in the laboratory frame as the  $x$ -direction, and the vertical direction as the  $y$ -direction. The polarization vector of the initial laser beam was close to the horizontal direction, or the  $x$ -direction. The beam first went through a BS which allowed only light with horizontal linear polarization to be transmitted, providing a beam with polarization exactly in the  $x$ -direction. Next, the beam passed through the heated sample cell. The cell was a 1 inch by 3 inch cylinder, identical to the sample cells used in Sec. 3.1, with the cylindrical axis along the  $z$ -direction. The laser beam propagated through the full length of the cell, and its polarization plane was rotated by the Faraday rotation angle. A pinhole was placed after the cell to block stray lights reflected from the cell walls. For all measurements

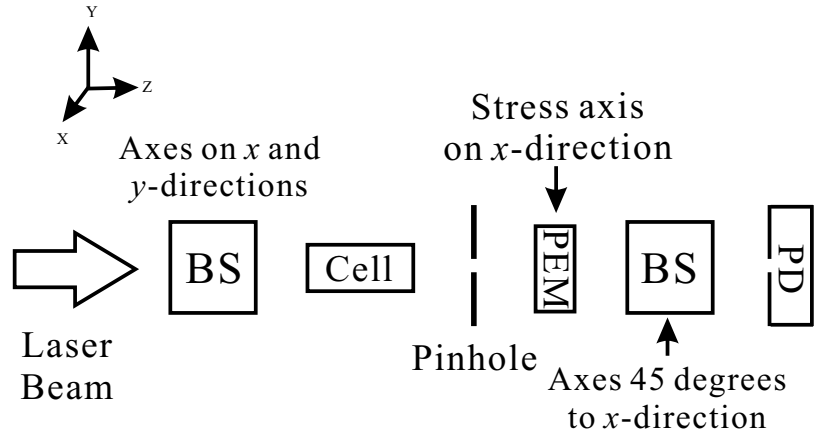


Figure 3.8: A schematical diagram of the optical experimental setup for the Faraday rotation measurements. The sample cell was heated in an oven with optical windows, the oven is not explicitly shown here.

at different alkali densities (thus different absorbances), the aperture of the pinhole was adjusted between 2 mm and 4 mm, to reach a compromise between reducing stray lights and maintaining a reasonable level of detectable photon flux. The beam then passed through the PEM with the stress axis in the  $x$ -direction, and another BS, whose axes were  $45^\circ$  with respect to the  $x$ -direction. The transmitted beam was finally detected using the PD.

The photodiode detected the light signals and transformed them into electric signals, which were input both to a HP oscilloscope and to a SRS Lock-in amplifier. The oscilloscope averaged the signal over a 16-second period to remove transient fluctuations, and recorded the size of the DC component of the signal. The lock-in amplifier received its reference signal from the PEM, with the frequency set at two times the modulating frequency of the PEM. The signal component at the same frequency formed the lock-in amplifier's output. The output was then sent to another input channel of the oscilloscope and averaged. The averages of the two components of the photodiode signal became the final data used to calculate the alkali densities.

Now we derive the formulae that describe the Faraday rotation measurement. The laser beam propagated along the direction of holding magnetic field, i.e., the  $z$ -direction, so the light's polarization vector can only be in the  $x$ - $y$  plane. After

passing through the sample cell, the electric field of the light is in the direction of  $(\cos(\Delta\theta)\hat{x} + \sin(\Delta\theta)\hat{y})$ . The pinhole does not change the polarization, so the electric field after the pinhole is in the form of

$$\vec{E} = E_0 e^{-i\omega t} (\cos(\Delta\theta)\hat{x} + \sin(\Delta\theta)\hat{y}), \quad (3.15)$$

where  $\omega$  is the frequency of the incident laser light. The PEM introduces a relative phase retardation between the linear polarization component on the PEM's stress axis, and the component on the perpendicular direction. We denote this phase retardation by  $\psi$ ,  $\psi$  varies with time, in the form of  $\psi(t) = \psi_0 \cos(\omega_{PEM}t)$ , where  $\psi_0$  is the maximum retardation, and  $\omega_{PEM}$  is the PEM frequency. After the PEM, the electric field of the laser becomes

$$\vec{E} = E_0 e^{-i\omega t} (\cos(\Delta\theta)\hat{x} + \sin(\Delta\theta)e^{-i\psi}\hat{y}). \quad (3.16)$$

The second BS projects the electric field onto a direction  $45^\circ$  with respect to  $x$ -axis. Denoting the projection direction to be the  $x'$ -direction, the projection becomes

$$\vec{E} = E_0 \frac{\sqrt{2}}{2} e^{-i\omega t} (\cos(\Delta\theta) + \sin(\Delta\theta)e^{-i\psi})\hat{x}'. \quad (3.17)$$

Finally, the photodiode measures the flux of transmitted light that passes through the PD aperture. The flux is the product of the intensity and the aperture area, and the output signals are proportional to the flux. The signal from the PD can be written as

$$S \propto I \propto |E|^2 = \frac{E_0^2}{2} \left| \cos(\Delta\theta) \frac{\sqrt{2}}{2} + \sin(\Delta\theta) \frac{\sqrt{2}}{2} \cos \psi + i \sin(\Delta\theta) \frac{\sqrt{2}}{2} \sin \psi \right|^2 \\ \propto 1 + \sin(2\Delta\theta) \cos \psi. \quad (3.18)$$

Substituting  $\psi$  by  $\psi_0 \cos(\omega_{PEM}t)$ , we can expand the  $\cos \psi$  term in the above result into Bessel functions of the first kind  $J_n(\psi_0)$ , keeping terms with frequencies up to  $2\omega_{PEM}$ ,

$$S \approx \text{constant} \times (1 + \sin(2\Delta\theta)J_0(\psi_0) - 2\sin(2\Delta\theta)J_2(\psi_0) \cos(2\omega_{PEM}t)). \quad (3.19)$$

By choosing the PEM's setting for  $\psi_0$  so that  $J_0(\psi_0) = 0$ , or  $\psi_0 = 2.406$  rad, we can construct the DC component of the signal independent of  $\Delta\theta$ . Now,  $J_2(2.406) = 0.432$ , so

$$\left| \frac{S_2}{S_0} \right| = 0.864 \sin(2\Delta\theta), \quad (3.20)$$

where  $S_2$  denotes the signal component with frequency  $2\omega_{PEM}$ , and  $S_0$  is the DC component of the signal. From the data we took, it was straightforward to calculate the Faraday rotation angle  $\Delta\theta$ .

In reality, the passage through the alkali vapor in the sample cell can induce a small circular polarization in the transmitted light. This small circular polarization, quantified by the mean photon spin  $s$ , would alter the  $S_2$  signal component by a factor of  $\sqrt{1-s^2}$ , and generate an extra signal component  $S_1$  at the  $\omega_{PEM}$  frequency, with a size of

$$S_1 = \text{constant} \times 2sJ_1(\psi_0), \quad (3.21)$$

where the constant is the same as the one in Eq. (3.19). During our measurements, we monitored the mean photon spin by recording the signal component  $S_1$  with the frequency of  $\omega_{PEM}$ , and found that for all our measurements,  $s = (S_1/S_0)/(2J_1(\psi_0)) \lesssim 3\%$ . The relative inaccuracy in  $|S_2/S_1|$  induced by  $s$  is  $1 - \sqrt{1-s^2} \approx s^2/2 \lesssim 0.05\%$ , and was negligible for our measurements.

Using the above signal from the photodiode, we can calculate  $\Delta\theta$ . For each detuning of the wavelength  $\Delta\lambda$ , we made measurements at two different values of the holding magnetic field (approximately  $\pm 40$  Gauss). The exact difference between them was 84.1 Gauss. From Eq. (3.14), the difference in the two  $\Delta\theta$  values can be found, it is related to the alkali density by

$$|\Delta\theta_2 - \Delta\theta_1| \approx l[\text{alkali}]r_e\lambda_0^4 \frac{2}{9c} \frac{\mu_B \Delta B}{h} \frac{1}{(\Delta\lambda)^2}, \quad (3.22)$$

where  $\Delta B = 84.1$  Gauss, and  $l = 7.5$  cm. As a result, the difference in the Faraday rotation angles was solely determined by the alkali density and the wavelength

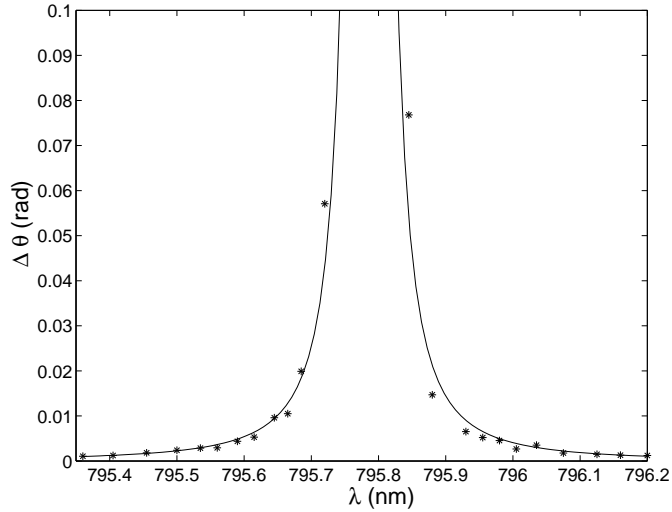


Figure 3.9: A typical fit of the difference in Faraday rotation angles with respect to the detuning of the incident light wavelength. The fit indicates a Rb density of  $2.53 \times 10^{19} \text{ m}^{-3}$ .

detuning  $\Delta\lambda$ ,

$$|\Delta\theta_2 - \Delta\theta_1| = \frac{C_F}{(\Delta\lambda)^2} [\text{alkali}], \quad (3.23)$$

$$\text{where } C_F \equiv \frac{2lr_e\lambda_0^4\mu_B\Delta B}{9hc}.$$

The constant  $C_F$  varies for different alkali metals.

The laser wavelength  $\lambda$  was tuned in the range of  $\pm 0.3$  nm of the  $D1$  resonance wavelength  $\lambda_0$  (i.e.,  $\Delta\lambda$  varied between  $-0.3$  and  $0.3$  nm). The corresponding  $|\Delta\theta_2 - \Delta\theta_1|$  values were recorded. An average data set contained about 20 data points of  $|\Delta\theta_2 - \Delta\theta_1|$  at different  $\Delta\lambda$  values. The data were subsequently fit to the form of Eq. (3.23) to calculate [alkali], the alkali number density. A typical fit of  $|\Delta\theta_2 - \Delta\theta_1|$  with respect to  $\Delta\theta$  is shown in Fig. 3.9. The fit is for a Rb cell, and corresponds to a Rb density of  $2.53 \times 10^{19} \text{ m}^{-3}$ .

For each alkali metal, we made measurements for two cells and at different temperatures. It is possible that some cell-to-cell variation in the alkali densities results from slight differences during the cleaning and filling processes of the cells. Therefore, we purposely chose cells made from different glass manifolds for the density mea-

measurements, so that the cell-to-cell variation, if existed, can be easily detected. The temperature measurement was performed using a RTD, in the same manner as for our relaxation rate measurements, which has been described in Sec. 3.1. Therefore, the possible systematic uncertainty in the temperature measurement would not be carried into the determination of alkali densities. For K, Rb, and Cs, we have plotted our results in Fig. 3.10, 3.11, and 3.12, respectively. Also in the plots are plotted some frequently used empirical formulae: Killian formulae for K and Rb [42], and the formula from *Vapor Pressure of the Elements* for Cs [45]. These empirical formulae are

$$[\text{K}] = 10^{10.83-4964/T}/(kT) \quad (3.24a)$$

$$[\text{Rb}] = 10^{9.55-4132/T}/(kT) \quad (3.24b)$$

$$[\text{Cs}] = 10^{13.1781-1.35 \log_{10} T-4041/T}/(kT), \quad (3.24c)$$

where the number densities are in  $\text{m}^{-3}$ ,  $k$  is Boltzmann's constant, and the temperature  $T$  is in Kelvin. From the plots we see that, although the experimental data differed significantly from the existing formulae, the experimental and empirical values have good correlations. That is, no significant cell-to-cell variation in the alkali vapor density-temperature relations was observed.

Concerning the alkali vapor density-temperature relations, we have a preliminary conjecture, that the relations can vastly change due to contaminants in the alkali metals and in the cell walls. This conjecture can explain the fact that cell-to-cell variations in the density-temperature relations were observed by other research group, yet were not present in our cells, since for all our sample cells, we used alkali metals with same specifications, and prepared the cells in the same manner. This can also explain the difference between our experimental values of the alkali densities and the empirical formulae in the literature, since the sample cells used for determining the empirical formulae were prepared in different manners.

Since the cell-to-cell variation in alkali density-temperature relations is not observed in our cells, empirical formulae can still be used to calculate alkali densities from the measured cell temperatures. It is usually assumed that the saturated vapor

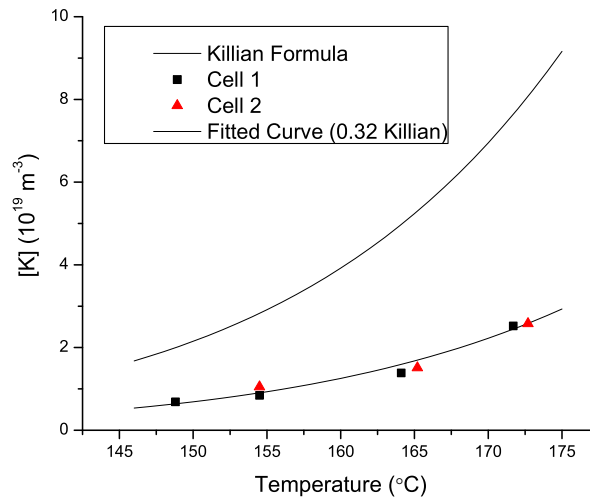


Figure 3.10: The K densities from our direct measurements, together with Killian's empirical density formula and the renormalized Killian formula we fitted using our data.

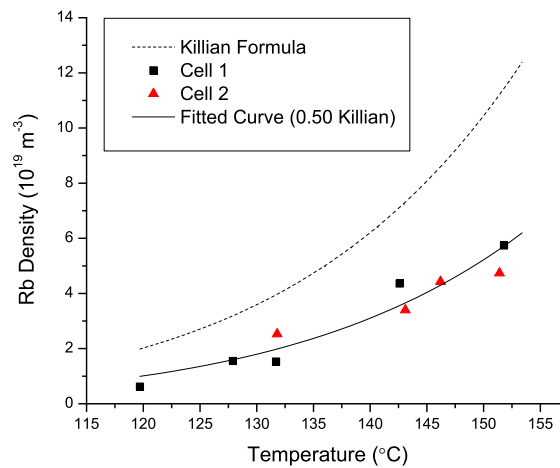


Figure 3.11: The Rb densities from our direct measurements, together with Killian's empirical density formula and the renormalized Killian formula we fitted using our data.

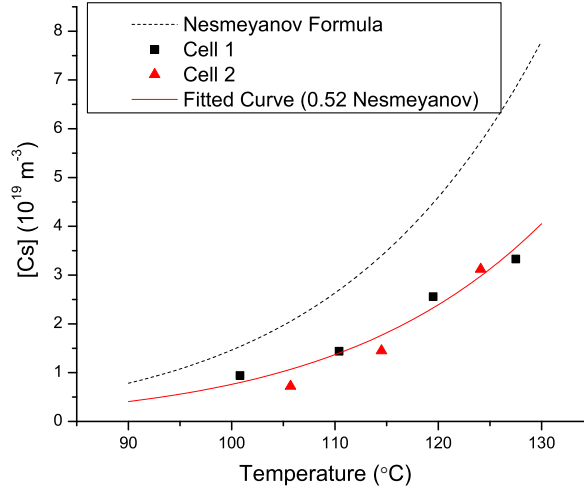


Figure 3.12: The Cs densities from our direct measurements, together with Nesmeyanov’s empirical density formula from *Vapor Pressure of the Elements* and the renormalized formula we fitted using our data.

densities for all alkali metals take the form of [44]

$$[\text{alkali}] = 10^{A-B/T-C \log_{10} T} / (kT), \quad (3.25)$$

where  $A$ ,  $B$ , and  $C$  are constants for a particular metal,  $[\text{alkali}]$  is in  $\text{m}^{-3}$ , and  $T$  is in Kelvin. We made a further assumption that the differences between our empirical formulae and the formulae in the literature (3.24) are only scaling factors, that is, only values of  $A$  differ. We fitted our data to estimate these factors. The fitted curves are also shown in Figs. 3.10-3.12. The scaling factors for K, Rb, and Cs number densities were found to be 0.32, 0.50, and 0.52, respectively.

With the scaling factors included, the final forms of the empirical formulae from our Faraday rotation measurements are

$$[\text{K}] = 10^{10.34-4964/T} / (kT) \quad (3.26a)$$

$$[\text{Rb}] = 10^{9.25-4132/T} / (kT) \quad (3.26b)$$

$$[\text{Cs}] = 10^{12.89-1.35 \log_{10} T - 4041/T} / (kT) \quad (3.26c)$$

where the unit for number densities is still  $\text{m}^{-3}$ . With these formulae we determined

the spin-exchange rate constants. Based on the fitted curves, we estimated a 10% relative uncertainty in our modified formulae of alkali saturated vapor densities as functions of the temperature.

### 3.4 Determination of the Spin-Exchange Rate Constants

Using the approach described above, for each alkali metal, we measured the values of  $\gamma_{SE}/[\text{alkali}]$  for different cells, each with a different combination of Xe and N<sub>2</sub> densities. As we discussed in Ch. 2, there are two spin-exchange mechanisms: the transfer of spin in binary collisions, which is independent of the densities of Xe and N<sub>2</sub> in the cell, and the transfer by forming van der Waals molecules, which is dependent on these densities. By fitting the measured  $\gamma_{SE}/[\text{alkali}]$  values with respect to [Xe] and [N<sub>2</sub>] in the form of Eq. (2.31), we extracted  $\langle v\sigma \rangle_{\text{Xe-alkali}}$ ,  $\gamma_M$ , and  $b$  for each alkali metal. As an example, for the Cs case, the results of  $\gamma_{SE}/[\text{Cs}]$  measured for 9 Cs-Xe cells are listed in Table 3.2. The data and fits are plotted in Fig. 3.13, with the ordinate being  $\gamma_{SE}/[\text{Cs}]$ , and the abscissa being the reciprocal of the effective number density of the cell. The effective number density of the cell is defined as  $[\text{Xe}] + b[\text{N}_2]$ , where  $b$  for the Cs-Xe case has the fit value of 0.97. The unit for number densities of Xe and N<sub>2</sub> has been changed from amagat to m<sup>-3</sup> so that  $\gamma_M$  has the dimension of sec<sup>-1</sup>.

Studies for K-<sup>129</sup>Xe and Rb-<sup>129</sup>Xe pairs were also performed, with 5 and 7 cells, respectively. Raw data were analyzed with the same method, with one minor difference. For Rb, we took the value of  $b$ , the constant for N<sub>2</sub> in the effective number density, from calculations by Cates *et al.* [20]. The results for the three alkali-<sup>129</sup>Xe pairs are listed in Table 3.3. As discussed above, the  $\langle v\sigma \rangle$  values have slight temperature dependencies, and the results listed in Table 3.3 for K, Rb, and Cs are for average temperatures of 150°C, 130°C, and 110°C, respectively.

As discussed in Sec. 3.3, the major systematic uncertainty comes from the deter-

[Xe] ( $10^{24} \text{ m}^{-3}$ )	[N <sub>2</sub> ] ( $10^{24} \text{ m}^{-3}$ )	$\gamma_{SE}/[\text{Cs}]$ ( $10^{-21} \text{ m}^3 \text{ sec}^{-1}$ )
12.5	3.33	$2.33 \pm 0.10 \pm 0.23$
5.83	3.33	$3.50 \pm 0.10 \pm 0.35$
3.31	3.33	$5.44 \pm 0.19 \pm 0.54$
8.33	10.0	$1.85 \pm 0.10 \pm 0.18$
8.33	5.00	$2.00 \pm 0.12 \pm 0.20$
8.33	2.50	$3.23 \pm 0.19 \pm 0.32$
4.17	3.33	$4.04 \pm 0.13 \pm 0.40$
4.17	5.00	$3.35 \pm 0.08 \pm 0.34$
4.17	7.50	$3.06 \pm 0.08 \pm 0.31$

Table 3.2: The quantity  $\gamma_{SE}/[\text{Cs}]$  measured for the 9 Cs-Xe cells, tabulated with the number densities of Xe and N<sub>2</sub> in the cells. Note that  $\text{m}^{-3}$  has been used as the unit for the number densities.

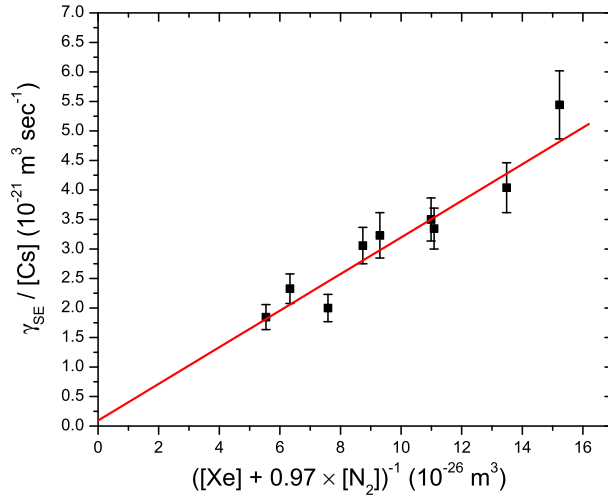


Figure 3.13: A plot of  $\gamma_{SE}/[\text{Cs}]$  versus the reciprocal of the effective number density in the cells. The effective number density is defined as  $[\text{Xe}] + b[\text{N}_2]$ , where  $b=0.97$  for the Cs-Xe case. From the fit, we have  $\gamma_{SE}/[\text{Cs}] = 9.4 \times 10^{-23} + (3.1 \pm 0.4) \times 10^4 ([\text{Xe}] + (0.97 \pm 0.11) [\text{N}_2])^{-1} (\text{m}^3 \text{sec}^{-1})$ , with the number densities in  $\text{m}^{-3}$ .

Alkali Metal	$\langle v\sigma \rangle$ ( $10^{-22}\text{m}^3\text{sec}^{-1}$ )	$\zeta$ (calculated)	$\gamma_M$ ( $10^5\text{sec}^{-1}$ )	$b$
K	0.63	0.125	$1.92 \pm 0.24 \pm 0.20$	$0.87 \pm 0.08$
Rb	10	0.095	$1.02 \pm 0.08 \pm 0.09$	0.275
Cs	0.94	0.0625	$4.92 \pm 0.63 \pm 0.49$	$0.97 \pm 0.11$

Table 3.3: Experimental results of  $\langle v\sigma \rangle$ ,  $\gamma_M$ , and  $b$  for the three alkali metals. The  $\zeta$  values were calculated from the relative abundances and nuclear spins of the alkali metals' isotopes. The first term in the uncertainties of the  $\gamma_M$  values comes from statistical scatterings of the data points, and the second term is the systematic uncertainty.

mination of alkali densities, which we estimated to be a  $\sim 10\%$  relative uncertainty. Other uncertainties (e.g., the knowledge of the pressures of the gases during fillings) did not exceed  $\sim 3\%$ . An overall  $10\%$  systematic uncertainty has been included in Table 3.3. The quantity  $b$ , however, is free from this systematic uncertainty, since the uncertainty would be absorbed into  $\gamma_M$ .

Since all of the test cells contain Xe and  $\text{N}_2$  number densities less than one amagat, the data points were not close enough to the high-density limit to give an accurate fit value for the intercept. The intercept corresponds to the binary collision term  $\langle v\sigma \rangle$ , so the results for  $\langle v\sigma \rangle$  are only crudely determined. The uncertainties on the  $\langle v\sigma \rangle$  values are large and have not been indicated in the table of results. The  $\gamma_M$  results have reasonable precisions, with uncertainties of  $\sim 15\%$ .

Compared with previous measurements of  $\langle v\sigma \rangle$  for the Rb- $^{129}\text{Xe}$  pair [20, 21], which find

$$\langle v\sigma \rangle = (3.70 \pm 0.15 \pm 0.55) \times 10^{-22} \text{ m}^3\text{sec}^{-1},$$

and

$$\langle v\sigma \rangle = (1.75 \pm 0.12) \times 10^{-22} \text{ m}^3\text{sec}^{-1},$$

respectively, our result  $1.0 \times 10^{-21}\text{m}^3\text{sec}^{-1}$  is different, in the latter case by a factor of 5. The uncertainties of our values of  $\langle v\sigma \rangle$  are also large. Our  $\gamma_M$  value for Rb-Xe pair  $(10.2 \pm 0.8 \pm 0.9) \times 10^4 \text{ sec}^{-1}$  is about 3 times as large as the result from measurements

by Cates *et al.* [20], which is

$$\gamma_M = (2.92 \pm 0.18 \pm 0.41) \times 10^4 \text{ sec}^{-1}.$$

However, in Ref. [20], the Killian empirical formula was used to calculate the Rb density, while we used direct Rb density measurements. Our Faraday rotation measurements suggest that, at least for our cells, the Killian formula for Rb vapor densities tends to give results higher than the actual values, and data analysis based on the Killian formula might underestimate the relaxation rates.

The  $\gamma_M$  values for K and Cs have not been previously measured at high Xe density (i.e.,  $\sim 1$  amagat), so we do not have similar results with which to compare.

Presently the majority of applications [16, 17, 18, 47] using  $^{129}\text{Xe}$  polarization through spin-exchange collisions with alkali metals have been performed with total number densities of Xe and  $\text{N}_2 \lesssim 1$  amagat, similar to our conditions. For such cell densities, it is the van der Waals mechanism that dominates the spin-exchange process, and our precise determinations of  $\gamma_M$ 's are helpful information for these cases. Nonetheless, it is desirable to complement our studies with tests in the high-density limit as has been done for Rb- $^{129}\text{Xe}$  by Jau *et al.* [21]. Such measurements can provide accurate determinations of  $\langle v\sigma \rangle$  by suppressing the contribution from vdW molecules.

Since different alkali metals have different values for  $\zeta$  and  $b$ , their  $\gamma_M$ 's can not be directly compared to find which alkalis are better for polarizing  $^{129}\text{Xe}$  through the SEOP process. But comparisons might be done by calculating the spin-exchange rates for different alkalis under typical conditions, so that we can gain insight into the choice of the most promising alkali for polarizing  $^{129}\text{Xe}$ . An example of such comparisons is shown in Table 3.4, in which the number densities for Xe and  $\text{N}_2$  were taken to be 0.35 amagat and 0.15 amagat, respectively. The number density for the alkali metal was set at  $2.5 \times 10^{19}$  atoms/m<sup>3</sup>, which corresponded to different temperatures for different alkalis, as shown in Table 3.4. Naturally, laser availability, pumping efficiency, temperature and other issues need to be considered for optimizing the  $^{129}\text{Xe}$  polarization for different applications.

Alkali Metal	Spin-Exchange Rate (sec <sup>-1</sup> )	Corresponding Temperature (°C)
K	0.031	164
Rb	0.048	136
Cs	0.062	122

Table 3.4: Comparison of spin-exchange rates between <sup>129</sup>Xe and the three alkali metals K, Rb, and Cs, under a typical condition. This condition has [Xe]=0.35 amagat and [N<sub>2</sub>]=0.15 amagat, [alkali] was set at  $2.5 \times 10^{19}$  atoms/m<sup>3</sup>, the corresponding temperatures for different alkalis (calculated from our empirical alkali density formulae) were listed in the table.

In summary, we had made measurements for the spin-exchange rates between alkali-<sup>129</sup>Xe pairs for three alkali metals K, Rb, and Cs, with cell densities in the range of 0.2 to 0.7 amagat. The two terms in the spin-exchange rate, the binary collision term and the van der Waals molecule term, are separated by studying the cell density dependence of the spin-exchange rates. The constants that govern the spin-exchange process,  $\gamma_M$ ,  $\langle v\sigma \rangle$ , and  $b$  are determined. These results, especially the value of  $\gamma_M$ , provide useful information for estimating the spin-exchange rates of the three alkali-<sup>129</sup>Xe pairs under typical polarizing conditions, and ultimately for achieving optimal nuclear polarizations for <sup>129</sup>Xe.

## Chapter 4

# Experiments II: Imaging Study

In this chapter, we present a research project in which magnetic resonance imaging (MRI) of polarized  $^{129}\text{Xe}$  was performed. The purpose of the project is to demonstrate the possibilities of utilizing  $^{129}\text{Xe}$  polarized by the SEOP approach, as an imaging agent for MRI. Specifically, in collaboration with a Stanford research group, we constructed a low readout magnetic field imaging system, which is capable of produce MRI images using both water and laser-polarized  $^{129}\text{Xe}$  as the imaging agent. Ours was the first successful effort to perform both types of imaging in the same system, with low magnetic field and room temperature. The main task of our group (Hughes group at Caltech) was to produce sample cells containing  $^{129}\text{Xe}$ , and to build a polarizing system, which uses the SEOP method to polarize the nuclear spin of  $^{129}\text{Xe}$  in the cell, inducing a polarization high enough for the imaging. Throughout this project, we used the alkali metal Rb to polarize  $^{129}\text{Xe}$ .

To produce the sample cells, we needed a vacuum system to remove the air in the cells, before filling with the alkali Rb and the gases Xe and  $\text{N}_2$ . In Sec. 4.1, we will discuss in detail the procedures of cell building, including the cell designs, the preparation procedures of the glass cells before filling, a description of the vacuum system, and the production of the sample cells containing Rb and the gases.

When the sample cells were ready, we tried to determine the maximum nuclear polarization of  $^{129}\text{Xe}$  in the cells achieved by SEOP, to ensure that the imaging signal-to-noise ratio would be good. The polarization measurement (“polarimetry”) was performed by generating adiabatic fast passage (AFP) signals of the  $^{129}\text{Xe}$  magne-

tization, and calibrating the signals using water AFP signals. More about these measurements will be presented in Sec. 4.2.

The sample cells with the highest  $^{129}\text{Xe}$  polarizations were used for the MRI imaging. They were polarized, and imaged in our low field imaging system. The imaging system and the experimental designs for imaging the cells will be introduced in Sec. 4.3, and the imaging results will be presented in Sec. 4.4.

## 4.1 Sample Cell Construction

The sample cells used for the imaging study were glass cells made of Pyrex. The cells were filled with Xe (natural isotopic abundance) and  $\text{N}_2$ , and they also contained milligrams of Rb metal. The cells had spherical shapes, with the outer diameters being about 2.5 cm (1 inch). The sizes of the cells were chosen so that they could easily fit into the imaging magnet, yet be capable of producing signals with good signal-to-noise ratios. After accounting for the thickness of the glass wall, the inner diameters of the cells were estimated to be  $2.4 \pm 0.1$  cm.

We used Pyrex tubes as our raw material, and had them blown into glass manifolds by a professional glassblower. During the glassblowing process, the tubes were melted and expanded, resulting in cells with pristine glass surfaces having less adsorbed impurities. This helps to decrease the wall-induced relaxation of  $^{129}\text{Xe}$  nuclear polarization. The manifolds were designed so that each one could be used to produce five cells. On the end of each manifold, a glass capsule was attached containing Rb metal produced by the Alfa Aesar company. The purity of the Rb metal is 99.75%. The capsule was kept sealed during the glass blowing, and was broken only after the manifold had been pumped down to an appropriate level of vacuum. A sketch of the manifold is shown in Fig. 4.1. Only two raw cells are shown in the figure; the rest are not shown. To make it easier to pull off finished cells from the manifold, a narrow part was devised on each “stem” connecting a raw cell to the manifold. The completed cells were to be removed from these narrow parts.

The impurities in the cell can have unwanted effects on our study. For exam-

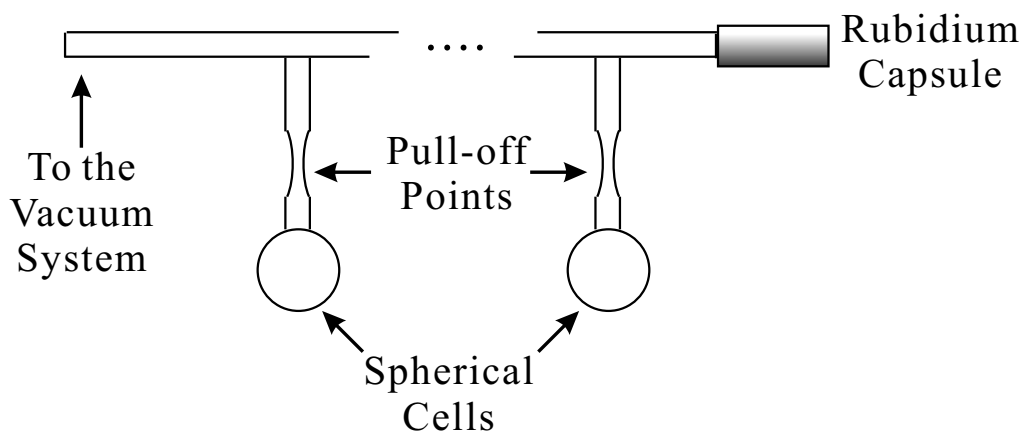


Figure 4.1: A schematic of the design of our glass manifolds. Of the five raw cells in the manifold, only two are shown. The left end of the manifold was for connecting with the vacuum system, and on the right end was a glass capsule containing Rb metal. The narrow parts in the stems of the cells were points where the filled cells were to be separated from the manifold.

ple, oxygen and water vapor react with the Rb metal, resulting in some negative consequences. First, the amount of Rb will be reduced, with the danger of leaving insufficient Rb in the cell for the SEOP process. Secondly, the rubidium oxide produced by the reactions is strongly paramagnetic (the mass magnetic susceptibility of rubidium oxide is  $1.92 \times 10^{-2}$ , while for Rb metal it is  $2.14 \times 10^{-4}$ ). The paramagnetic oxide can introduce strong magnetic field gradients in the cell, and induce extra relaxation of the  $^{129}\text{Xe}$  nuclear polarization, reducing the maximum achievable  $^{129}\text{Xe}$  polarization. There are other solid impurities that may have adverse effects if left in the manifolds. To reduce the impurities to acceptable levels, our manifolds were carefully cleaned, by rinsing with distilled water, and then with methanol. The manifolds dried for several hours, so that the water and methanol could evaporate, and then connected to a vacuum system. The manifold/vacuum system connections needed to be airtight, so the connections were sealed using epoxy.

The vacuum system was similar to filling stations used for producing polarized targets in high energy particle physics studies [39], and had been carefully designed to be able to reach an ultra high vacuum (UHV), with the residual gas pressure in the

system reduced to being on the order of  $10^{-8}$  mbar ( $10^{-11}$  atmosphere). To achieve this, two vacuum pumps were used: a turbomolecular manufactured by Pfeiffer Vacuum Technology which brought the pressure down from one atmosphere (atm) to the order of  $10^{-6}$  mbar, and an ion pump manufactured by Varian Inc. to further reduce the pressure to  $10^{-8}$  mbar. The residual gas level was monitored at two points. A Stanford Research Systems (SRS) residual gas analyzer (RGA) was placed close to the valves, and a hot ion gauge (manufactured by Inficon) was placed close to the glass manifold. A baratron (manufactured by MKS Instruments) that can measure gas pressures on the order of atmospheres was used to help filling the cells to the predetermined gas levels.

In addition to reaching UHV, a section of the system was also designed to withstand a maximum pressure of 6 atm. The system can roughly be divided into two portions: the “bottom portion,” including all the pumps and the RGA, and the “top portion,” including the connections to gas cylinders and to the glass manifold, the hot ion gauge, and the baratron. The bottom portion was held under vacuum, while the top portion worked under pressures of  $\sim 1$  atmosphere during cell fillings. The two portions were separated by a “main valve,” denoted by “V1.” The valve between the glass manifold and the rest of the system will be denoted by “V2.” Schematics of the bottom and the top portions of the vacuum system are shown in Fig. 4.2 and Fig. 4.3, respectively. To facilitate the collaborative project, we also built a new vacuum system in Stanford, identical to our existing one at Caltech, so that we could make the cells quickly and test them immediately in the Stanford imager.

When a manifold was attached to the vacuum system, we opened the valves V2, and began to remove the gases in the manifold. At room temperature, the water and some other impurities adsorbed to the glass wall usually pumped away slowly. Therefore, we used heating tapes to heat up the manifold to about  $150^{\circ}\text{C}$ , so that the vapor pressures of the impurities would increase, and the impurities were then pumped away from the manifold efficiently. Typically after 1-2 days of pumping, the gas pressure, monitored by the hot ion gauge, would drop below  $10^{-7}$  mbar. The RGA showed charts of the gas impurities, indicating the amounts of various gases.

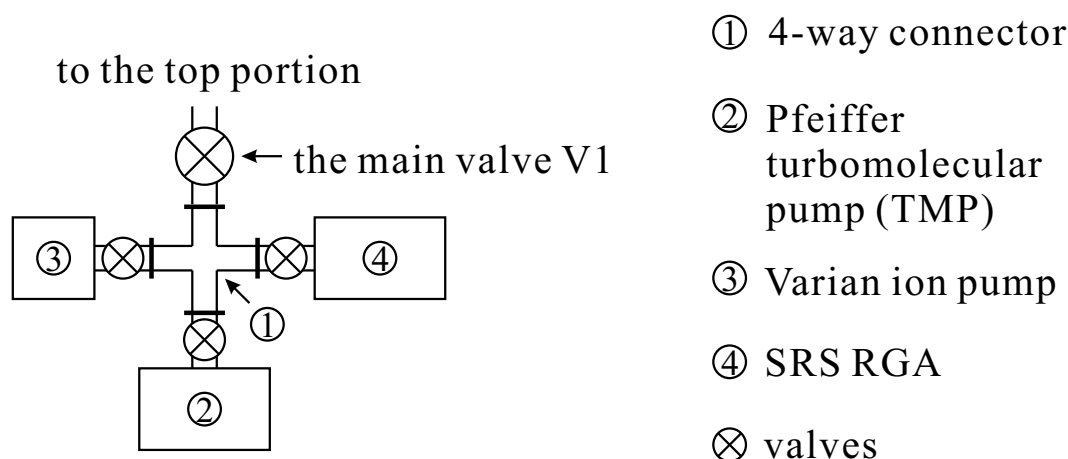


Figure 4.2: A schematic of the “bottom portion” of our vacuum system. Some of the connections between the instruments are not shown.

A typical chart is shown in Fig. 4.4. From the analysis results of the RGA, we knew that the dominant (over 50%) residual gas was  $N_2$ , which did not have any adverse effect on our studies, because  $N_2$  was one of the gases to be filled in the cells. The levels of oxygen and water was reduced to well below  $10^{-8}$  mbar, as shown in Fig. 4.4.

After the vacuum inside the manifold had reached a satisfactory level, we began to chase the Rb metal into the cells. The glass capsule containing Rb was broken, using a small magnet in the manifold, guided by a larger magnet outside of the manifold. The region around the capsule was then heated using a torch. The heated capsule was well above the melting temperature of Rb ( $39^\circ\text{C}$ ), while the rest of the manifold remained cold. The Rb vapor evaporated out of the capsule and condensed on the glass walls. By carefully heating different parts of the cell walls in turn, we directed a few milligrams of Rb metal into each of the cells.

When enough Rb had been transferred into each of the raw cells, valve V1 was closed, isolating the top portion of the system from the vacuum pumps. Gases were let out from the cylinders, first into the tubings between the cylinder valves and the pressure regulators (“buffer portions” as shown in Fig. 4.3), and then, under the control of the regulators, into the top portion of the system and into the glass manifold. This two-stage filling process enabled a precise control over the amount of

- |   |   |
|---|---|
| ① 6-way connecting cube                         | ③ baratron for high pressures (0.001~1 atm) |
| ② hot ion gauge for low pressures (< 0.001 atm) | ④ 3-way connector                           |
| ⊗ valves  | Ⓜ regulators                                |

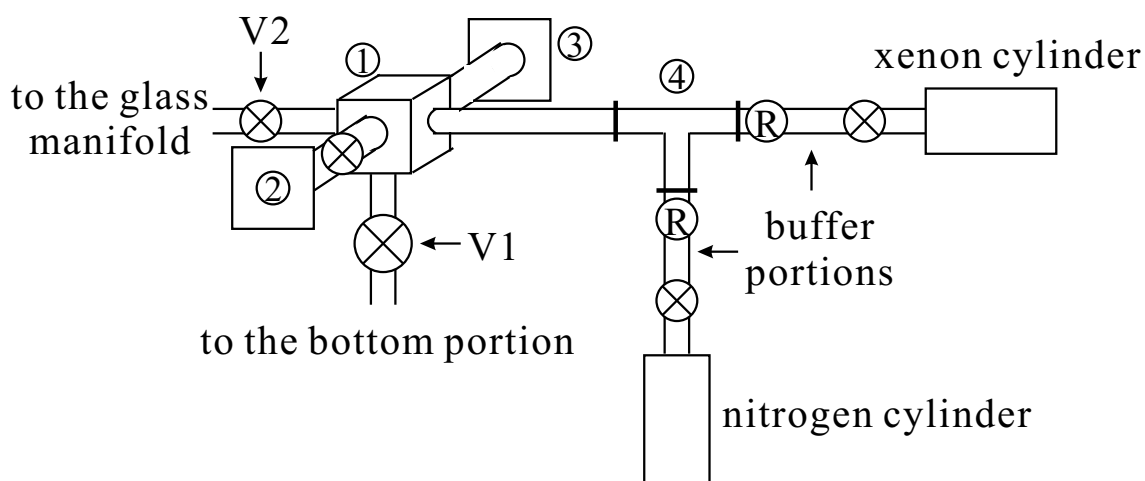


Figure 4.3: A schematic showing the “top portion” of the vacuum system. The 6-way connecting cube was used to connect 5 tubings, and the extra face was sealed off. The “buffer portions” in the figure were used for storing the gases from the cylinders before filling the cells.

gas filled into the cells. The pressure in the manifold was controlled to a precision of  $\pm 0.01$  pound per square inch (psi), or about  $\pm 7 \times 10^{-4}$  atmosphere. We used research grade Xe and N<sub>2</sub> gases with natural isotopic abundances, produced by Spectra Gases Incorporation.

After the gases had been filled in the manifold, we isolated the glass manifold from the rest of the vacuum system by closing the valve V2. We removed the cells from the manifold one by one, by heating the narrow parts in the stems using an ethyne-oxygen flame. For most of the cells, the total pressures inside were kept below one atmosphere at room temperature. As a result, when the glass at the narrow partss were softened

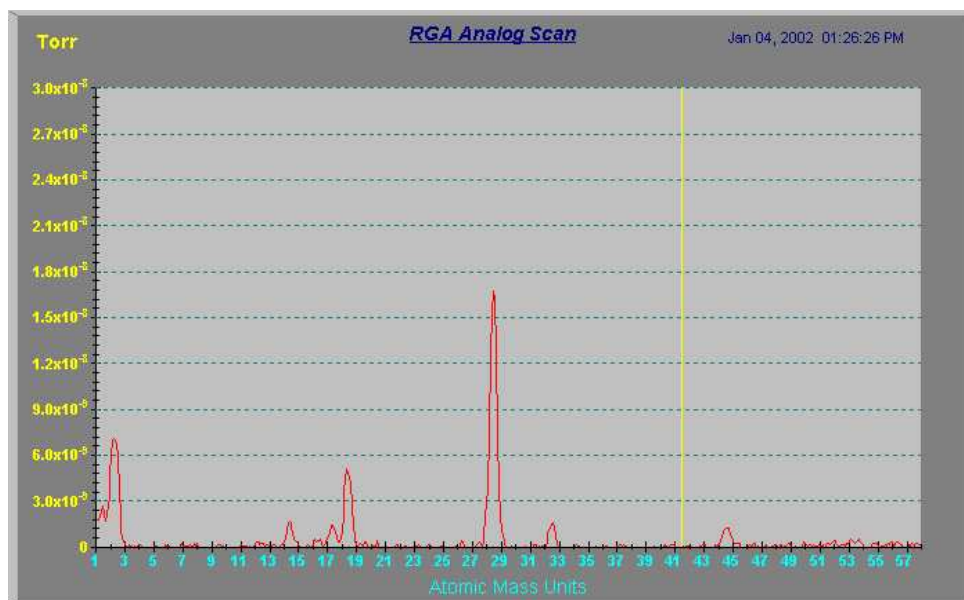


Figure 4.4: A typical readout from the RGA, after the pressure in the system had been brought down to a satisfactory level. The peak at 28 atomic mass units (AMU) corresponds to  $\text{N}_2$  molecules, and the one at 14 AMU stands for N atoms. Together they constituted over 50% of the residual pressure. The peaks at 1 and 2 AMU for hydrogen, at 16 and 32 AMU for oxygen, at 18 AMU for water, at 17 amu for hydroxyl ions ( $\text{OH}^-$ ), and at 44 AMU for carbon dioxide, were all well below  $10^{-8}$  Torr, or  $1.3 \times 10^{-8}$  mbar.

by the heat, it collapsed under the atmospheric pressure, and sealed the cells from the manifold. If cells with total pressures above 1 atmosphere at room temperature were desired, a technique called cryo-filling was applied. The raw cells were immersed in liquid nitrogen to reduced the pressures in the cells below 1 atmosphere during the sealing process. The sealed cells were then gently pulled, and separated from the manifold. After the cell removal, a portion of the stem, about 1 cm long, was left on the cell. So the finished cells were 2.5 cm (outer diameter) spheres, with 1 cm-long conical protrusions. These protrusions were mostly solid glass, and did not contribute significantly to the volume of the gas mixture in the cell. The gas volume in the sample cells were estimated to be  $\frac{1}{6}\pi((2.2 \pm 0.1) \times 10^{-2})^3 = (7.2 \pm 0.9) \times 10^{-6} \text{ m}^3$  from the above discussions.

Since the valve V2 was closed throughout each pull-off, and only the small por-

tions around the narrow parts were heated, the heating during the pull-off did not significantly change the densities of the gases in our cells. To increase the precision of the measurement of the gas densities in each cell, we performed the following procedure. After each pull-off, the manifold was allowed time to cool down to room temperature, then valve V2 was opened, and the pressure in the system was recorded by the baratron. The exact pressure inside a cell can be determined using these pressure readings and the relative ratios of the volume of the cell to the volume of the rest of the system (the rest of the glass manifold plus the top portion of the vacuum system).

For example, denote the volume of each cell on a manifold by  $V_{\text{cell}}$ , and denote the volume of the top portion of the vacuum system and the manifold excluding all the cells by  $V_0$ . The pressure before pulling off the first cell was  $P_0$ , and the pressure after the first pull-off was  $P_1$ , both measured at room temperature. From the ideal gas equation, it is easy to calculate that  $P_{\text{cell}1}$ , the pressure in the first cell measured at room temperature, was

$$P_{\text{cell}1} = \frac{P_0(V_0 + 5V_{\text{cell}}) - P_1(V_0 + 4V_{\text{cell}})}{V_{\text{cell}}} = P_0 \left( \frac{V_0}{V_{\text{cell}}} + 5 \right) - P_1 \left( \frac{V_0}{V_{\text{cell}}} + 4 \right), \quad (4.1)$$

since each of our manifolds had 5 raw cells attached to it. Similarly, the pressure in the  $i$ -th cell at room temperature was

$$P_{\text{cell}i} = P_{i-1} \left( \frac{V_0}{V_{\text{cell}}} + (6 - i) \right) - P_i \left( \frac{V_0}{V_{\text{cell}}} + (5 - i) \right), \quad (4.2)$$

where the cells were numbered according the order of the pull-off, and  $P_{i-1}$  and  $P_i$  stand for the pressure recorded by the baratron at room temperature before and after the pull-off of the  $i$ -th cell, respectively.

The volume ratio  $V_0/V_{\text{cell}}$  was obtained in the following way. Immediately after the glass manifold was connected to the vacuum system, the manifold was first pumped to a vacuum of below  $10^{-5}$  mbar, and the valve V1 leading to the pumps was closed. The valve V2 was closed as well, leaving the glass manifold under vacuum. The rest of the top portion of the system was then filled with  $\text{N}_2$ , with the pressure  $P_i$  recorded. After the valve V2 was opened again, the pressure dropped to  $P_f =$

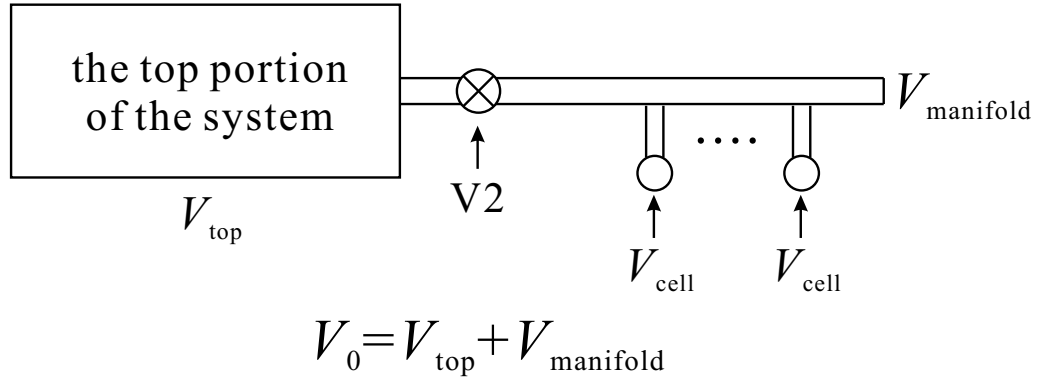


Figure 4.5: Schematic of the volumes involved in the determination of pressures in the filled cells. The italic  $V$ 's denote volumes, while V2 stands for the valve between the top portion of the vacuum system and the glass manifold. Only 2 out of the 5 raw cells are shown in the schematic.

$P_i V_{\text{top}} / (V_{\text{top}} + V_{\text{manifold}} + 5V_{\text{cell}})$ , where  $V_{\text{top}}$  denotes the volume of the top portion excluding all glass parts, and  $V_{\text{manifold}}$  is the volume of the glass manifold excluding the raw cells. Note that by definition,  $V_0 \equiv V_{\text{manifold}} + V_{\text{top}}$ . After all the pull-off's were completed, the entire top portion was pumped down to a low vacuum again, then the above process was repeated. With V1 and V2 closed, and the tubings were filled with  $\text{N}_2$  to a pressure of  $P'_i$ . The valve V2 was once more opened, and the pressure in the system became  $P'_f$ , where  $P'_f = P'_i V_{\text{top}} / (V_{\text{top}} + V_{\text{manifold}})$ . From the pressure ratios,  $R_1 \equiv P_i / P_f$  and  $R_2 \equiv P'_i / P'_f$ , we find

$$\frac{V_0}{V_{\text{cell}}} = \frac{5R_2}{R_1 - R_2}. \quad (4.3)$$

Plugging this ratio into Eq. (4.2),  $P_{\text{cell}i}$  was found for each of the cells.

For clarity, the volumes involved in the above calculations are sketched in Fig. 4.5.

The partial pressures of Xe and  $\text{N}_2$  in the cells were calculated by assuming that heating did not change the relative proportion of the two gases Xe and  $\text{N}_2$ . The pressures were converted to densities by taking the temperatures at which the pressures were measured to be  $300 \pm 2$  K. From the description above for determining the gas densities, we estimate a maximum relative uncertainty in the densities of 3%. Both for the discussions in Sec. 3.4 and for the error analysis of calibration of the  $^{129}\text{Xe}$  nuclear polarization in Sec. 4.2, this density uncertainty was used.

To check that enough Rb was in the cells, the following calculations were made. The highest temperature used during the SEOP process for this project was about 100°C. This temperature corresponded to a Rb number density of about  $3 \times 10^{18} \text{m}^{-3}$  according to the empirical formula we fitted for our conditions (Eq. (3.8)), or about  $6 \times 10^{18} \text{m}^{-3}$  according to the unmodified Killian’s formula (3.24b). Using  $7.2 \times 10^{-6} \text{m}^3$  as the volume of each of our cells, the maximum amount of Rb we needed in the cells was  $4.3 \times 10^{13}$  atoms  $\approx 7.2 \times 10^{-11}$  moles. This amount corresponds to a weight of less than  $7 \times 10^{-9}$  grams. So a few milligrams of Rb in each of our cells was indeed sufficient for the SEOP processes.

Similarly, the maximum amount of alkali metals needed in the cylindrical cells for the measurements of spin-exchange rate constants was estimated to be less than  $10^{-6}$  gram. Therefore, all the cells that we built had plenty of alkali metals for our purposes.

In the final stage of the cell building, the filled cells were placed in an oven, and heated to over 200°C. This process is called “curing” of the cells, and has been regularly applied during the productions of SEOP sample cells containing noble gases and alkali metals [11, 21, 48]. The purpose of the curing process is to ensure that the interaction between alkali vapor and the Pyrex walls reached an equilibrium, thereby reducing the wall relaxation rate to a stabilized minimum. This was especially important for the cells used in the measurements of spin-exchange rate constants (Ch. 3), where the wall relaxation rates needed to be stable.

## 4.2 $^{129}\text{Xe}$ Polarimetry

The nuclear polarizations of  $^{129}\text{Xe}$  in our sample cells were measured using the adiabatic fast passage (AFP) technique introduced in Sec. 2.3. The experimental setup was essentially the same as that described in Sec. 3.1. The diode laser was used as the light source for the SEOP process. The AFP was performed by fixing the frequency of  $\vec{B}_1$ , the rotating magnetic field, and sweeping the holding field,  $\vec{B}_0$ , past the resonance point. The strength of the rotating field  $B_1$  and the holding field’s sweep-

ing rate  $dB_0/dt$  also had the values used in Ch. 3. The rotating frequency of the field  $B_1$ , denoted as  $\omega_{B_1}$ , was 33 kHz, slightly different from the 27.6 kHz frequency used in Ch. 3. The reason for the difference was that the pickup circuit had been slightly modified between the two projects, and for each circuit, the frequency had been adjusted to produce optimal signals. As discussed below, the AFP conditions Eqs. (2.42) and (2.43) were satisfied for these experimental settings.

As discussed in Sec. 2.3, AFP produces Lorentzian-like signals in the form of Eq. (2.45),

$$|s(t)| = C\omega_{B_1}M_0\frac{B_1}{\sqrt{B_1^2 + (bt)^2}}, \quad (4.4)$$

such that the height of the signal peak is  $C\omega_{B_1}M_0$ . Following Eq. (2.35), the peak size is directly proportional to the nuclear polarization of  $^{129}\text{Xe}$  in the form of

$$S_{\text{Xe}} = C\omega_{B_1,\text{Xe}}N_{\text{Xe}}\mu_{\text{Xe}}P_{\text{Xe}}, \quad (4.5)$$

where  $S_{\text{Xe}}$  is the peak signal above the background. The quantity  $N_{\text{Xe}}$  is the total number of  $^{129}\text{Xe}$  nuclei in the sample cell, and  $\mu_{\text{Xe}}$  is the magnetic moment of a single  $^{129}\text{Xe}$  nucleus. We have used the subscript ‘‘Xe’’ to specify that these quantities pertained to  $^{129}\text{Xe}$ , in order to distinguish them from quantities pertained to water AFP signals, which will be discussed later.

The above signal  $s(t)$  is the voltage signal excited in the pick-up coils. To obtain the final signal recorded by the computer, the response of the pick-up circuit and the gain of the pre-amplifier must also be included (cf. Fig. 3.3 for the circuit). If we denote the signal recorded by the computer as  $\bar{s}_{\text{Xe}}(t)$ , and the peak size of  $\bar{s}_{\text{Xe}}(t)$  as  $\bar{S}_{\text{Xe}}$ , then

$$\bar{S}_{\text{Xe}} = C\omega_{B_1,\text{Xe}}N_{\text{Xe}}\mu_{\text{Xe}}G_{\text{preamp, Xe}}r_{\text{circuit, Xe}}P_{\text{Xe}}, \quad (4.6)$$

where  $G_{\text{preamp, Xe}}$  and  $r_{\text{circuit, Xe}}$  are the  $^{129}\text{Xe}$  AFP values of the amplification factor of the pre-amplifier, and the response of the pick-up circuit, respectively.

As described in Sec. 3.1 and shown in Fig. 3.3, the AFP signals were separated from background by the lock-in amplifier. The lock-in amplifier projected the signals

in a vector space onto the  $x$  and  $y$  directions, and then transmitted the two projections in two output channels. For the measurement of the alkali- $^{129}\text{Xe}$  spin-exchange rate constants, the total signal size was not of primary importance, since all calculations used instead the relative ratio of the two peaks from AFP signals. Therefore, in Sec. 3.1, we described the optimization of the signal-to-noise ratio (SNR) for one of the channels, and then recording the signals from that channel as our primary data. However, for the purpose of deciding the  $^{129}\text{Xe}$  polarization, the most important information came from the overall signal size of the AFP signals. Instead of optimizing the SNR for one of the channels, we projected all the AFP signal into one channel by adjusting the projection phase of the lock-in amplifier. The data used for the determination of  $P_{\text{Xe}}$  came from the channel output containing the entire AFP signal. The same applies to the water AFP signals to be discussed below.

Following Eq. (4.6),  $P_{\text{Xe}}$  can readily be calculated from the measured peak size of the AFP signal, provided that the coefficient  $C\omega_{B_1,\text{Xe}}N_{\text{Xe}}\mu_{\text{Xe}}G_{\text{preamp, Xe}}r_{\text{circuit, Xe}}$  is known. All the quantities in the expression are either known or easy to calculate or measure, except the pickup constant  $C$ . Unfortunately,  $C$  is determined by the geometrical properties of the pickup coils, and is hard to calculate directly.

To work around the difficulties in determining  $C$ , we obtained water AFP signals using a sample cell with the same specifications as our Xe sample cells, the same pair of pickup coils, and the same relative position of the cell with respect to the coils. The water signals were generated by the hydrogen nuclei (protons) in the water, and the nuclear polarization of the protons came from the Helmholtz distribution in the holding magnetic field. Following Eq. (2.34), the nuclear polarization of the protons in water sample can be calculated as  $P_w = \tanh(\mu_p B / (kT)) \approx \mu_p B / (kT)$  where the subscript “w” stands for water,  $B$  is the strength of the holding field,  $k$  is Boltzmann’s constant,  $T$  is the temperature of the water sample, and  $\mu_p$  is the magneton of a proton. We used deionized water for all our water AFP signals.

Similar to Eq. (4.6) for the peak size of a  $^{129}\text{Xe}$  AFP signal, we find the water

AFP signal is

$$\bar{S}_w = C\omega_{B_1,w}N_p\mu_pG_{\text{preamp, w}}r_{\text{circuit, w}}P_w, \quad (4.7)$$

where the subscript “w” is used to specify quantities related to the water AFP signal, with the exception of the quantities  $N$  and  $\mu$ . The subscript “p” is used for  $N$  and  $\mu$ , to make it clear that  $N_p$  is the total number of the protons in the water sample, namely two times the number of the water molecules, and  $\mu_p$  is the magneton of a single proton. Combining the above equations (4.6) and (4.7), and plugging in the expression for  $P_w$ , we find  $P_{\text{Xe}}$

$$P_{\text{Xe}} = \frac{\mu_p B}{kT} \cdot \frac{\bar{S}_{\text{Xe}}}{\bar{S}_w} \cdot \frac{\omega_{B_1,w}}{\omega_{B_1,\text{Xe}}} \cdot \frac{\mu_p}{\mu_{\text{Xe}}} \cdot \frac{N_p}{N_{\text{Xe}}} \cdot \frac{G_{\text{preamp, w}}}{G_{\text{preamp, Xe}}} \cdot \frac{r_{\text{circuit, w}}}{r_{\text{circuit, Xe}}}. \quad (4.8)$$

In the above formula the pickup constant  $C$  has been cancelled out, and all the quantities needed for the determination of  $P_{\text{Xe}}$  were either known or easily measured or calculated. The practice of comparing the sizes of the water and  $^{129}\text{Xe}$  AFP signals to calculate  $P_{\text{Xe}}$  is called “water calibration.” The above formula Eq. (4.8) will be referred to as the “water calibration formula.”

A typical water AFP signal obtained in our lab is shown in Fig. 4.6. It was obtained using a water sample cell, with identical shape and size with our  $^{129}\text{Xe}$  sample cells. It is a sphere with an inner diameter of  $(2.4 \pm 0.1)$  cm. For our experimental conditions, i.e., at room temperature, and under a magnetic field of  $\sim 20$  Gauss, the nuclear polarization of the protons in the water sample is on the order of  $10^{-9}$ . This proton polarization is much smaller than the  $^{129}\text{Xe}$  polarization resulting from the SEOP. As a result, the water signal sizes were very small, and the signal-to-noise ratio (SNR) was not as good as for  $^{129}\text{Xe}$  signals. This can be clearly observed in Fig. 4.6. To improve the SNR, water AFP signals were usually averaged over 10-100 scans, and the averaged signal sizes were used to calibrate the  $^{129}\text{Xe}$  polarization. The averaging process was automated by our Labview program. Between two consecutive signal acquisitions, a time delay of 9 seconds was allowed for the proton polarization to relax back to its equilibrium value. By inspecting the two signal peaks for water AFP signals, we estimated the relaxation time  $T_1$  of the protons in our water sample

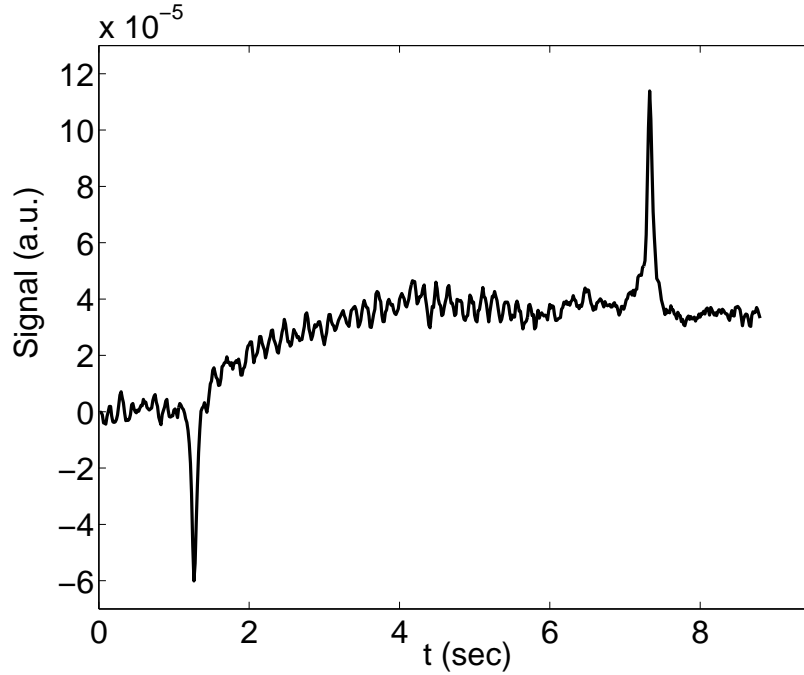


Figure 4.6: A typical water AFP signal. See text for the explanation of the two resonance peaks having different directions. The signal size is in arbitrary units. The signal-to-noise ratio is not as good as the  $^{129}\text{Xe}$  AFP signals due to the much smaller polarization of the protons in the water sample. The signals used for  $^{129}\text{Xe}$  polarization determination were averages of signals such as shown in the figure.

to be  $\lesssim 1$  sec. Therefore the interval between the signal acquisitions was 9 times  $T_1$ , enough for the proton polarization to reach equilibrium.

For water signals, the sweeping rate of the holding magnetic field  $B_0$  was the same as used for  $^{129}\text{Xe}$  AFP, but the value of  $\omega_{B_1}$  was chosen to be different, in order that that the strength of  $B_0$  at the point of resonance remained about the same as its value for  $^{129}\text{Xe}$  AFP. Since at the resonance point  $B_0 = \omega_{B_1}/\gamma$ , and the gyromagnetic ratio  $\gamma$  for protons is 3.6 times the value for  $^{129}\text{Xe}$  nuclei, we chose  $\omega_{B_1,w}$  to be 98 kHz, while  $\omega_{B_1,Xe}$  was 33 kHz.

The relaxation time of our proton polarization was much shorter than that of  $^{129}\text{Xe}$  nuclear polarization in gaseous samples. Therefore, between the two resonances in each of our AFP signals, the proton magnetization underwent several relaxation times to relax back towards its equilibrium value. Before the first resonance, the

magnetization of the sample was aligned along the direction of the effective field. Immediately after the first resonance, the magnetization followed the effective field during its reversal, and realigned opposite to the original direction. Immediately before the time of the second resonance, the magnetization had relaxed back to its original direction, and was in the opposite direction with the effective field. Since the relative direction of the magnetization with respect to the effective field determines the sign of the AFP signal, water AFP signals have the behaviour of having their two resonance peaks with different signs (on different directions, upward and downward). This behaviour can be clearly observed in Fig. 4.6, and is different from the case of the  $^{129}\text{Xe}$  AFP signals.

We now check the adiabatic and fast conditions for the water AFP process. For water, the relaxation resulting from diffusion and field inhomogeneities is much slower, since diffusions are much slower in liquids than in gases. So, following the discussions in Sec. 3.2 and dropping the  $D\frac{|\nabla B|^2}{B^2}$  term, the AFP conditions for water are  $1/T_1 \ll (\frac{dB_0}{dt}/B_1) \ll \gamma B_0$ . Taking the  $T_1$  time for the protons in our case to be 1 sec, the AFP relations became  $1 \text{ sec}^{-1} \ll 30 \text{ sec}^{-1} \ll 9.8 \times 10^4 \text{ sec}^{-1}$ , and were, indeed, satisfied.

The equilibrium value for the proton polarization was  $P_w \approx \mu_p B / (kT)$ . Immediately before the AFP resonance, the value of  $B$  was  $B = \omega_{B_1} / \gamma$ , where  $\gamma = 4.258 \times 10^7 \text{ Hz/Tesla} = 4258 \text{ Hz/Gauss}$ . However, during the AFP process,  $B$  was a time-varying quantity, and its rate of change  $\frac{dB}{dt} / B \approx 0.1 \text{ sec}^{-1}$  was faster than the relaxation rate  $1/T_1$  for the proton polarization. The actual proton polarization would lag behind its time-dependent equilibrium value. Following the discussions in Ref. [40], the average of the absolute values for the two resonance peaks is less affected by the lagging and is closer to the equilibrium value. Since the main purpose of our polarimetry measurements was to ensure that the cells would produce detectable signals in the imaging system, a high precision measurement was not necessary. Higher order corrections described in [40], therefore, were not carried out. We take the proton polarization corresponding to the averaged peak heights of the water AFP signals to be  $\mu_p(\omega_{B_1} / \gamma) / (kT) \approx 7.84 \times 10^{-9}$ . The uncertainty coming from this approximation had been estimated in Ref. [40] to be less than 5%. The temperature was taken to

be 300 K, with an uncertainty of less than 1%.

The averaged water AFP signals were fitted in the same way as described in Sec. 3.2 for the  $^{129}\text{Xe}$  signals. We estimate the uncertainties in the fits to be about 3%, for both the water and the  $^{129}\text{Xe}$  AFP.

The preamplification factor  $G_{\text{preamp}}$  was chosen to be 200 for both  $^{129}\text{Xe}$  and water proton AFP signals. The responses of the pickup circuit,  $r_{\text{circuit}}$ , were different for the two, since the two AFP frequencies occurred at different points on the response curve (Q-curve) for the pickup circuit. The pickup circuit was a simple RLC circuit, and its Q-curve was measured with the following method. A small multi-turn test coil was placed at the center of the pickup coils (i.e., where the cells would be placed during AFP tests), and at a direction perpendicular to the pickup coils. A function generator supplied the test coil with a fixed AC current, and the pickup coils detected the induced signals. Since the current was fixed, the magnetic flux that the test coil generated through the pickup coils had a fixed peak-to-peak size. The induced signal was

$$S_{\text{induced}} = \frac{d\Phi}{dt} r_{\text{circuit}} = \omega_{\text{test}} \Phi_{\text{max}} r_{\text{circuit}}, \quad (4.9)$$

where  $S_{\text{induced}}$  is the signal induced in the pickup circuit,  $\omega_{\text{test}}$  is the frequency of the AC current in the test coil, and  $\Phi_{\text{max}}$  is the maximum value of magnetic flux through the pickup coils. The quantity  $\Phi_{\text{max}}$  is determined by the AC current, and remained constant throughout the test. We recorded the induced signals by an oscilloscope while varying  $\omega_{\text{test}}$  between the AFP frequencies for  $^{129}\text{Xe}$  and for water, and the ratio of signals gave the ratio  $\omega_{B_1, \text{Xe}} r_{\text{circuit, Xe}} / (\omega_{B_1, \text{w}} r_{\text{circuit, w}})$ . The signal  $S_{\text{induced}}$  was measured to be 39.2 in arbitrary units at  $\omega_{B_1} = 33$  kHz, and 1190 at  $\omega_{B_1} = 98$  kHz. The ratio  $r_{\text{w}} \omega_{B_1, \text{w}} / (r_{\text{Xe}} \omega_{B_1, \text{Xe}}) = 30.36$  was estimated to have an uncertainty of 3% relative, the uncertainty came from the measurements of  $S_{\text{induced}}$ .

The ratio of the total numbers of nuclei,  $N_p/N_{\text{Xe}}$ , can be written as the product of two terms,  $V_{\text{w}}/V_{\text{Xe}}$  and  $n_p/n_{\text{Xe}}$ , where  $V$  stands for the volume, and  $n$  for the number density. The value of  $V_{\text{w}}/V_{\text{Xe}}$  was one, since the water sample cells were of identical specifications compared to the Xe cells. The uncertainty in the cell dimensions intro-

duced a corresponding uncertainty in the volume determinations. The inner diameter of the spherical cells was  $(2.4 \pm 0.1)$  cm, so the relative uncertainty in  $V_w/V_{Xe}$  was 12%.

The number density of  $H_2O$  molecules in water at room temperature is  $3.34 \times 10^{28} \text{ m}^{-3}$ , so  $n_p \approx 6.7 \times 10^{28} \text{ m}^{-3}$ . The uncertainty in  $n_p$  did not exceed 0.6%. The number density of Xe atoms in each sample cell was recorded during the cell building process, but it should be noted that only  $^{129}\text{Xe}$  nuclei contributed to the AFP signals, so  $n_{Xe}$  becomes 26.4% of the total Xe number densities.

The  $^{129}\text{Xe}$  nucleus has a magnetic moment of  $-0.778$  nuclear magnetons, while the proton's magnetic moment is 2.79 nuclear magnetons. The sign difference can be ignored since we recorded only absolute values, so  $\mu_p/\mu_{Xe} = 3.59$ . The uncertainty in this term is negligible.

With all the quantities in Eq. (4.8) determined, we estimated the nuclear polarization of  $^{129}\text{Xe}$  achieved in our cells. For a particular cell with good signals, we had  $\bar{S}_{Xe} = 0.17$  mV, and our water signal size was 0.07 mV after averaging the two AFP peaks. The Xe pressure in this cell was calculated to be 7.02 pound per square inch (psi), which is equal to 0.478 atmosphere. Since the pressure was measured at room temperature, the number density of Xe in the cell was  $0.478 \times 273/300 = 0.435$  amagat =  $1.17 \times 10^{25} \text{ m}^{-3}$ . The  $^{129}\text{Xe}$  number density was  $0.264 \times 1.17 \times 10^{25} = 3.09 \times 10^{24} \text{ m}^{-3}$ . Plugging in the values for the quantities in Eq. (4.8), we obtain

$$P_{Xe} = 7.84 \times 10^{-9} \cdot \frac{0.17}{0.07} \cdot \frac{2.79}{0.778} \cdot \frac{6.7 \times 10^{28}}{3.09 \times 10^{24}} \cdot 1 \cdot \frac{1190}{39.2} \approx 0.032 = 4.5\%, \quad (4.10)$$

for this cell which we denoted "C5." The  $^{129}\text{Xe}$  polarizations measured in similar cells ranged from 1% to 5%. Cell C5 was one of the cells eventually used for imaging.

The uncertainty in the AFP polarimetry for cell C5 is shown in Table 4.1. The overall uncertainty for  $P_{Xe}$  was calculated to be 14.8% relative, i.e.,  $P_{Xe} = (4.5 \pm 0.7)\%$ . This polarization was about 20% of the best reported polarization results (e.g., [18]).

Using the water calibration, we also estimated the  $^{129}\text{Xe}$  nuclear polarization in cells used for the project measuring the  $^{129}\text{Xe}$ -alkali spin-exchange rate constants (cf. Ch. 3). A cylindrical water cell with the same specifications as our Xe sample cells

Quantity	Value	Relative Uncertainty
$P_w$	$7.84 \times 10^{-9}$	5% +1%
$\bar{S}_{Xe}$	0.17 mV	3%
$\bar{S}_w$	0.07 mV	3%
$\mu_p/\mu_{Xe}$	3.59	0
$V_w/V_{Xe}$	1	12%
$n_p$	$6.7 \times 10^{28} \text{ m}^{-3}$	0.6%
$n_{Xe}$	$3.09 \times 10^{24} \text{ m}^{-3}$	3%
$G_w/G_{Xe}$	1	0
$r_w\omega_{B_1,w}/(r_{Xe}\omega_{B_1,Xe})$	30.36	3%
$P_{Xe}$	4.5%	14.8%

Table 4.1: Error analysis for the water calibration of the  $^{129}\text{Xe}$  nuclear polarization in sample cell C5. The quantity  $P_w$  has two sources of uncertainties, see the text for details. In the table, the notations  $G_{\text{preamp}}$  and  $r_{\text{circuit}}$  had been simplified to  $G$  and  $r$ , only the subscripts “w” or “Xe” are kept. The overall relative uncertainty was calculated as the square root of the square sum of all individual relative uncertainties, since these uncertainties are uncorrelated.

was used for the calibration. For the AFP signal shown in Fig. 3.5, we have tabulated in Table 4.2 the quantities that led to an estimation of the  $^{129}\text{Xe}$  polarization. For the project described in Ch. 3, there was one change in the circuit. We used two interchangeable capacitors in the pickup circuit, one for water AFP signals, and the other for  $^{129}\text{Xe}$  AFP. The two capacitors correspond to two different Q-curves for the pickup circuit. The radio frequency used for  $^{129}\text{Xe}$  signals was 27.6 kHz, and the one for water AFP was 85.9 kHz, both near the top of the Q-curve using their respective capacitor. Since the maximum response of an RLC circuit is solely determined by its resistance, and is independent of the capacitance, the circuit response  $r_{\text{circuit}}$  was taken to be the same for water and for  $^{129}\text{Xe}$ . The remaining quantities were obtained similarly with the calibration for the spherical sample cells described above. The estimated polarization is

$$P_{Xe} = 6.87 \times 10^{-9} \cdot \frac{85.9}{27.6} \cdot \frac{2.5}{0.059} \cdot \frac{2.79}{0.778} \cdot \frac{6.7 \times 10^{28}}{4.84 \times 10^{24}} \cdot \frac{20}{100} \cdot 1 \approx 0.9\%. \quad (4.11)$$

Since the exact polarization was not important for the measurements of the spin-exchange rate constants, we do not include an error analysis.

Quantity	Value
$P_w$	$6.87 \times 10^{-9}$
$\bar{S}_{Xe}$	2.5 mV
$\bar{S}_w$	0.059 mV
$\mu_p/\mu_{Xe}$	3.59
$V_w/V_{Xe}$	1
$n_p$	$6.7 \times 10^{28} \text{ m}^{-3}$
$n_{Xe}$	$4.84 \times 10^{24} \text{ m}^{-3}$
$G_w/G_{Xe}$	20/100=1/5
$r_w/r_{Xe}$	$\approx 1$
$\omega_w$	85.9 kHz
$\omega_{Xe}$	27.6 kHz
$P_{Xe}$	0.9%

Table 4.2: Water calibration for the  $^{129}\text{Xe}$  nuclear polarization in a cylindrical sample cell used for the measurements of the spin-exchange rate constants. The  $^{129}\text{Xe}$  AFP signal used for the calibration was shown in Fig. 3.5.

The  $^{129}\text{Xe}$  nuclear polarization in the cylindrical cell was lower than in the spherical cells. This was expected since the cylindrical cell has a larger volume compared to the spherical cells, while the laser power used for pumping the two types of cells remained essentially unchanged, and the  $^{129}\text{Xe}$  densities in the two cells are on the same order of magnitude. The product of the volume and the polarization for the two cells was approximately the same:  $33.5 \text{ cm}^3 \times 0.9\% \approx 30 \text{ cm}^3 \cdot \%$  for the cylindrical cell,  $7.2 \text{ cm}^3 \times 4.5\% \approx 32 \text{ cm}^3 \cdot \%$  for the spherical cell.

## 4.3 The Imaging System

### 4.3.1 The Stanford PMRI System for Water Imaging

A detailed description of the PMRI system built by the Macovski group at Stanford can be found in their original papers [25, 26]. Here, we will only present a basic description of the system. We will focus more on the experimental setup of the hyperpolarized  $^{129}\text{Xe}$  imaging part in our collaborative project.

As introduced in Sec. 2.3, the most frequently exploited MRI method uses water

signals, in which the nuclear polarizations of protons in water are induced by an external holding magnetic fields. These thermal polarizations are proportional to the holding magnetic field and inversely proportional to the environmental temperature. Therefore, to achieve the best SNR, it is desirable to use a high holding field and/or a low temperature for the imaging. In the case where *in vivo* MRI is to be performed, a high holding field is the only choice for increasing the SNR. At the same time, because the imaging process involves encoding the information about spatial positions into the NMR signals (cf. subsection 2.3.2), degradation in image quality results thus from any inherent spatial inhomogeneity or temporal instability in the holding magnetic field. To achieve good field homogeneities, magnets with larger sizes are often essential. The twofold requirement on the holding field, a high field strength and an excellent field uniformity, greatly increases the cost of a practical MRI system, and therefore limits the applicability of the MRI diagnosis method.

The Prepolarized MRI (PMRI) technique was brought to maturity in the last two decades, trying to use a novel way to reduce the cost of a MRI system. The basic idea of PMRI is that, the twofold requirement on the holding magnetic field can be divided in two pieces, and each satisfied by a different field, generated by a different set of magnet. A strong but inhomogeneous “polarizing field,”  $B_p$ , polarizes the proton spins in the image sample, and a weak but homogeneous “readout field,”  $B_r$ , acts as the holding field during the imaging. The quantity  $B_r$  is usually several hundred Gauss, and is kept on continuously, while  $B_p$  is on the order of 1 Tesla, and is turned on only for a specific duration. As soon as the protons have gained a satisfactory polarization,  $B_p$  is turned off, field gradients encoding the spacial information are turned on, and the imaging process begins. With a combination of a high field but small in size (therefore inhomogeneous) magnet and a large but low field homogeneous magnet, the fields needed for imaging can be provided. The system is constructed with a cost reduction of an order of magnitude. Nevertheless, the system produces a comparable SNR with the single magnet design. (In [26], Morgan et al. demonstrated a design of PMRI system costing \$19,000, whereas a commercial MRI system with a similar SNR costs \$136,000.)

Using the technique of PMRI, the proton polarization is proportional to the polarizing field  $B_p$ , and the loss in the polarization by the time the imaging process begins is estimated to be insignificant. The imaging SNR of a PMRI system was derived to be [26]

$$\text{SNR} \propto \frac{\omega b_1 B_p \Delta V \sqrt{t_{\text{acq}}}}{\sqrt{T_s R_s(\omega) + T_c R_c(\omega)}}, \quad (4.12)$$

where  $\omega$  is the readout frequency,  $b_1$  is the receiver coil sensitivity,  $\Delta V$  is the “voxel size” defined as the smallest distinguishable volume in the image,  $t_{\text{acq}}$  is the total imaging time,  $T_s$  and  $T_c$  are the temperatures of the sample and the receiver coils, and  $R_s$  and  $R_c$  are the resistances of the sample and the receiver coils. The sample resistance  $R_s$  is proportional to the square of the readout frequency, whereas  $R_c$  varies more slowly with the frequency. Therefore, when the readout frequency is sufficiently high, we can usually assume that the body noise dominates over the coil noise, i.e.,  $T_s R_s \gg T_c R_c$ . In this “body noise domination scenario,” the  $\omega$  term in the SNR gets cancelled out in the SNR, and we are left with

$$\text{SNR} \propto \frac{B_p \Delta V \sqrt{t_{\text{acq}}}}{\sqrt{T_s}}. \quad (4.13)$$

Compared with conventional MRI, the readout frequency  $\omega$  of PMRI is much lower, since the readout magnetic field is lower. The MRI signal size is always proportional to the proton polarization. In PMRI, the proton polarization is proportional to the polarizing field  $B_p$ , while in MRI, the polarization is proportional to the holding field. As seen in Eq. (4.13), the imaging SNR is independent of  $\omega$ . So we conclude that, in the body noise domination scenario, a PMRI system can have comparable SNR with a MRI system, provided that the polarizing field is the same, i.e.,  $B_p = B_0$ .

A schematic of the prototype PMRI system can be found in Fig. 4.7. The polarizing and the readout magnets are separately shown. A set of radio frequency (RF) coils both provide the RF excitation pulses, and pickup the NMR signals from the sample. The transmit/receive (T/R) switch controls the RF circuit and switches the circuit between its two functions. A RF source feeds the RF coils with the excitation pulses. The preamplifiers receive the image signals, and amplify them. The frequency of the

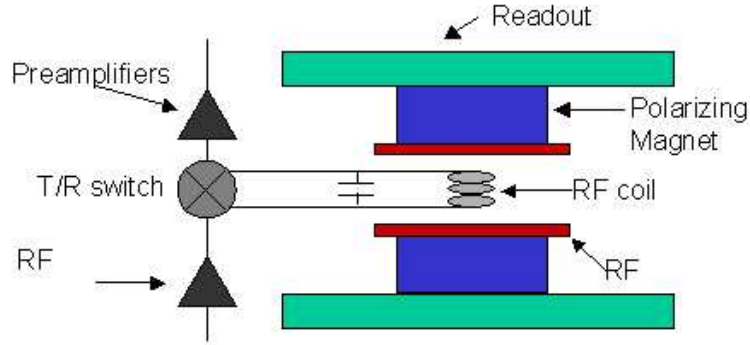


Figure 4.7: Schematic demonstrating the design of a PMRI system. Two sets of magnets together provide the holding magnetic field. The RF coils generate the excitation pulses, and also record the image signals.

signals is determined by the readout field  $B_r$ , in that  $\omega = \gamma B_r$ , where  $\gamma$  is the gyromagnetic ratio. For the particular system at Stanford,  $B_p = 0.3$  T, with a uniformity of about 20%, and  $B_r$  can be adjusted between 0 and 350 Gauss, with a uniformity  $\sim 10$  ppm throughout the imaging volume of  $\sim 1000$  cm<sup>3</sup>. The polarizing field is turned on for 300 ms to polarize the protons in the sample before each acquisition.

To demonstrate the imaging quality of the PMRI system, an image of a water sample cell was produced, shown in Fig. 4.8 [17]. The sample cell had the same specifications as the <sup>129</sup>Xe sample cells used for the imaging, namely a spherical cell with  $(2.4 \pm 0.1)$  cm inner diameter. The readout magnetic field used for the image was 93.7 Gauss, corresponding to a readout frequency of 399 kHz. The total imaging time  $t_{\text{acq}}$  was 10 s. The technique of two-dimensional Fourier transform imaging (2DFT imaging, cf. Sec. 2.3) was used for the image. The resulting image is two-dimensional without slice selection, i.e., a projection of the three-dimensional cell into a single plane. Therefore, the center of the image is brighter than the edge. The water sample cell imitated the protrusion on the <sup>129</sup>Xe cells, and the protrusion is also observed in the upper edge of the cell. The imaging field of vision (FOV) was 10 cm  $\times$  10 cm, and was divided into an “imaging matrix” of 64  $\times$  128. So, the resolution of the image in the two-dimensional plane is 1.56 mm  $\times$  0.78 mm.

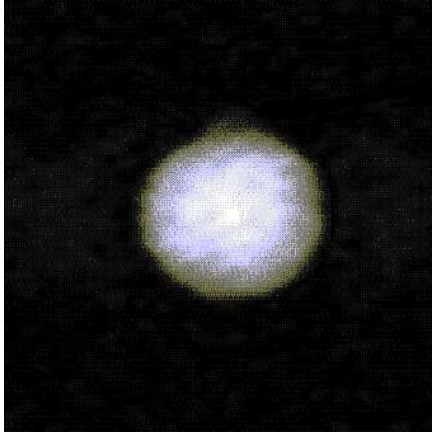


Figure 4.8: An image of a spherical water sample cell, using the PMRI system constructed by the Macovski group. The 2DFT image without slice selection corresponded to the projection of the 3D cell into a plane.

### 4.3.2 Experimental Design for Performing Hyperpolarized $^{129}\text{Xe}$ MRI in the PMRI System

MRI using laser-polarized  $^{129}\text{Xe}$ , usually named hyperpolarized  $^{129}\text{Xe}$  MRI in the field of MRI, does not require a high readout magnetic field to achieve high SNR's. Similar to the derivation of Eq. (4.13), we have estimated that the SNR of hyperpolarized  $^{129}\text{Xe}$  MRI is, in the body noise dominance scenario,

$$\text{SNR} \propto \frac{P_{\text{Xe}} \Delta V \sqrt{t_{\text{acq}}}}{\sqrt{T_s}}, \quad (4.14)$$

where  $P_{\text{Xe}}$  is the nuclear polarization of  $^{129}\text{Xe}$  obtained from the SEOP process. Since the two imaging techniques, hyperpolarized  $^{129}\text{Xe}$  MRI and PMRI, have the common merit of producing high SNR in low readout fields, they can be realized using a single low field imaging system.

A straightforward experimental design to perform hyperpolarized  $^{129}\text{Xe}$  MRI using the PMRI system, would be to use the readout field of the system as the holding field both for the SEOP and for the imaging, and the polarizing field for PMRI would not be necessary, nor would any extra magnetic field be needed. However, there was a technical difficulty with this design. The bore of the polarizing magnet had

a small size ( $\sim 10$  cm in diameter), making it difficult to design an oven, which can fit in the bore and heat the cell, yet does not interfere with the magnetic field. Therefore, we decided on another design, in which the sample cell was polarized in another independent holding magnetic field, and was subsequently transferred into the imaging system. The magnetization of the sample cell would align with the earth magnetic field during the transfer, and upon entering the imaging system, it would realign with the readout field, and be ready for the imaging.

We built a smaller, and more portable pair of Helmholtz coils to provide the holding magnetic for the SEOP process for this project. The coils had a diameter of about 50 cm, and they produced a magnetic field of about 45 Gauss in the central region, where SEOP was performed. The field gradient at the central of the coils was measured to be  $\lesssim 0.4$  Gauss/cm. During the polarizing stage, the sample cell would be placed at the coils' center, laser beam from the diode laser would be guided to the cell. Since the purpose of the magnetic field was solely for the SEOP, a good field homogeneity was not required, and it was not essential to keep all ferromagnetic elements away from the coil. So, to make the setup simple and portable, we used a heat gun, instead of an oven, to maintain the cell temperature of about  $100^\circ\text{C}$ . A schematic of the polarizing system can be found in Fig. 4.9. Not shown in the sketch is the resistance temperature detector (RTD) for monitoring the cell temperature.

One problem with the above design is the loss of  $^{129}\text{Xe}$  nuclear polarization during the transfer and the imaging stages. During the SEOP, the cell had to be at a temperature of about  $100^\circ\text{C}$ , so that it contained Rb vapor of a sufficiently high density for the SEOP. Once the cell left the laser beam, the Rb vapor would change from a source of polarization into a sink, and contribute a large portion of the relaxation of  $^{129}\text{Xe}$  polarization. A high cell temperature would also increase the sample noise level. So, it was desirable for the cell to be cooled down between the polarizing and the imaging processes. In practice, the cell was immersed in cold water for about 5 seconds so that its temperature decreased to  $40\text{-}50^\circ\text{C}$ , and the Rb vapor density in the cell became negligible.

The time it took to transfer the cell from the polarizing system to the imaging

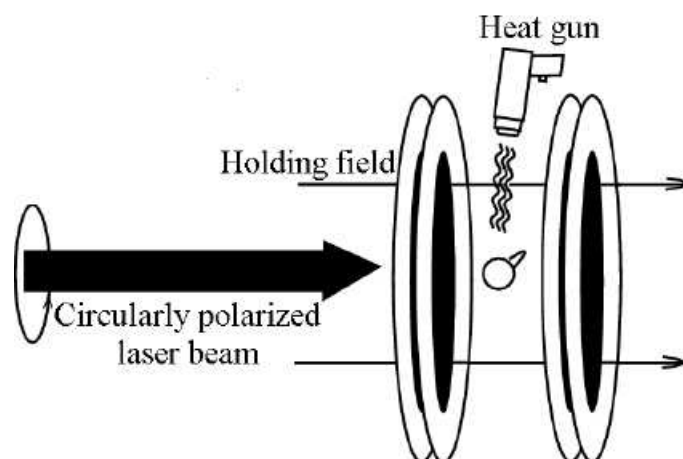


Figure 4.9: A sketch of the polarizing system for our hyperpolarized  $^{129}\text{Xe}$  imaging study. A diode laser provided the beam for SEOP, a pair of Helmholtz coils provided the holding magnetic field. The sample cell was heated using a heat gun to about  $100^\circ\text{C}$ .

system, including the immersion in water, was about 10 seconds. The imaging time was about 15 seconds. So, we had to make sure that throughout the imaging time, the  $^{129}\text{Xe}$  in the cell had a sufficient nuclear polarization. In other words, we needed to check that the relaxation time of the nuclear polarization of  $^{129}\text{Xe}$  in the sample cell would not be much shorter than 25 seconds, and the transfer would not induce any extra loss in the  $^{129}\text{Xe}$  polarization.

To test the feasibility of the plan of transferring the cell before imaging, we carried out a measurement at Caltech, before shipping the cells and coils to Stanford. A sample cell was put in the center region of the coils, heated up, and underwent approximately 10 minutes of SEOP. The cell was then removed from the polarizing field, immersed in cold water for 5 seconds, and put in the AFP system at Caltech (described in Sec. 3.1). We then performed several consecutive AFP measurements. It turned out that on average, we were able to obtain 3-5  $^{129}\text{Xe}$  AFP signals, before the signal decayed to unacceptably low levels. Cell C5, which was used as an example of water calibration for the  $^{129}\text{Xe}$  nuclear polarization, had a particularly long lifetime. The lock-in amplifier was adjusted so that for each AFP signal, the entire signal was

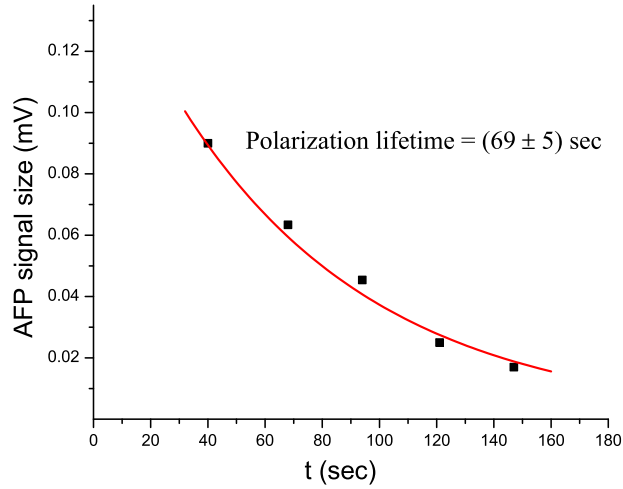


Figure 4.10: Time-decay of AFP signals produced by cell C5. These signals were obtained after the  $^{129}\text{Xe}$  inside had been polarized to an equilibrium value by SEOP, and the cell had been removed from the laser beam, cooled and placed in the AFP system. The  $t = 0$  point corresponded to the time when the cell was removed from the laser beam. The square data points were first peaks of the AFP signals. From them a solid line is fitted as an exponential decay.

projected into one output channel, and we used the first of the two peaks for the analysis. The size of these first peaks was plotted as a function of time, and fitted to an exponential decay. From the fit, we estimate the  $^{129}\text{Xe}$  nuclear polarization lifetime in cell C5 to be  $(69 \pm 5)$  sec. The plot and the fit are shown in Fig. 4.10. Note that the lifetime was obtained at 40-50°C (i.e., when no Rb vapor was in the cell to interact with the  $^{129}\text{Xe}$  nuclei).

Fits as in Fig. 4.10 were not accurate enough for the purpose of determining the spin-exchange rate constants (so we used other approaches in Ch. 3), but it was safe to conclude from them that, after being transferred from the polarizing system to the imaging system, the  $^{129}\text{Xe}$  nuclear polarizations in the cells would still be sufficiently large for the imaging. It should be noted that, in this design of polarizing and imaging in different magnetic fields, to calculate the SNR of hyperpolarized  $^{129}\text{Xe}$  MRI, the quantity  $P_{\text{Xe}}$  in Eq. (4.14) should be interpreted as the time average of  $P_{\text{Xe}}(t)$  during

the imaging time. If the lifetime of  $P_{Xe}$  was 70 sec, the time between the sample cell's removal from the polarizing laser beam and the beginning of imaging was 10 sec, and the imaging lasted 15 sec, then the averaged  $P_{Xe}$  would be about one fourth less than the equilibrium value of  $P_{Xe}$  during the SEOP process.

Two of our spherical sample cells, labelled as C3 and C5, were selected for the final imaging studies. They both had long  $^{129}\text{Xe}$  polarization lifetimes (i.e.,  $\sim 70$  seconds), and they both produced equilibrium  $^{129}\text{Xe}$  polarizations of 3-5% during SEOP. They were shipped to Stanford together with the small pair of Helmholtz coils, and we proceeded to image them.

## 4.4 Imaging Results

At Stanford, we set up the polarizing system in the same way as described in subsection 4.3.2, and performed the following tests with the polarize-and-transfer approach described above. For a first test, we tried to produce a NMR signal of the  $^{129}\text{Xe}$  sample cell without encoding the spatial information, that is, without separating the signals generated by different parts of the cell. The result is shown in Fig. 4.11. In the figure, the  $x$ -axis is " $\Delta f$ ," defined as the frequency detuning from the resonance frequency. The signal size is given in arbitrary units. The readout field used for the signal was 33.6 mT=336 Gauss, corresponding to the resonance frequency of 398 kHz. The bandwidth of the receiving circuit was set to be  $\pm 2415$  kHz, for this signal and for all the following NMR signals. The polarizing magnetic field was not activated. The SNR for the signal was estimated to be 20:1, and was satisfactory for performing imaging tests.

For comparison, we also recorded two water NMR signals. For the acquisition of the first water signal, the prepolarizing technique was applied. The polarizing magnetic field was 0.3 T, and the readout field had the same strength as the  $^{129}\text{Xe}$  NMR, corresponding to a resonance frequency of 1430 kHz. The NMR signal is shown in Fig. 4.12. The plot is centered on the resonance frequency 1430 kHz. The SNR of the signal was estimated to be 100:1.

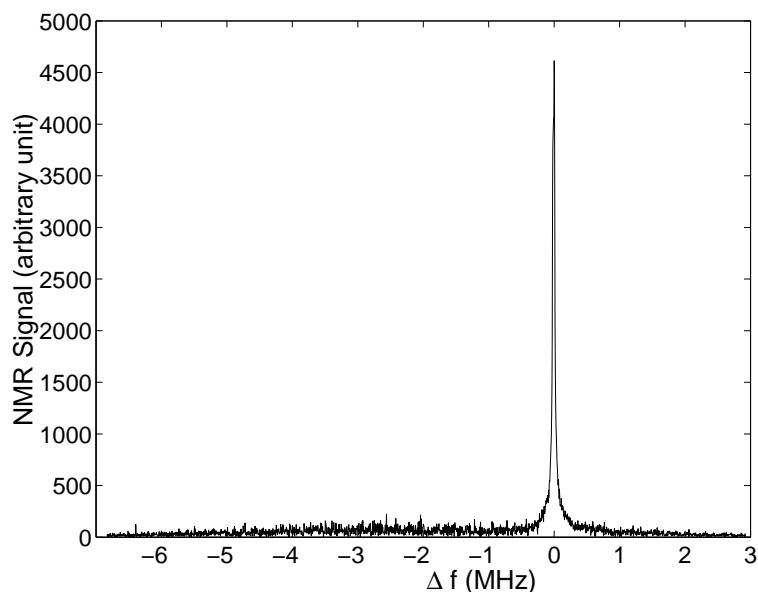


Figure 4.11: A NMR signal obtained using a sample cell containing hyperpolarized  $^{129}\text{Xe}$ .

For a second test, we performed water NMR without the prepolarizing process. The proton polarization was the thermal polarization induced by the readout magnetic field. The resonance frequency was chosen to be approximately the same as the  $^{129}\text{Xe}$  NMR frequency, so the readout magnetic field was set at 9.37 mT, which corresponds to a resonance frequency of 399 kHz. The water signal is shown in Fig. 4.13. The plot is also centered at the resonance frequency. The signal had a SNR of  $\sim 10:1$ .

From the three NMR signals, it is clear that both the hyperpolarizing technique and the prepolarizing technique can produce low magnetic field NMR signals with good SNR.

Next, we tried to obtain hyperpolarized  $^{129}\text{Xe}$  MR images. We performed the 2DFT imaging without slice selection. A RF pulse was used to tip all the  $^{129}\text{Xe}$  magnetons in the sample cell (not just a slice of atoms) by  $13.5^\circ$ . Imaging signals were then recorded, and the magnetization returned to the direction of the holding field due to the “ $T_2$  processes” (cf. subsection 2.3.1). Such a signal acquisition period lasted 255 msec, and was repeated 64 times. The total imaging time was 16.3 seconds.

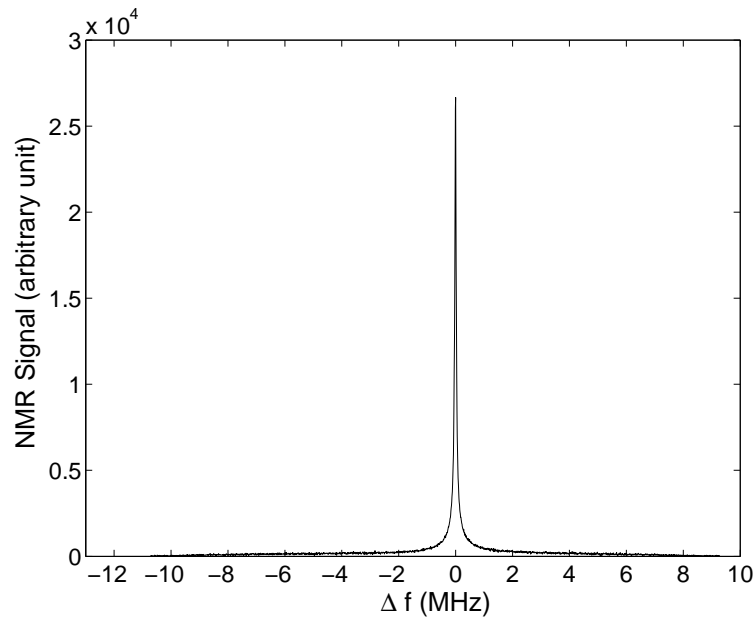


Figure 4.12: A water NMR signal, obtained using the prepolarizing technique. The sample cell was a spherical one containing deionized water, and had the same size as the  $^{129}\text{Xe}$  sample cells.

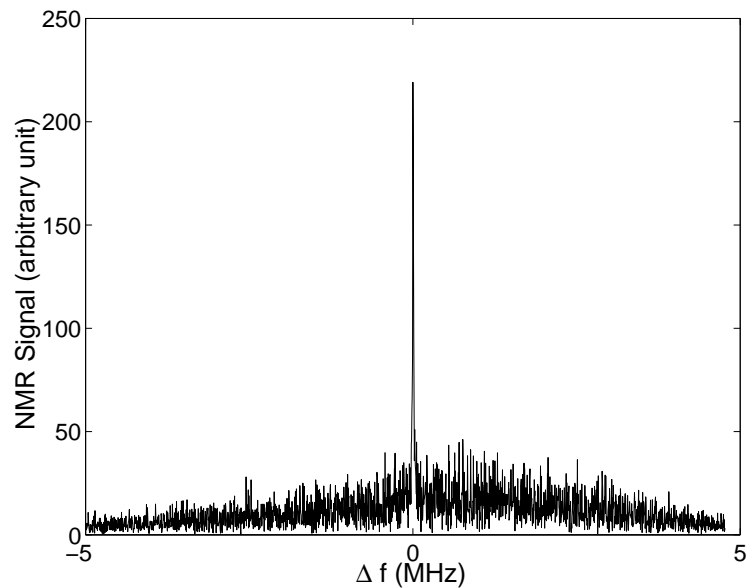


Figure 4.13: A water NMR signal obtained using the water sample cell, exploiting only the thermal proton polarization induced by the readout magnetic field.

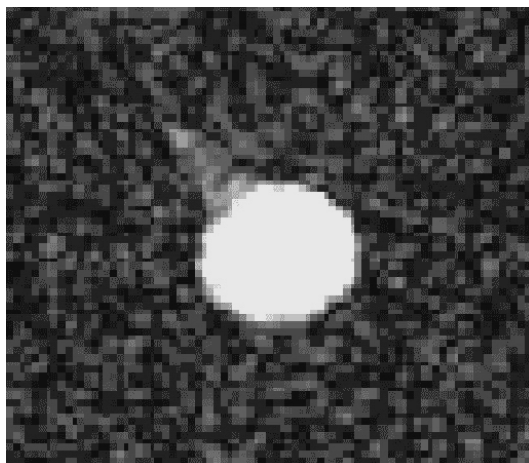


Figure 4.14: A hyperpolarized  $^{129}\text{Xe}$  MRI, obtained under a low readout magnetic field.

The imaging FOV was  $14.5\text{ cm}\times 10\text{ cm}$ , and the imaging matrix was  $128\times 64$ , so the resolution in the  $x$ - $y$  plane was  $1.13\text{ mm}\times 1.56\text{ mm}$ . The imaging result is shown in Fig. 4.14. In the figure, the display has been magnified to a field of vision of  $4\text{ cm}\times 3.5\text{ cm}$ . The profile of the spherical cell with a protrusion can be clearly discerned in the figure.

To summarize, the hyperpolarized noble gas MRI, in particular the hyperpolarized  $^{129}\text{Xe}$  MRI, has the following advantages over conventional water proton MRI. As an imaging agent,  $^{129}\text{Xe}$  produces good imaging SNR, without requiring a high magnetic field ( $\gtrsim 0.05$  Tesla), and therefore, the cost of the magnets in the imaging system can be greatly reduced. The gaseous nature of  $^{129}\text{Xe}$  enables MRI of void-spaces, for example lungs. At the same time, unlike  $^3\text{He}$ ,  $^{129}\text{Xe}$  can dissolve in blood, so MRI of other tissues is also possible. Because  $^{129}\text{Xe}$  is not naturally abundant in the human body, the imaging agent will be concentrated in the region where it is injected/inhaled, and the background signal will be minimal. Due to  $^{129}\text{Xe}$ 's larger chemical shift, it has a better sensitivity to the environments. For example, the  $^{129}\text{Xe}$  chemical shift is dependent on the oxygenation level of the blood, and this feature has been exploited in the work by Wolber *et al.* [49].

On the other hand, compared with water MRI, the disadvantages of hyperpo-

larized  $^{129}\text{Xe}$  MRI include: the  $^{129}\text{Xe}$  nuclear polarization induced by SEOP is a non-equilibrium polarization, and it decays with time, usually on the timescale of several tens of seconds. The polarization decay limits the available time for transferring polarized  $^{129}\text{Xe}$  to the part to be imaged, and for performing MRI. Techniques of freezing polarized  $^{129}\text{Xe}$  during the transfer have been proposed and developed (e.g., [18]). Also, the achievable density of  $^{129}\text{Xe}$  in human body is low, either when Xe is inhaled as a gas or is injected as a solute. Since the MRI signal is proportional to the density of the imaging agent, the low  $^{129}\text{Xe}$  density is a disadvantage, and high nuclear polarizations must be achieved to make the technique practical.

The Prepolarized MRI (PMRI) technique uses protons as the imaging agent, and uses low readout magnetic fields. Like hyperpolarized  $^{129}\text{Xe}$  MRI, PMRI can also achieve comparable SNR with high magnetic field MRI, so it can also reduce the cost of the imaging magnets. The proton polarizations induced by the prepolarizing process are non-equilibrium as well, so the polarizing magnet has to be activated before every signal acquisition period during the imaging process.

Before our project, low field  $^{129}\text{Xe}$  imaging had been reported, for example in works by Augustine *et al.* [50] and Tseng *et al.* [51]. Our collaborative project demonstrated the first successful attempt to perform both hyperpolarized  $^{129}\text{Xe}$  imaging and water imaging in the same system, under low magnetic field and room temperature. The results of our project have been previously reported in [17].

## Chapter 5

# Future Outlook

Noble gases with nuclear spin-1/2, in particular  $^{129}\text{Xe}$ , can receive nuclear spin polarizations through spin-exchange optical pumping processes. The nuclear polarizations thus obtained can be utilized in various applications, including magnetical resonance imaging for medical diagnose. However, the current achievable nuclear polarization for  $^{129}\text{Xe}$  is still not high enough to become practical for diversified applications. Therefore, efforts to achieve higher  $^{129}\text{Xe}$  polarization are still important.

In this thesis, two research projects have been introduced in detail, and their outcomes presented. The first project served to determine the constants that characterize the rate of spin-exchange between  $^{129}\text{Xe}$  and alkali metals K, Rb, and Cs. Knowledge of these constants can help predict the build-up rate of  $^{129}\text{Xe}$  polarization through SEOP, as well as the maximum achievable  $^{129}\text{Xe}$  polarization for a particular polarizing scenario. This project was the first to measure the spin-exchange rate constants between  $^{129}\text{Xe}$  and the alkalis K and Cs at cell densities of  $\lesssim 1$  amagat. In the project, direct measurements of the alkali number densities in the sample cells were carried out using the Faraday rotation method. These measurements can provide more accurate alkali densities than empirical formulae found in the literature.

The second project explored the possibility of using hyperpolarized  $^{129}\text{Xe}$  as an agent for MRI with low magnetic fields. In this project, we demonstrate the first successful attempt to build a MRI system using a low readout magnetic field ( $\sim 0.01$  Tesla) which can perform both water MRI and hyperpolarized  $^{129}\text{Xe}$  MRI. The water MRI was performed using the technique of Prepolarized MRI developed by the

Macovski group at Stanford university.

For a given SEOP scenario (i.e., fixed laser availability and laser power, fixed wall relaxation rate of  $^{129}\text{Xe}$  polarization in the sample cells, etc.), the knowledge of the spin-exchange rate constants can help choosing the polarizing parameters necessary to optimize the production of hyperpolarized  $^{129}\text{Xe}$  samples. These parameters include the choice of alkali metal, the experimental cell temperature and thus the vapor density of the alkali metal, and the densities of Xe and  $\text{N}_2$  in the sample cell. Future studies can be designed to achieve better efficiency for producing polarized  $^{129}\text{Xe}$  sample in various applications. Coating the inner walls of the sample cells to reduce the wall relaxation rate of  $^{129}\text{Xe}$  polarization [52, 53], and developments of cheaper lasers would also facilitate in the mass production of hyperpolarized  $^{129}\text{Xe}$ . Numerous research groups are also exploiting polarized  $^{129}\text{Xe}$  with the current achievable polarizations, for medical and material applications (for example, [54, 55]). The study of polarized  $^{129}\text{Xe}$  is still a lively and active field with many promising applications. Achieving high polarizations for large volume  $^{129}\text{Xe}$  is still a fruitful endeavor.

# Bibliography

- [1] F. D. Colegrove, L. D. Schearer, and G. K. Walters, *Phys. Rev.* **132**, 2561 (1963).
- [2] M. A. Bouchiat, T. R. Carver, and C. M. Varnum, *Phys. Rev. Lett.* **5**, 373 (1960).
- [3] P. L. Anthony *et al.*, *Phys. Rev. Lett.* **71**, 959 (1993).
- [4] A. K. Thompson *et al.*, *Phys. Rev. Lett.* **68**, 2901 (1992).
- [5] K. Abe *et al.*, *Phys. Rev. Lett.* **79**, 26 (1997).
- [6] B. Saam, D. A. Yablonskiy, D. S. Gierada, and M. S. Conradi, *Mag. Res. Med.*, **42**, 507 (1999).
- [7] W. Happer, E. Miron, S. Schaefer, D. Schreiber, W. A. van Wijngaarden, and X. Zeng, *Phys. Rev. A* **29**, 3092 (1984).
- [8] S. Appelt, A. Ben-Amar Baranga, C. J. Erickson, M. V. Romalis, A. R. Young, and W. Happer, *Phys. Rev. A* **58**, 1412 (1998).
- [9] A. Ben-Amar Baranga, S. Appelt, M. V. Romalis, C. J. Erickson, A. R. Young, G. D. Gates, and W. Happer, *Phys. Rev. Lett.* **80**, 2801 (1998).
- [10] B. Grover, *Phys. Rev. A* **28**, 2521 (1983).
- [11] X. Zeng, Z. Wu, T. Call, E. Miron, D. Schreiber, and W. Happer, *Phys. Rev. A* **31**, 260 (1985).
- [12] M. S. Albert, G. D. Cates, B. Driehuys, W. Happer, B. Saam, C. S. Springer, and A. Wishnia, *Nature* **370**, 188 (1994).

- [13] Y. Q. Song, B. M. Goodson, and A. Pines, *Spectroscopy* **14**, 26 (1999).
- [14] D. Raftery, H. Long, T. Meersmann, P. J. Grandinetti, L. Reven, and A. Pines, *Phys. Rev. Lett.* **66**, 584 (1993).
- [15] J. P. Butler, R. W. Mair, D. Hoffmann, M. I. Hrovat, R. A. Rogers, G. P. Topulos, R. L. Walsworth, and S. Patz, *J. Phys.-Cond. Mat.* **14**, L297 (2002).
- [16] M. V. Romalis, and M. P. Ledbetter, *Phys. Rev. Lett.* **87**, 067601 (2001).
- [17] W. Shao, G. Wang, R. Fuzesy, E. W. Hughes, B. A. Chronik, G. C. Scott, S. M. Conolly, and A. Macovski, *App. Phys. Lett.* **80**, 2032 (2002).
- [18] B. Driehuys, G. D. Cates, E. Miron, K. Sauer, D. K. Walter, and W. Happer, *App. Phys. Lett.* **69**, 1668 (1996).
- [19] C. H. Volk, T. M. Kwon, and J. G. Mark, *Phys. Rev. A* **21**, 1549 (1980).
- [20] G. D. Cates, R. J. Fitzgerald, A. S. Barton, P. Bogorad, M. Gatzke, N. R. Newbury, and B. Saam, *Phys. Rev. A* **45**, 4631 (1992).
- [21] Y. Y. Jau, N. N. Kuzma, and W. Happer, *Phys. Rev. A* **66**, 052710 (2002).
- [22] B. Chann, E. Babcock, L. W. Anderson, and T. G. Walker, *Phys. Rev. A* **66**, 032703 (2002).
- [23] Z. Wu, M. Kitano, W. Happer, M. Hou, and J. Daniels, *App. Opt.* **25**, 4483 (1986).
- [24] P. T. Callaghan, *Principles of Nuclear Magnetic Microscopy*, Oxford University Press, New York, 1993
- [25] A. Macovski and S. M. Conolly, *Mag. Res. Med.* **30**, 221 (1993).
- [26] P. Morgan, S. Conolly, G. Scott, and A. Macovski, *Mag. Res. Med.* **36**, 527 (1996).
- [27] W. A. J. Kastler, *J. Phys. Radium* **11**, 225 (1950).

- [28] W. Happer, *Rev. Mod. Phys.* **44**, 169 (1972).
- [29] L. W. Anderson, F. M. Pipkin, and J. C. Baird, *Phys. Rev.* **120**, 1279 (1960).
- [30] L. D. Schearer and G. K. Walters, *Phys. Rev. A* **139**, A1398 (1965).
- [31] G. D. Cates, S. R. Schaefer, and W. Happer, *Phys. Rev. A* **37**, 2877 (1988).
- [32] B. Chann, I. A. Nelson, L. W. Anderson, B. Driehuys, and T. G. Walker, *Phys. Rev. Lett.* **88**, 113201 (2002).
- [33] M. Bencsik and C. Ramanathan, *Mag. Res. Imag.* **19**, 379 (2001).
- [34] A. Abragam, *The Principles of Nuclear Magnetism* (Oxford University Press, Oxford, England, 1961)
- [35] F. Bloch, *Phys. Rev.* **70**, 460 (1946).
- [36] N. Bloembergen, E. M. Purcell, and R. V. Pound, *Phys. Rev.* **73**, 679 (1948).
- [37] R. C. Welsh, T. E. Chupp, K. P. Coulter, M. S. Rosen, and S. D. Swanson, *Nucl. Inst. Meth. A* **402**, 461 (1998).
- [38] E. L. Hahn, *Phys. Rev.* **80**, 580 (1950).
- [39] J. R. Johnson *et al.*, *Nucl. Inst. Meth. A* **356**, 148 (1995).
- [40] H. L. Middleton, Ph. D. thesis, Princeton University, 1994.
- [41] M. V. Romalis, Ph. D. thesis, Princeton University, 1994.
- [42] T. J. Killian, *Phys. Rev.* **27**, 578 (1926).
- [43] C. J. Smithells, *Metals Reference Book*, 4th ed., Butterworths (1967).
- [44] *Handbook of Chemistry and Physics*, 82 ed., 2001/2002. data from 1984 Canadian metallurgical quarterly.
- [45] A. N. Nesmeyanov, *Vapor Pressure of the Elements* (Academic, New York, 1963)

- [46] E. Vliegen, S. Kadlecck, L. W. Anderson, T. G. Walker, C. J. Erickson, and W. Happer, *Nucl. Inst. Meth. A* **460**, 444 (2000).
- [47] A. Wong-Foy, S. Saxena, A. J. Moule, H. M. L. Bitter, J. A. Seeley, R. McDermott, J. Clarke, and A. Pines, *J. Mag. Res.* **157** (2), 235 (2002).
- [48] Z. Wu, W. Happer, M. Kitano, and J. Daniels, *Phys. Rev. A* **42**, 2774 (1990).
- [49] J. Wolber, A. Cherubini, M. O. Leach, and A. Bifone, *European Radiology* **9**, B42 (1999).
- [50] M. P. Augustine, A. Wong-Foy, J. L. Yarger, M. Tomaselli, A. Pines, D. M. Ton-That, and J. Clarke, *App. Phys. Lett.* **72**, 1908 (1998).
- [51] C. H. Tseng, G. P. Wong, V. R. Pomeroy, R. W. Mair, D. P. Hinton, D. Hoffmann, R. E. Stoner, F. W. Hersman, D. G. Cory, and R. L. Walsworth, *Phys. Rev. Lett.* **81**, 3785 (1998).
- [52] X. Zeng, E. Miron, W. A. van Wijngaarden, D. Schreiber, and W. Happer, *Phys. Lett. A* **96**, 191 (1983).
- [53] S. R. Breeze, S. Lang, I. Moudrakovski, C. I. Ratcliffe, J. A. Ripmeester, G. Santyr, B. Simard, and I. Zuger, *J. of App. Phys.* **87**, 8013 (2000).
- [54] C. M. Hillenbrand, D. R. Elgort, E. Y. Wong, A. Raykowski, F. K. Wacker, J. S. Lewin, and J. L. Duerk, *Mag. Res. Med.* **51**, 668 (2004).
- [55] R. W. Mair, R. Wang, M. S. Rosen, D. Candela, D. G. Cory, and R. L. Walsworth, *Mag. Res. Imag.* **21**, 287 (2003).

# List of Figures

2.1	Angular momenta related to the spin-exchange optical pumping process	10
2.2	Formation and break-up of a van der Waals molecule . . . . .	12
2.3	A “tipped away” magnetization in an external magnetic field . . . . .	23
2.4	Time evolution of the effective magnetic field in the rotating reference frame . . . . .	26
2.5	Timing diagram of a 2DFT process . . . . .	31
3.1	Optical setup for spin-exchange rate constants measurements concerning alkalis K and Cs, using the Ti:Sapphire laser . . . . .	35
3.2	The coil system for performing adiabatic fast passage measurements . .	35
3.3	Schematic of the electronics setup for the measurements of the spin-exchange rate constants . . . . .	38
3.4	Time evolution of the $^{129}\text{Xe}$ nuclear polarization during the AFP process	40
3.5	A typical $^{129}\text{Xe}$ AFP signal . . . . .	42
3.6	The fit of a particular data set to determine the quantity $\gamma_{SE} + \Gamma_{\text{Xe}}$ . A histogram showing the scattering of the data points is plotted as an inset.	44
3.7	Fit of the measured relaxation rates versus Cs number density for a particular Cs-Xe cell . . . . .	47
3.8	A schematical diagram of the optical experimental setup for the Faraday rotation measurements . . . . .	51
3.9	Fitting of the difference in Faraday rotation angles versus the detuning of the incident light wavelength to determine Rb density . . . . .	54
3.10	Measured K densities, Killian’s empirical density formula for K, and our renormalized formula . . . . .	56

3.11	Measured Rb densities, Killian's empirical density formula for Rb, and our renormalized formula . . . . .	56
3.12	Measured Cs densities, Nesmeyanov's empirical density formula for Cs, and our renormalized formula . . . . .	57
3.13	Fit of spin-exchange rate per Cs atom versus effective number density in the cell to calculate the spin-exchange rate constants between $^{129}\text{Xe}$ and Cs . . . . .	59
4.1	Schematic of the design of our glass manifolds . . . . .	65
4.2	Schematic of the "bottom portion" of our vacuum system . . . . .	67
4.3	Schematic of the "top portion" of our vacuum system . . . . .	68
4.4	A typical readout from the RGA, after the pressure in the system had been brought down to a satisfactory level . . . . .	69
4.5	Schematic of the volumes involved in the determination of pressures in the filled cells . . . . .	71
4.6	A typical water(proton) AFP signal . . . . .	76
4.7	Schematic demonstrating the design of a prepolarized MRI system . . . . .	84
4.8	A PMRI image of a spherical water sample cell . . . . .	85
4.9	A sketch of the polarizing system for the hyperpolarized $^{129}\text{Xe}$ imaging study . . . . .	87
4.10	Time-decay of AFP signals produced by sample cell C5. The cell was removed from the polarizing system after the $^{129}\text{Xe}$ in the cell had been polarized to an equilibrium value. . . . .	88
4.11	An NMR signal produced by hyperpolarized $^{129}\text{Xe}$ . . . . .	90
4.12	A water NMR signal obtained using the prepolarizing technique . . . . .	91
4.13	A water NMR signal in low magnetic field, exploiting only the thermal proton polarization . . . . .	91
4.14	Hyperpolarized $^{129}\text{Xe}$ MR image obtained under a low magnetic field . . . . .	92

# List of Tables

1.1	Summary of published spin-exchange rate constants measurements and those presented in this thesis . . . . .	3
2.1	Nuclear spin $I$ and relative abundance $f$ of all major isotopes of K, Rb, and Cs. Values of $\zeta$ are calculated from these quantities. . . . .	19
3.1	Measured relaxation rates tabulated with respect to the cell temperature and calculated Cs number density for a particular Cs-Xe cell . . . . .	47
3.2	Spin-exchange rate per Cs atom measured for the 9 Cs-Xe cells, tabulated with the number densities of Xe and N <sub>2</sub> in the cells . . . . .	59
3.3	Experimental results of $\langle v\sigma \rangle$ , $\gamma_M$ , and $b$ for the three alkali metals . . .	60
3.4	Comparison of spin-exchange rates between <sup>129</sup> Xe and the three alkali metals K, Rb, and Cs, under a typical condition . . . . .	62
4.1	Error analysis for the water calibration of the <sup>129</sup> Xe nuclear polarization in sample cell C5 . . . . .	80
4.2	Water calibration for the <sup>129</sup> Xe nuclear polarization in a cylindrical sample cell used for the measurements of the spin-exchange rate constants	81